Forschungszentrum Karlsruhe
Technik und Umwelt
Wissenschaftliche Berichte
FZKA 5835

Features of Arrival Time and Angle-of-Incidence Distributions of EAS Muons

I. M. Brâncuş, B. Vulpescu, H. Rebel, G. Völker, M. Duma, A. A. Chilingarian
Institut für Kernphysik

Oktober 1996

Forschungszentrum Karlsruhe
Technik und Umwelt

Wissenschaftliche Berichte
FZKA 5835

Features of Arrival Time and Angle-of-Incidence Distributions of EAS Muons

I.M. Brâncuş*, B. Vulpescu*, H. Rebel, G. Völker, M. Duma*, and A.A. Chilingarian**

Institut für Kernphysik

* IPNE, P.O.B. MG 6, RO - 7690 Bucharest, Romania
** Yerevan Physics Institute, Cosmic Ray Dept., Alikhanyan Brothers Str. 2, Yerevan 36, Armenia

Forschungszentrum Karlsruhe GmbH, Karlsruhe
1996

Forschungszentrum Karlsruhe GmbH
Postfach 3640, 76021 Karlsruhe

ISSN 0947-8620

Abstract

Various features and correlations of the arrival time and angle-of-incidence distributions of muons of extensive air showers (EAS) are studied by analyses based on Monte-Carlo simulations of the EAS development by use the air shower simulation code CORSIKA. Trends and dependencies of the temporal dispersion of the EAS muon component on shower size and distance from the shower core are displayed by the distribution of the arrival time and angle of incidence of the first muon, of the mean and median of the single shower distribution. Special attention is called to multi-correlations in observations at different radial distances from the shower core, which are shown to provide additional information in view of a discrimination of different EAS primaries.

Charakteristika und Abhängigkeiten von Ankunftszeit- und Einfallswinkelverteilungen von Myonen ausgedehnter Luftschauer

Verschiedene charakteristische Eigenschaften und Korrelationen von Ankunftszeit- und Einfallswinkelverteilungen von Myonen ausgedehnter Luftschauer (EAS) werden untersucht auf der Grundlage von Monte-Carlo Simulationen der EAS Entwicklung mit Hilfe des Simulations-Codes CORSIKA. Die Ankunftszeitverteilungen und Winkelverteilungen werden charakterisiert durch die Ankunftszeit bzw. Einfallswinkel des ersten Myons, durch Mittelwerte und Median-Werte der Verteilungen in den einzelnen Schauern.

Spezielles Augenmerk wird gerichtet auf Vielfach-Korrelationen bei gleichzeitigen Beobachtungen in verschiedenen Abständen vom Schauer-Zentrum. Es wird gezeigt, daß ein solcher Beobachtungsmode zusätzliche Informationen zur Verbesserung der Unterscheidung der Art der Primärteilchen liefert.

1. Introduction

The current interest in a detailed understanding of the longitudinal development of extensive air showers (EAS), induced by high-energy primary cosmic rays, arises from the possibility to infer signatures of the mass of primary particle and of the nature of very high-energy particle interactions /1/. In this context already in early studies (see ref. /2/), observations of arrival time distributions of the shower particles at ground level have been considered as a source of information of the longitudinal structure of EAS. In particular, due to high penetrability of muons and Cerenkov photons, the temporal dispersion of the muon component /3/ and the shape of the Cerenkov pulse /4/ are considered to map rather directly the history and the geometrical structure of the shower development.

The case of the muons has been recently analysed in studies based on Monte Carlo - simulations of the muon production and propagation through the atmosphere:

a.) Danilova et al. /5/ analyzed the spatial angle-of-incidence and the arrival time distributions of EAS muons in order to relate them to the longitudinal profile of the muon cascade and to determine the muon production height. Their approach ("Time-Track-Complementarity" /6/) takes advantage from the correlation of the temporal and spatial characteristics of the muon component.

   The "Time-Track-Complimentary" principle has been recently experimentally approached by studies with the COVER-PLASTEX setup /7/ (Limited Streamer Tubes tracking hodoscopes, equipped with RPC-detectors for timing), inserted as subarray in the GREX array of the Haverah Park.

b.) Rebel et al /8/ focussed their interest to the shape and position of various kinds of muon arrival time distributions, their dependence from the shower size N_e, the radial distance R from the shower core and on the mass of the primaries, i.e. to discriminating features as signatures for the mass composition of cosmic rays. The studies are specifically related to the KASCADE experiment /9, 10, 11/ and include the detector performance of the experimental facilities.

The present work follows the investigations of Rebel et al /8/, completing some aspects of the studies of arrival time distributions as potentially observed with the the central detector facilities of the KASCADE experiment (see ref. /8/). The studies are extended to the analogous arrival angle-of-incidence distributions. As the actual KASCADE central detector is not dedicately designed for muon tracking measurements, the analyses are based on hypothetical muon detectors of 10 x 10 m^2 area and with ideal timing and tracking qualities. A set up of such detectors, located at several different distances from the shower center, is considered for exploring coherently the features of arrival time and angles-of-incidence distributions. Special attention is focused to multicorrelations of shower variables at different radial distances, thus establishing a "radial correlation" approach, especially for arrival time measurements.

The "observed" arrival time and angle-of-incidence distributions and their correlations are analysed by nonparametric multivariate analyses techniques /12/ with respect to signatures of the mass of the EAS primaries.

2. EAS simulation data

The set of data of simulated EAS, induced by p, O and Fe primaries, is the same as used in ref /8/, enlarged by oxygen initiated EAS and calculated for nine values of the primary energy E_0 in equidistant steps of the log E_0 scale between 10^{14} and 10^{16} eV and grouped in nine groups of the shower size, taking into account the realistic primary energy spectrum. All simulations have been performed with the air-shower Monte Carlo simulation program CORSIKA /13/, which has been specifically developed to perform simulations for the KASCADE experiment and is under continuous refinements of the hadronic interaction models used as Monte-Carlo generators. All secondary particles are tracked explicitly along their trajectories, and their parameters are stored on tape when reaching the observation level. This allows a detailed analysis of all features of the simulated data. For sake of simplicity these exploration studies consider showers of vertical incidence only.

Some characteristic features of various types muon distributions of typical proton and Fe induced showers at $E_0 = 10^{15}$ eV are illustrated by displays in ref /14/.

3. Arrival time distributions in the sight of the KASCADE central detector - a replique

The KASCADE central detector (described in detail elsewhere /9, 10, 11/) identifies muons of an energy threshold of 2 GeV by position-sensitive large-area multiwire proportional chambers (MWPC), installed in the basement under the iron-sampling calorimeter (thickness ca. 1000 g/cm^2) and distributed over an area of 20 x 16 m^2 /8, 15/. The MWPC setup works together with the trigger and timing facility, which is an active layer of the calorimeter and consists of 456 plastic scintillator detector elements (covering 64 % of the total area of the central detector area). Each single element consists of two quadratic scintillator sheets of 3 cm thickness (Fig. 1), with an readout by a wavelength shifter (WLS) and a photomultiplier. Two detectors are housed, optically isolated, in one single detector box. The time resolution of these trigger detectors is σ_t = 1.8 ns.

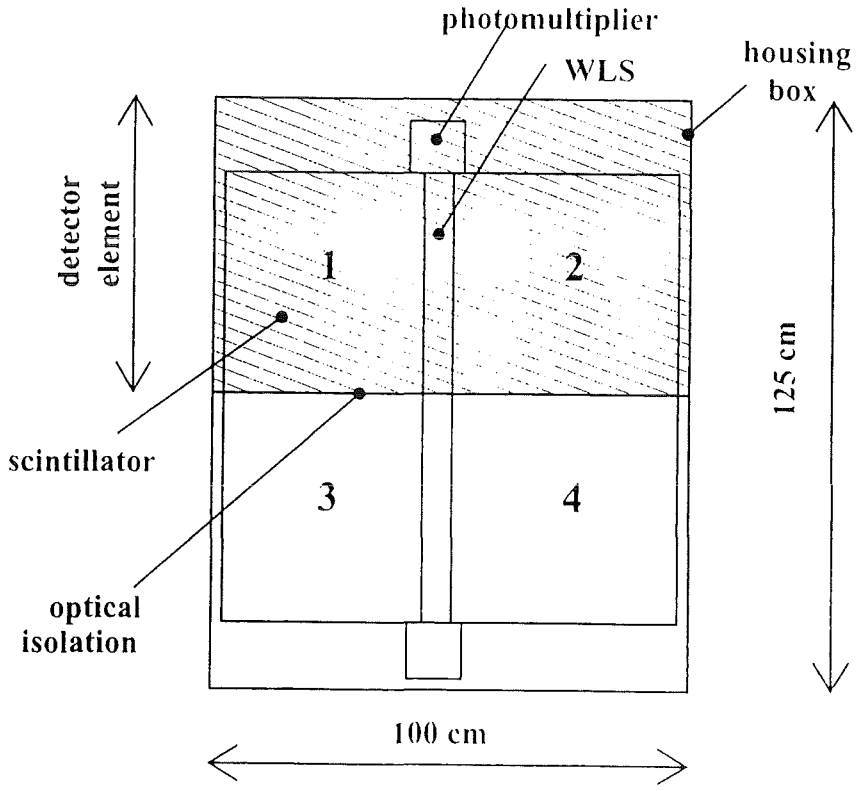

Fig. 1: Detector element of the trigger and timing facility of the KASCADE central detector (see ref. /8/)

Muon arrival time distributions, whose structures depend on the mass and the energy of the primary (on the shower size N_e, respectively), on the radial distance R_μ from the shower center, on the energy threshold and multiplicity of the muon observation, have been already extensively analysed for proton and Fe induced showers in view of the KASCADE facilities /8/. There, in addition to the distribution of the *mean* values of the muon arrival times

$$\Delta\tau_{mean} = \tau_\mu(R_\mu) - \tau_c \tag{3.1}$$

(τ_c = arrival time of the shower in the center),

the distributions of the arrival time

$$\Delta\tau_1 = \tau_\mu^1(R_\mu) - \tau_c \tag{3.2}$$

of the foremost muon (with large probability of originating from an early stage of the shower development), triggered by 4 subsequently registered muons, are studied.

The present paper follows these analyses, with completing the studies by including oxygen induced showers and taking into account the efficiency of the timing detectors. We consider also the question whether the *median* arrival times

$$\Delta\tau_{median} = \tau_\mu^{median} - \tau_c \tag{3.3}$$

may provide more pronounced signatures, especially, if combined with corresponding observations of the angle-of-incidence distributions (see chpt. 6).

3.1 Arrival time distributions of the foremost muon

Figs. 2a - 2b compile relative arrival time distributions of the foremost muons from proton induced showers of different shower sizes N_e and observed at different distances R_μ from the shower center. In Fig. 2b the influence of the time jitter in τ_c has been taken into account. It should be noted that in both figs. 2a and 2b the zero of the time scale is the same (fixed by τ_c without any fluctuation), so that in fig. 2b formally negative values for short $\Delta\tau_1^{det}$ occur. By the influence of the detectors the true first muon can be delayed so that the second, third ... muon have a chance to be counted as being the

foremost. In this way there appears a shift to 'negative' time values, especially in cases when the width of the arrival time distribution compares with the time resolution.

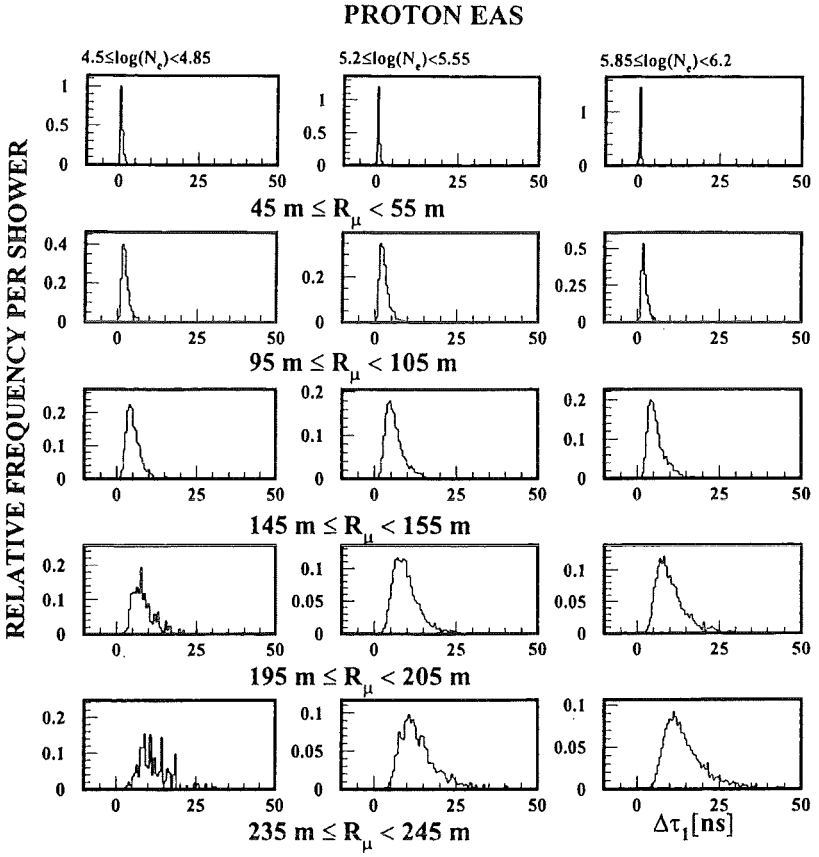

Fig. 2a: Relative arrival time distributions of the foremost muon, triggered by the muon multiplicity 5, of proton induced EAS (without detector resolution effects)

The influence of various contributions to the shape of the arrival time distributions ($\Delta\tau_1$ and $\Delta\tau_1^{det}$) is displayed in Fig. 3 and characterized by the mean values

$$\overline{\Delta\tau_1} = \sum_{i=1}^{N} \Delta\tau_1^i / N \qquad (3.4)$$

and the standard deviation

$$\sigma = \sqrt{\sum_{i=1}^{N} \left(\Delta\tau_1^i - \overline{\Delta\tau_1}\right)^2 / (N-1)} \qquad (3.5)$$

given in Tab. 1 for proton and oxygen induced EAS of two different ranges of the shower size N_e.

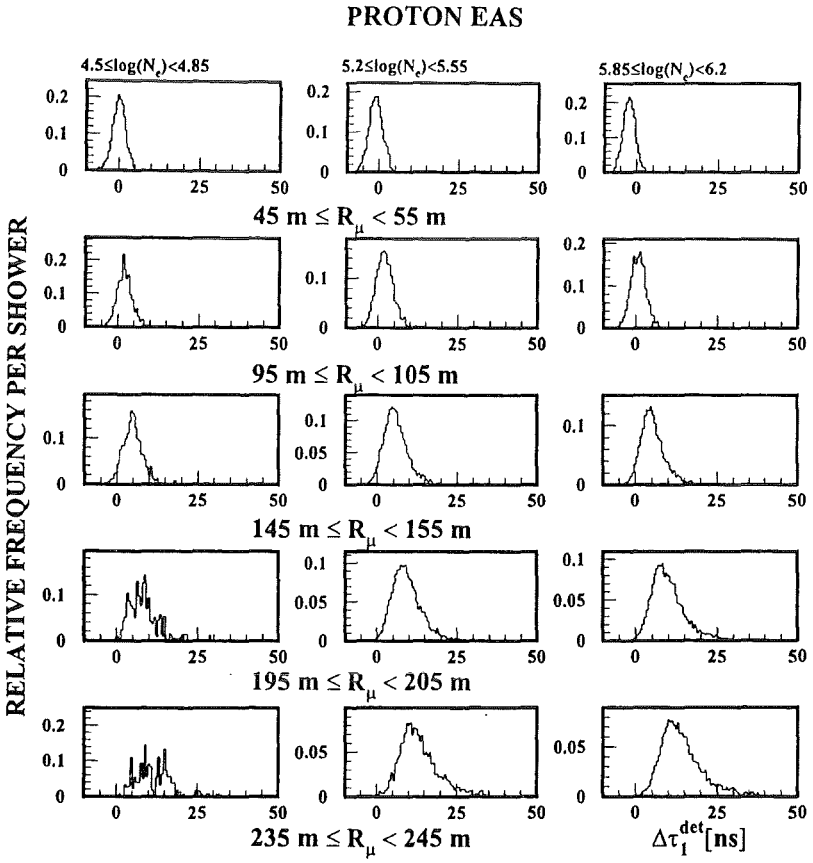

Fig. 2b: Relative arrival time distributions of the foremost muon, triggered by the muon multiplicity 5, of proton induced EAS (with detector resolution effects taken into account)

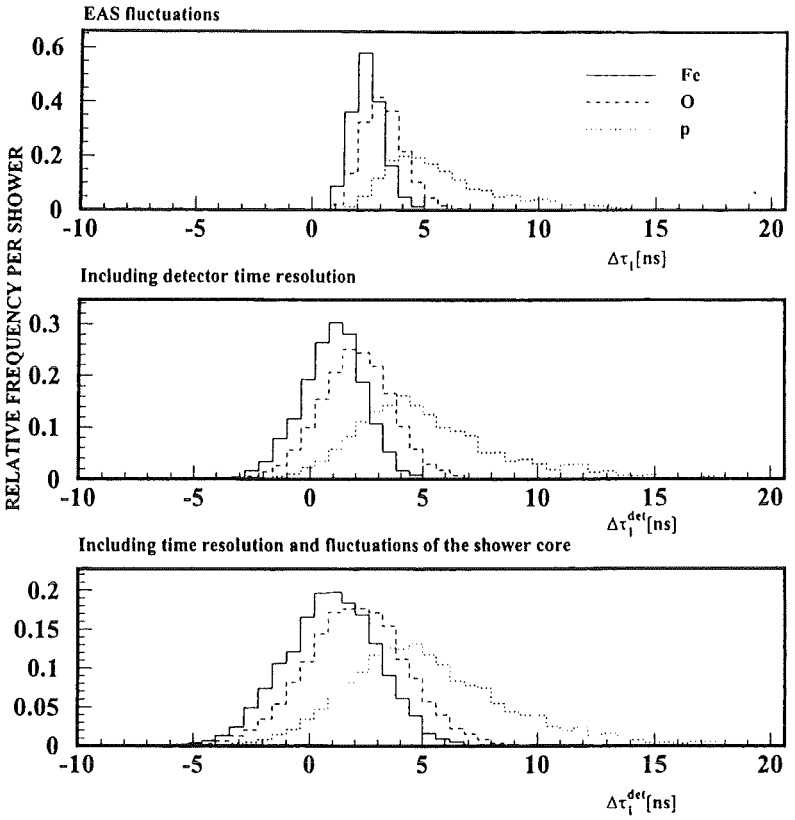

Fig. 3: Distributions of arrival times $\Delta\tau_1$ of the foremost muon of proton, oxygen and iron induced EAS of shower sizes of log N_e = 5.85 - 6.2 and observed at 150 m from the shower center (KASCADE observation level)

The variation with the radial distance from the shower center is shown in Fig. 4. Qualitatively the behaviour is in fair agreement with experimental observations of the arrival time distributions of EAS particles /7/.

Table 1: Mean value and standard deviation of the distribution of the muon arrival time $\Delta\tau_1$, observed at different distances R_μ from the shower center

log N_e = 3.8 - 4.2								
	PROTON				OXYGEN			
R_μ [m]	$\overline{\Delta\tau_1}$ [ns]	σ [ns]	$\overline{\Delta\tau_1^{det}}$ [ns]	σ [ns]	$\overline{\Delta\tau_1}$ [ns]	σ [ns]	$\overline{\Delta\tau_1^{det}}$ [ns]	σ [ns]
20	0.1	0.1	-1.9	1.3	0.1	0.1	-2.0	1.3
50	0.6	0.5	-0.7	1.5	0.4	0.3	-1.2	1.3
100	2.5	1.4	1.5	2.0	1.6	0.9	0.6	1.8
150	4.8	2.6	4.2	3.0	3.9	1.9	3.2	2.3
200	6.9	4.2	7.5	4.9	6.3	2.9	6.0	3.0

log N_e = 5.8 - 6.2								
	PROTON				OXYGEN			
R_μ [m]	$\overline{\Delta\tau_1}$ [ns]	σ [ns]	$\overline{\Delta\tau_1^{det}}$ [ns]	σ [ns]	$\overline{\Delta\tau_1}$ [ns]	σ [ns]	$\overline{\Delta\tau_1^{det}}$ [ns]	σ [ns]
20	0.1	0.1	-3.1	1.1	0.03	0.02	-3.9	0.9
50	0.7	0.5	-1.6	1.3	0.3	0.2	-2.6	1.1
100	2.8	1.7	1.7	2.3	1.6	0.7	-0.1	1.5
150	6.4	3.4	5.7	3.7	4.2	1.9	3.2	2.4
200	10.6	4.8	9.8	4.9	7.4	3.0	6.4	3.3

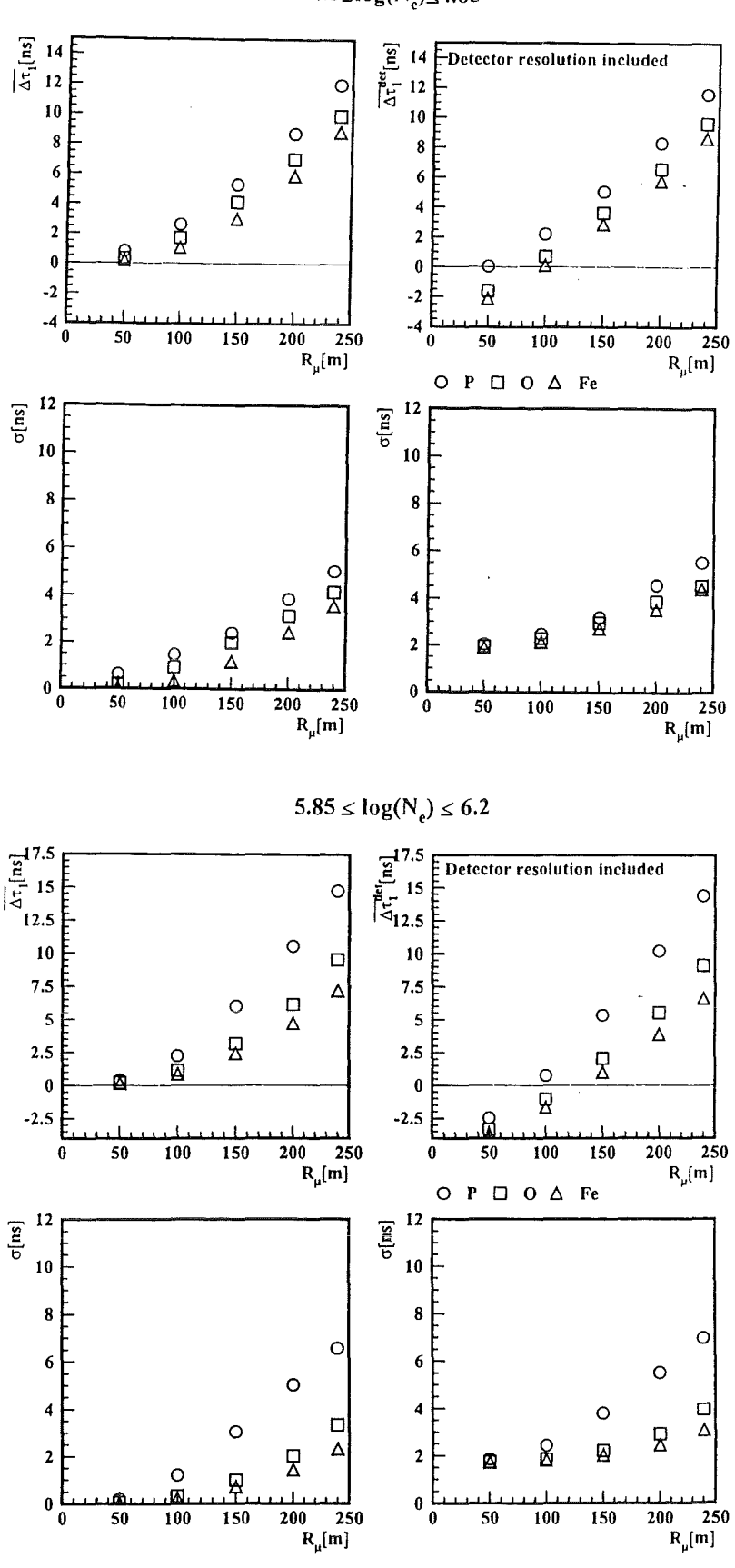

Fig. 4: *The dependence of the mean value $\overline{\Delta\tau_1}$ and of the standard deviation σ of the muon arrival time $\Delta\tau_1$ on the radial distance R_μ from the shower center*

3.2 Parametrization of the arrival time distributions

Following Woidneck and Böhm /16/ the arrival time distributions may be parametrized in terms of the Γ-probabilitiy density function

$$W_i(t - t_0,\ \bar{t},\ \sigma_\Gamma) = C_i(t - t_0)^b \exp(-\lambda(t - t_0)) \qquad (0 < t - t_0) \qquad (3.6)$$

whose parameters are related /17/ to the mean delay

$$\bar{t} = (1 + b) / \lambda \qquad (3.7)$$

and the standard deviation

$$\sigma_\Gamma = \sqrt{1 + b} / \lambda \qquad (3.8)$$

can be compared with the values extracted from the empirical distributions (like those shown in Fig. 4). In addition to the scale and shape parameters σ_Γ and λ, the position of the distribution is shifted by a third parameter t_0 while C_i contains the relative normalization in a superposition of different distributions W_i.

Fig. 5 displays the result of fitting the arrival time distributions ($\Delta\tau_1$)using this kind of parametrization and minimizing χ^2. Once the shape and position of the single distributions fixed, one may use this knowledge to analyse an unknown superposition and disentangle a mixed composition. The result of such an attempt is shown in Fig. 5d.
Table 2 compares the mean value and the variance, directly evaluated from the simulation data with those resulting from the fit.

Table 2: Comparison of the mean value and the variance of the arrival time distributions ($\Delta\tau_1$) extracted from the simulation data and the fits by the Γ-functions parametrization.

	R_μ = 100 m				R_μ = 150 m			
	Empirical		Γ-fit		Empirical		Γ-fit	
Primary	$\overline{\Delta\tau_1}$	σ	$\overline{\Delta\tau_1^\Gamma}$	σ_Γ	$\overline{\Delta\tau_1}$	σ	$\overline{\Delta\tau_1^\Gamma}$	σ_Γ
H	2.8	1.7	2.7	1.3	6.4	3.4	6.2	2.7
O	1.6	1.6	1.5	0.6	4.2	1.9	4.1	1.7
Fe	1.2	1.2	1.2	0.5	3.5	1.6	3.4	1.4

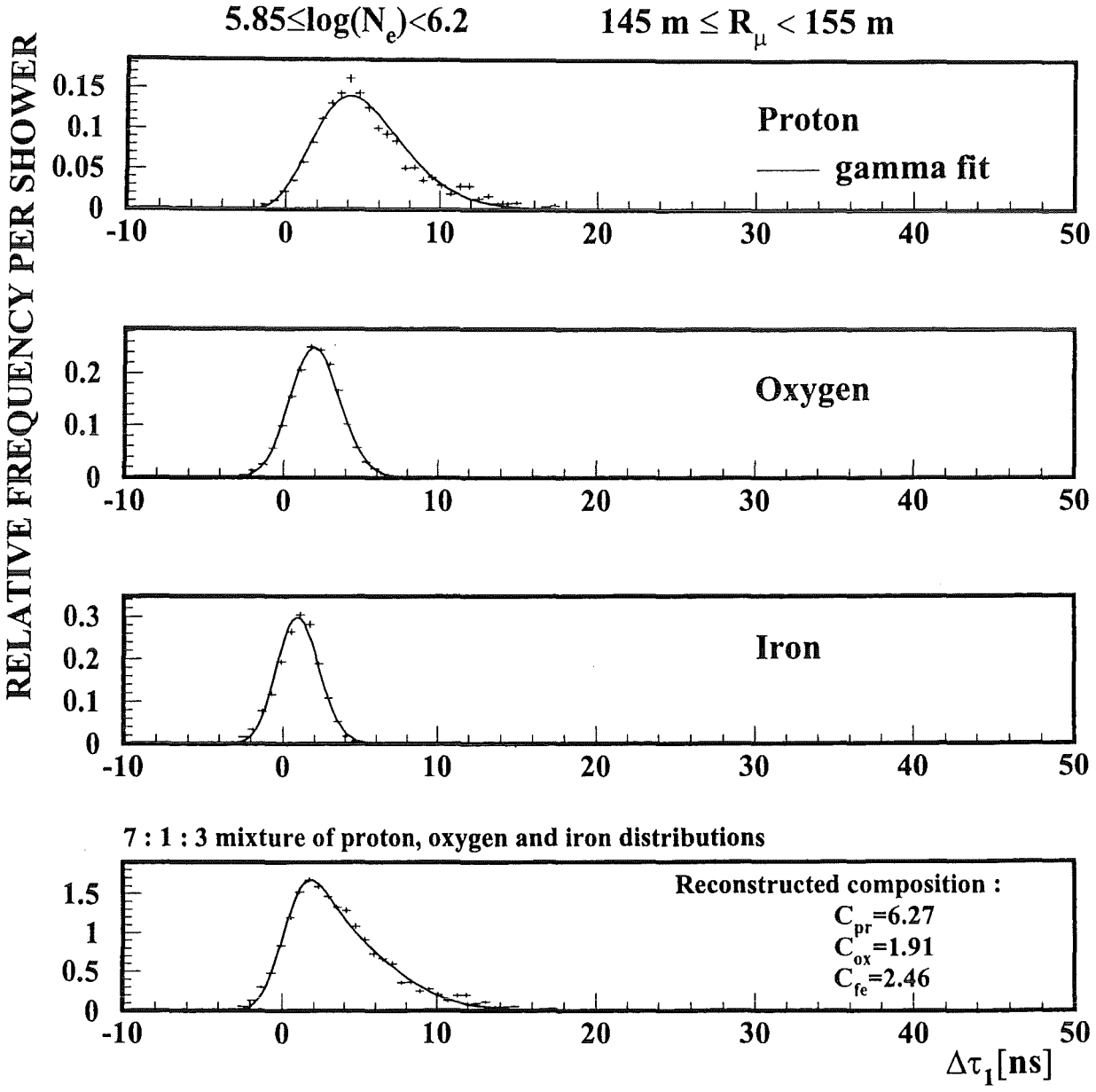

Fig. 5: *Representation of muon arrival time ($\Delta\tau_1$) distributions by a Γ-function parametrization fitted to the results of the EAS Monte-Carlo simulations. the result of a re-identification of a 7 : 1 : 3 - H : O : Fe mixed composition is shown.*

3.3 Is the median a better representative of the EAS muon arrival time distributions?

The statistical *median*, the median value in size in a group of observations, can distinctly differ from the *mean* value in cases, when few extreme values dominate the mean value. Therefore the distribution of the median values of the muon arrival time distributions may be less affected by extremely early or extremely late muons. However, the effect i.e. the difference from the distribution of the mean value of the arrival time or of $\Delta\tau_1$ is dependent from the a-priori unknown "true" muon arrival time distribution, we have to approach empirically. In order to get some quantitative insight, analogously to Fig. 3, the distributions of $\Delta\tau_1$, of $\Delta\tau_{mean}$ and $\Delta\tau_{median}$ are compared for proton, oxygen and iron induced EAS with different shower sizes and different distances (R_μ = 50 m and R_μ = 150 m) from the shower core (Fig. 6).

The relative time scale of these distributions reflects the time structure of the muon component, indicating that the first muons predominantly originate from the first generations (see ref. 8). The distribution of the median arrival times, narrowed in comparison to the mean arrival times indicates the larger abundance of 'early' muons and cuts obviously the influence of extremly delayed muons. On the other side, the influence of fluctuations of the arrival time of the first muon is also reduced.

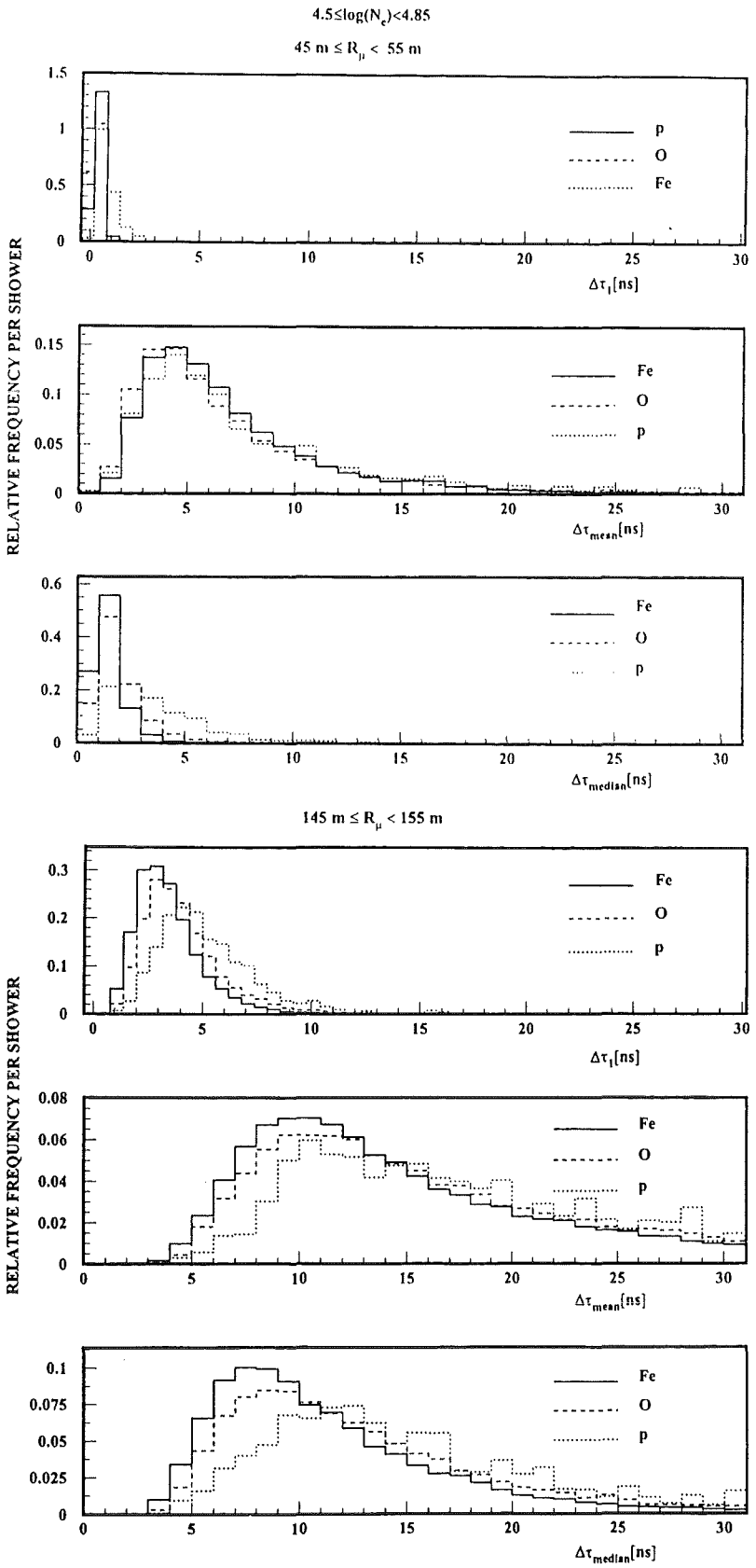

Fig. 6a-b: Distributions of $\Delta\tau_1$, of $\Delta\tau_{mean}$ and $\Delta\tau_{median}$ of muon arrival time distributions of proton, oxygen and iron induced showers at different distances from the shower core.

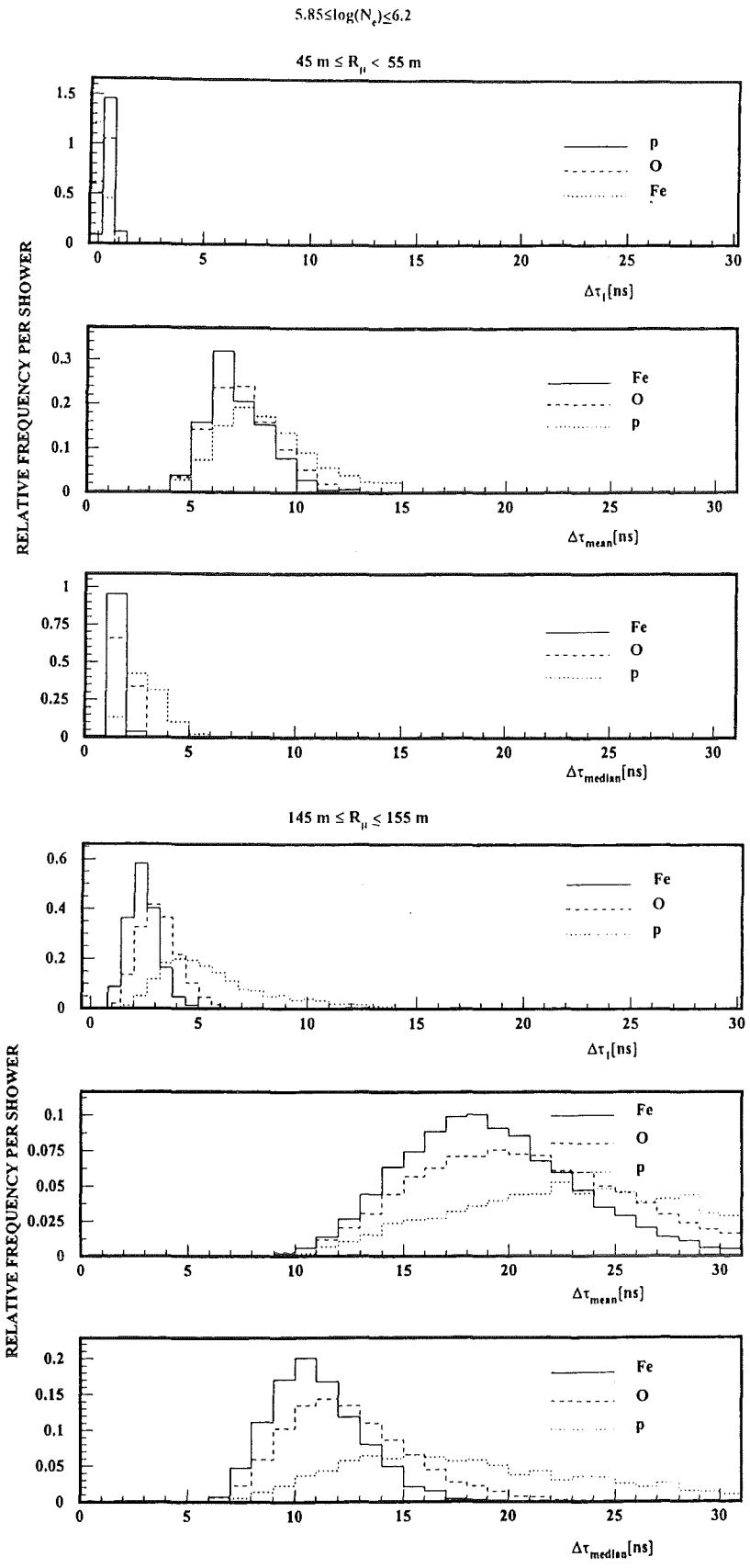

Fig. 6c-d: Distributions of $\Delta\tau_1$, of $\Delta\tau_{mean}$ and $\Delta\tau_{median}$ of muon arrival time distributions of proton, oxygen and iron induced showers at different distances from the shower core

4. Correlations of muon arrival time distributions observed at different radial distances

In previous studies of muon arrival time distributions /5, 8/ single distributions, observed at different radial distances from EAS center, have been analysed in view of signatures of the mass of the primary cosmic ray particles. In addition, correlations with various shower parameters, determined from the observations, like the N_μ / N_e ratio or the lateral shower age have been discussed /8/. In particular, the correlation with the distribution of the angle-of-incidence of the observed muons, which is considered to be complimentary to the time distribution, has been worked out in detail as source of information on the longitudinal shower development /5/.

In order to explore with a more general view the role of correlated muon arrival time distributions, observed at different distances from the shower center, we abandon the specific geometry of the KASCADE central detector and introduce a hypothetical array of several (ideal) timing detectors for muons of a collection area of 10 x 10 m^2 each and positioned within 10 m broad radial bins at different distances (50, 100, 150, 200 and 240 m) from the shower center.

Such an arrangement may weakly remind to a part of the KASCADE setup, observing extensive air showers with the core hitting the central detector (whose electron/photon detector array on the top provides the arrival time τ_c of the core) and measuring the muon arrival times with the muon tracking telescopes (as far as they are additionally equipped by timing devices) in the socalled "muon-tunnel" of the KASCADE array /18/.

For the following analyses we adopt the energy threshold $E_\mu \geq 1$ GeV of the muons detected in the KASCADE muon tunnel.

Ignoring the distortions by the limited detector qualities, Fig. 7 shows the correlations of the arrival times for muons observed at two different distances (R_μ^1 and R_μ^2) from the shower center. The graph emphasises the strong dependence of the correlation from the R_μ^1 - R_μ^2 - combination.

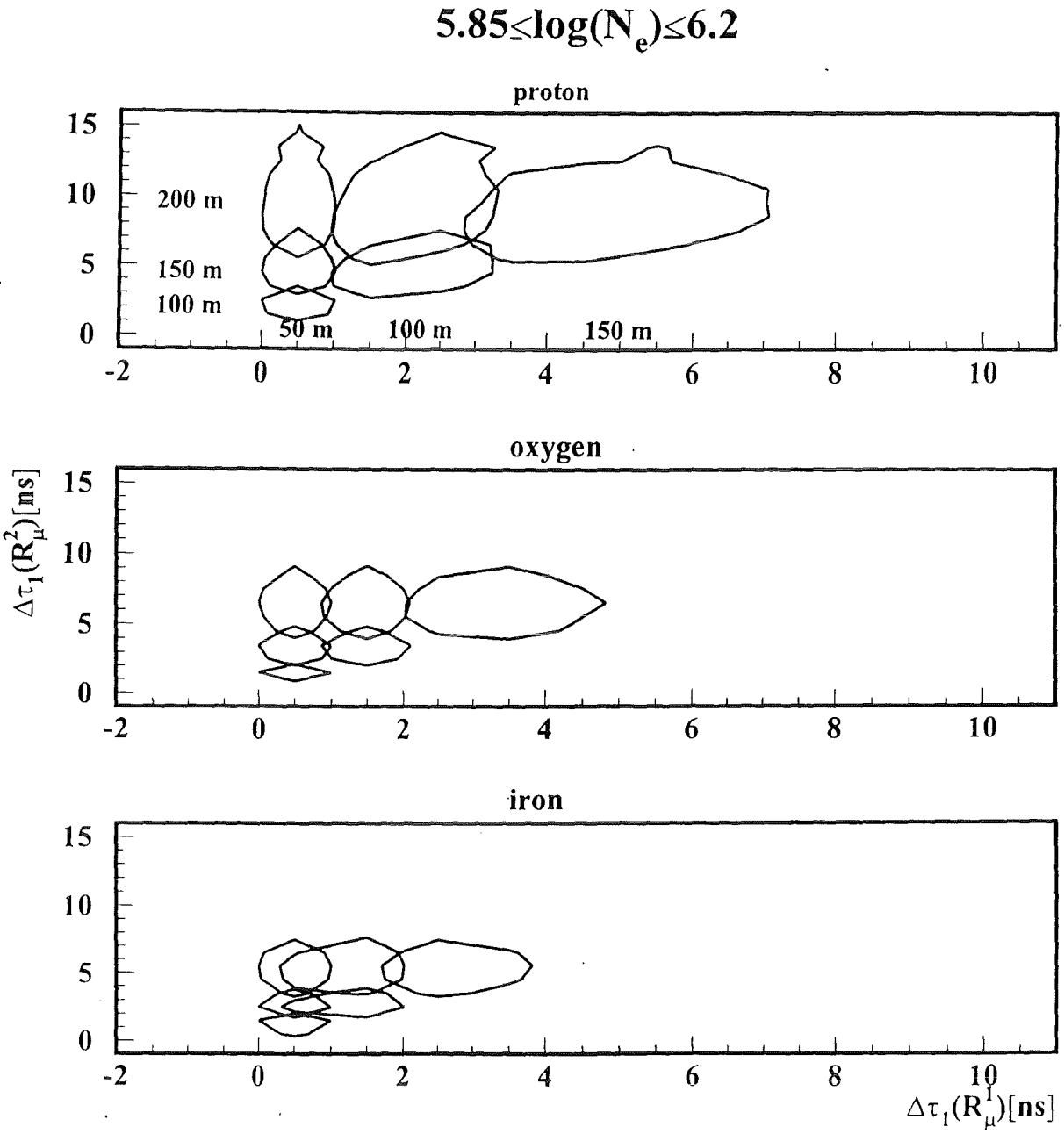

Fig. 7: Correlation of the arrival times of the first muons observed at different radial distances for proton, oxygen and iron induced EAS of $5.85 \leq \log N_e \leq 6.2$. The contour display the half-maximum of the distributions.

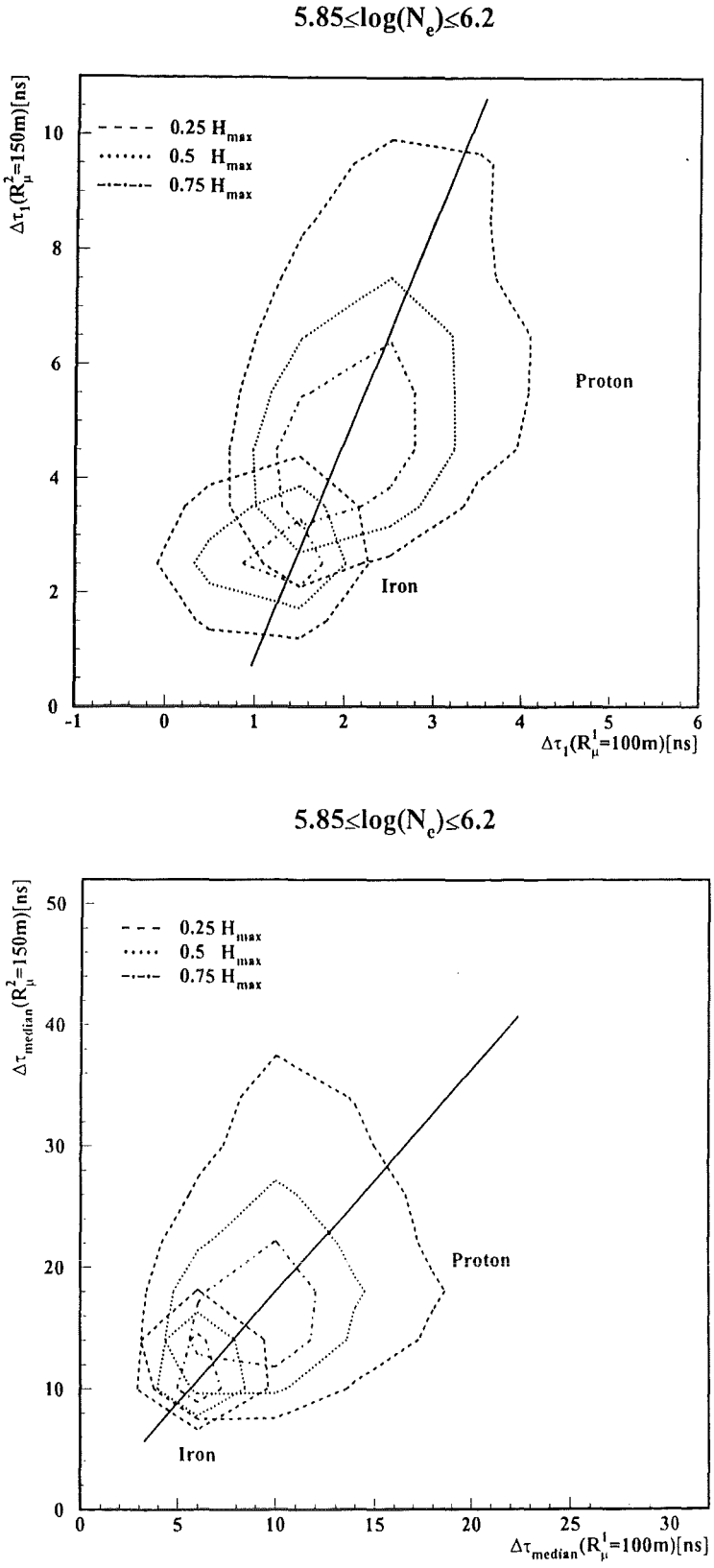

Fig. 8: Correlations of arrival time distributions represented by the foremost muons and the time median of proton and iron induced showers, observed with two detectors placed at $R_\mu^1 = 100$ m and $R_\mu^2 = 150$ m.

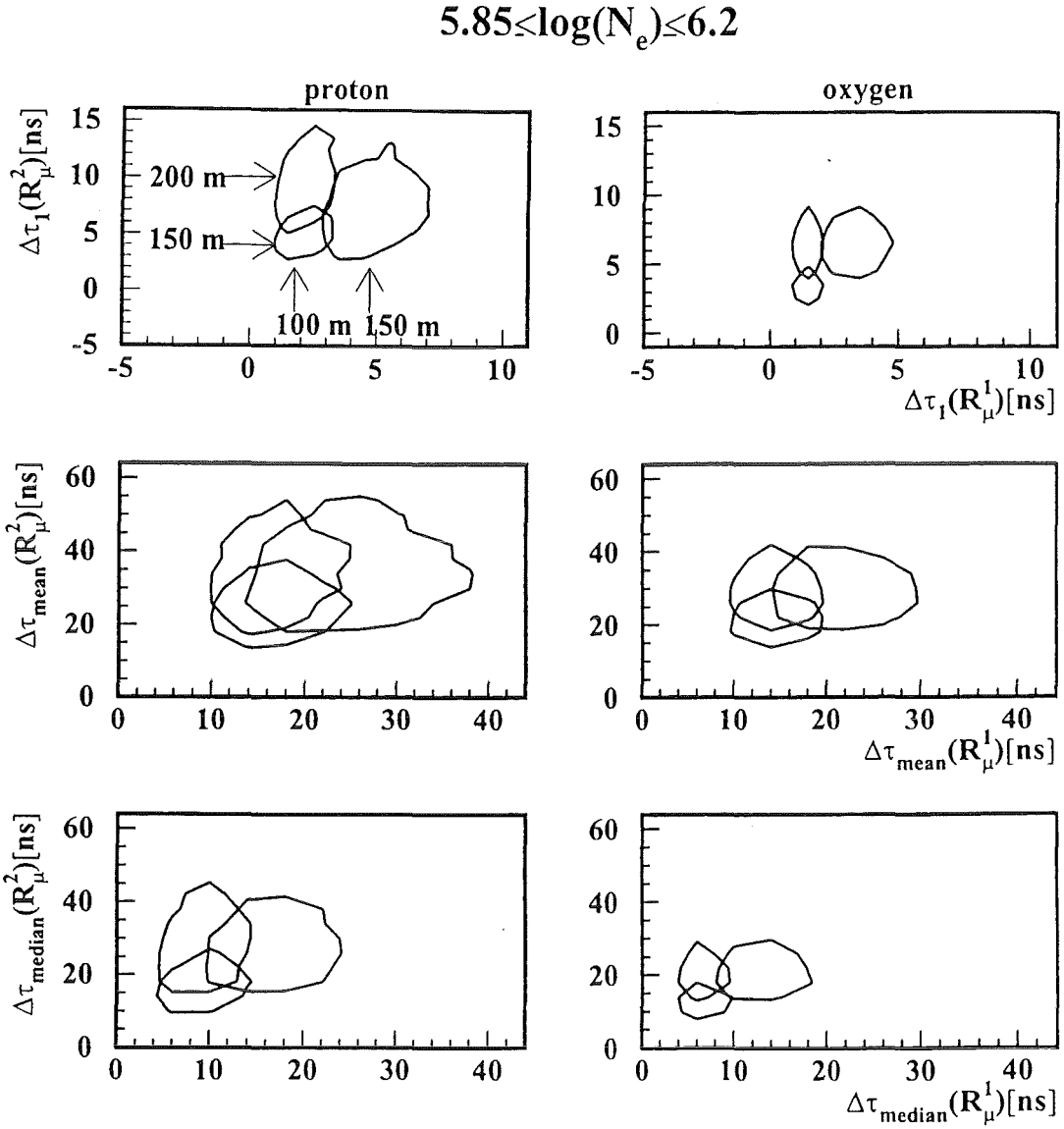

Fig. 9: Correlations of the muon arrival times for proton and oxygen induced showers observed at different distances from the shower center

The pronounced dependence on the mass of the primary cosmic particle, inducing the EAS is shown in Fig. 8, comparing the correlated distributions of the foremost muons at two different distances R_μ^1 = 100 m and R_μ^2 = 150 m for proton and iron initiated showers.

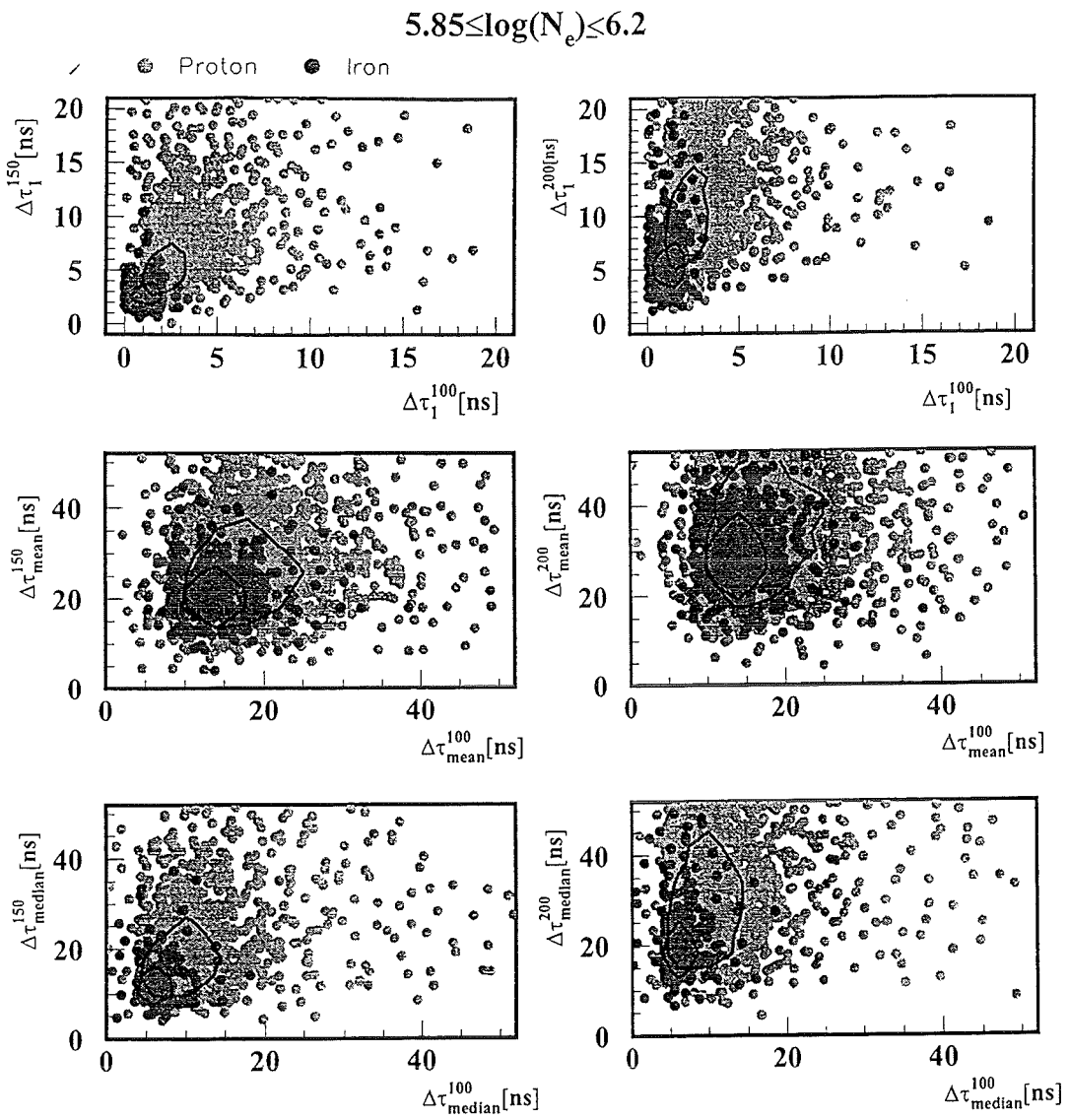

Fig. 10: Correlations of the muon arrival times for proton and iron induced showers observed at two different distances from the shower center

The above procedure (sect. 3.2) for the identification of the contributions of different masses to an a-priori unknown mixed composition can be modified by analysing the correlated time distribution, projected onto an adequately chosen axis (connecting the maxima) in the contour diagram (see Fig. 8). In fact, it turns out that the analysis of the correlated spectrum leads to an improved reconstruction of the original mass composition spectrum.

As further illustration Figs. 9 and 10 display the correlations of the arrival time distributions for $R_\mu^{1,2}$ = 100 and 150 m and of $R_\mu^{1,2}$ = 100 and 200 m represented by the arrival time of the first muon, of the mean and the median values of the distributions of EAS induced by different primaries.

5. Angle-of-incidence distributions of EAS muons

5.1 Uncorrelated distributions

While the arrival time distributions map the distribution of the production heights by the time of flight of the EAS muons, the angles-of-incidence reflect analogically the direction of travel, pointing to the production loci on (or near) the shower axis.

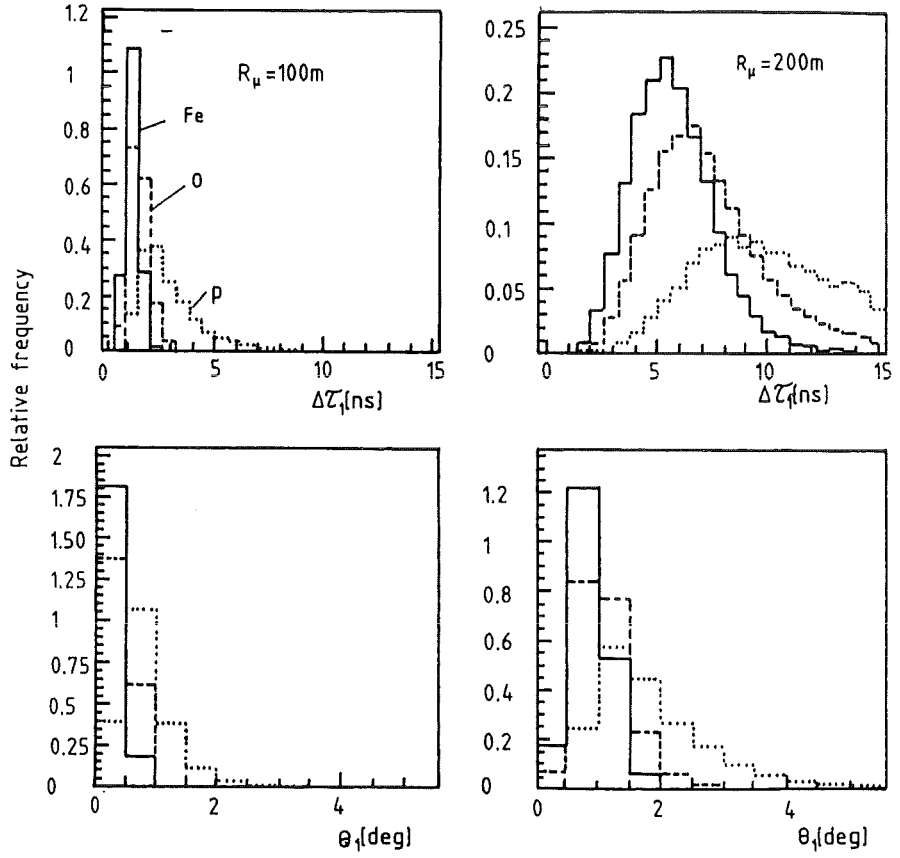

Fig. 11: Distribution of arrival times and angles-of-incidence of the foremost muons at two radial distances for shower sizes: log N_e = 5.85 - 6.2

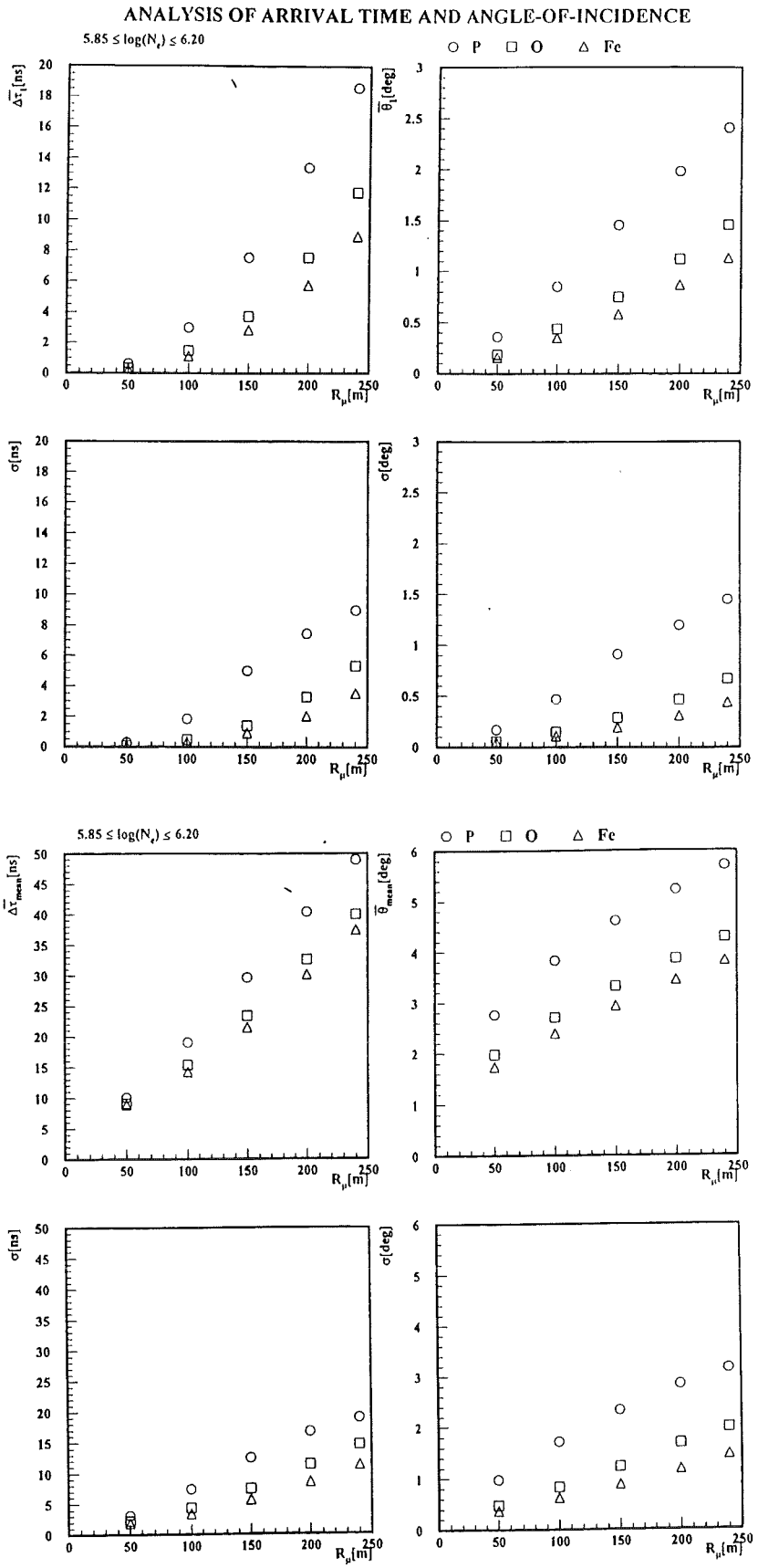

Fig. 12: Mean and standard deviation of the distributions of the foremost muons and of the mean of the single distributions: Dependence on the distance from the shower center ($5.85 \leq \log N_e \leq 6.20$)

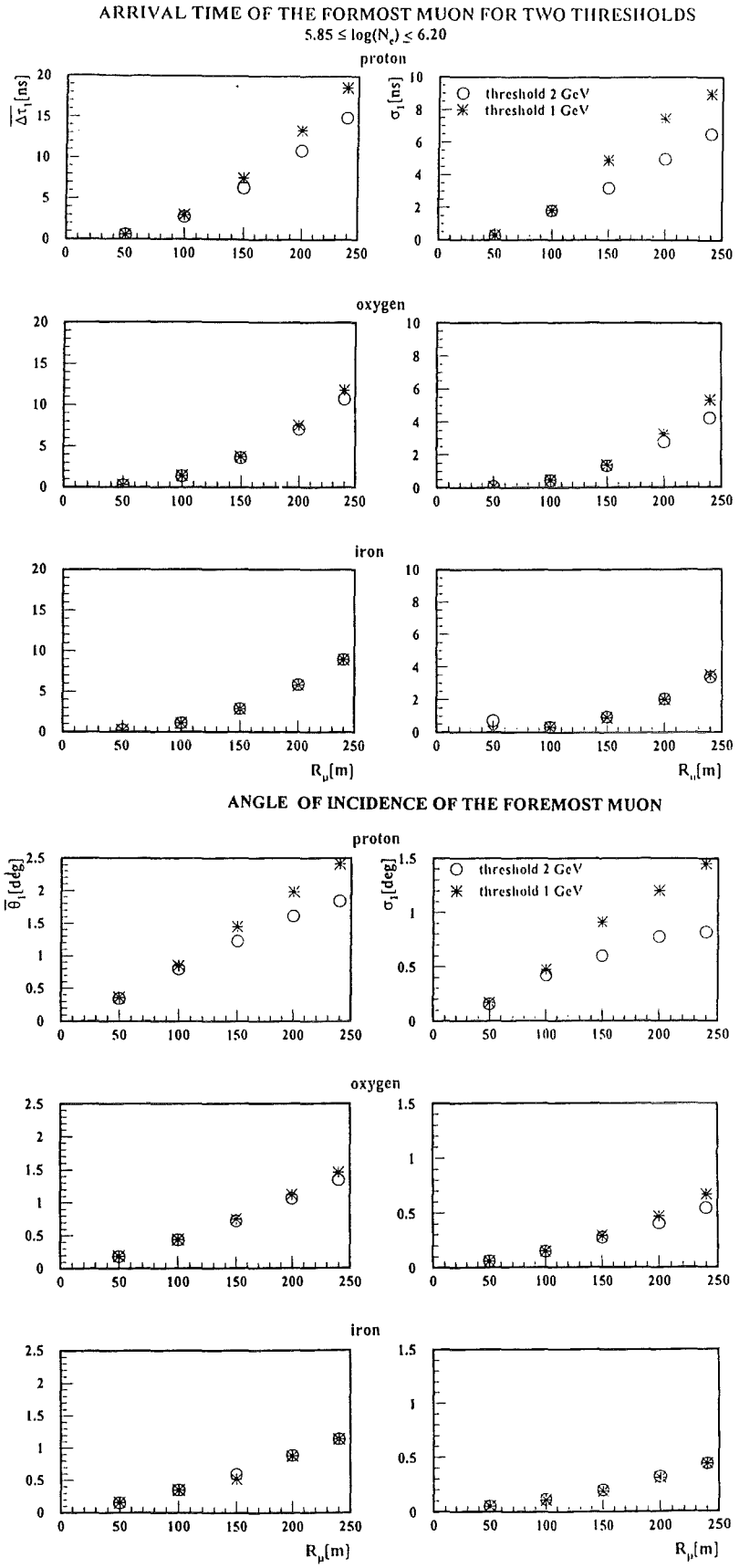

Fig. 13: Dependence of the distributions from the energy thresholds of the observed muons

Therefore the features of arrival time and angle-of-incidence distributions (see Fig. 11) exhibit similar trends, which are further illustrated by Fig. 12.

- With increasing distance from the shower center the distributions are shifted to larger average values and get broader.
- Comparing different type of primaries, the shifts and widths of the distributions appear to be smaller for the heavier primaries.

The displayed results correspond to an energy threshold of 1 GeV of the observed muons. In particular the widths of proton induced showers vary significantly with the energy threshold (Fig. 13). Below 1 GeV the distributions get rather shallow, obviously due to the increased influence of multiple scattering in the atmosphere.

5.2 Distributions of correlated observations

There are analogous correlations of the angle-of-incidence distributions observed a different radial distances from the shower center like they are noticed for the arrival time distribution (see sect. 4).

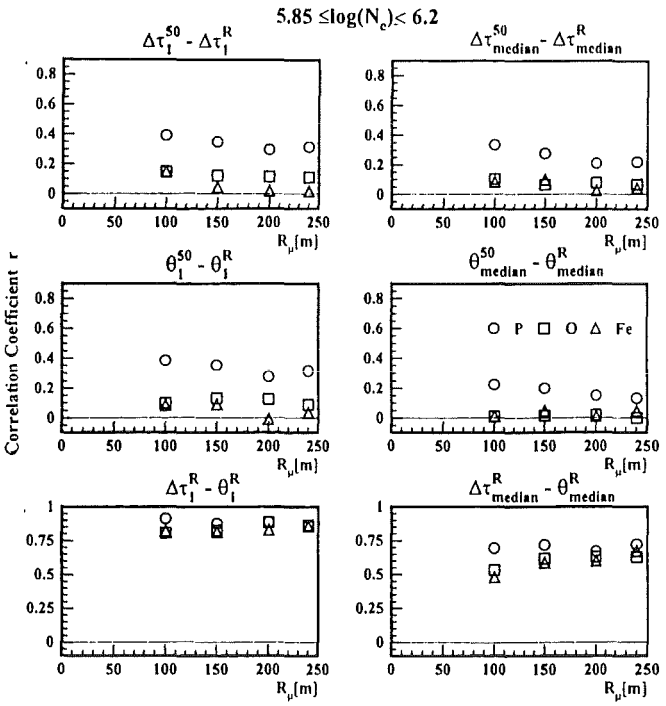

Fig. 14: Linear correlation coefficient for various correlated observation modes.

In order to quantify the degree of correlation Fig. 14 displays the values of the linear correlation coefficient /19/ for various combinations of the observation position R_μ. It indicates the significant correlation in the case of the observation of $\Delta\tau_1$, in particular for protons.

Most interesting is the significant correlation between arrival time and angle-of-incidence. This correlation appears with values of the correlation coefficient r = 0.8 - 0.9. It indicates a strong mutual dependence of both types of observables. That is basically understandable by their relation to the production heights of the EAS muons /2/. This correlation has been discussed in context of "Time-Tracking-Complementary Principle", used to improve the geometrical reconstuction of the production heights /6/ (though involving various approximations).

Figs. 15 - 16 illustrate the time-angle correlations dependent on different locations (R_μ) of the anticipated timing-tracking detector and on different primaries.

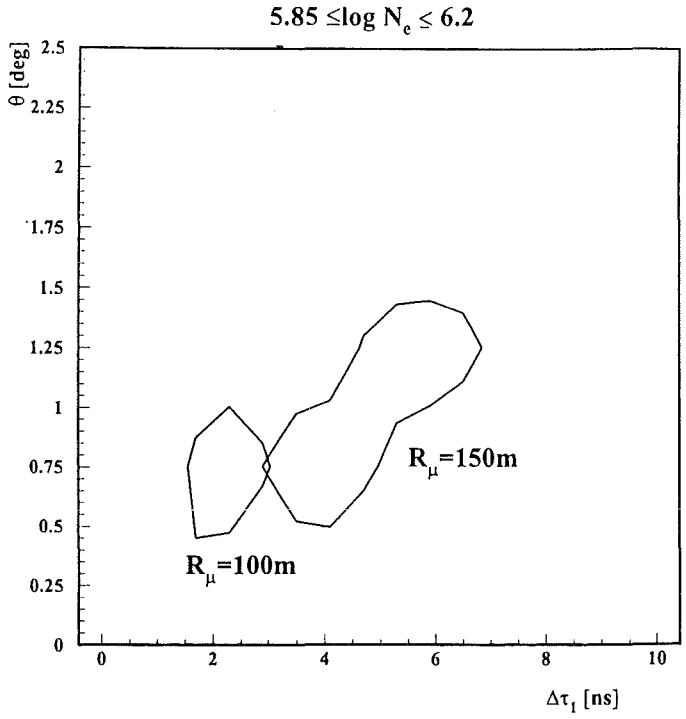

Fig. 15: Arrival time correlated with angle-of-incidence distributions of EAS-muons of proton induced showers

In order to study time-angle-correlations, simultaneously observed at two *different* distances R_μ from the shower core, we introduce a transformation of time and angle-like quantities.

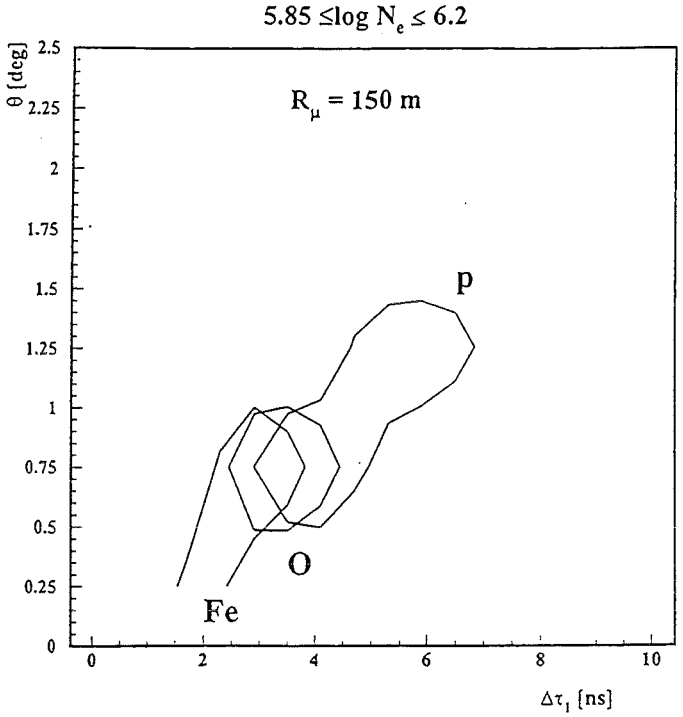

Fig. 16: Arrival time correlated with angle-of-incidence distributions of EAS-muons for different primaries

$$\Delta\tau \rightarrow h_1 = \left(R_\mu^2 - \left(c \cdot \Delta\tau\right)^2\right) / 2c\Delta\tau \tag{5.1}$$

$$\sigma_\tau \rightarrow \sigma_1$$

$$\Theta \rightarrow h_2 = R_\mu / \tan\Theta \tag{5.2}$$

$$\sigma_\Theta \rightarrow \sigma_2$$

and define a correlation quantity

$$h_{12}\left(R_\mu\right) = \frac{h_1\sigma_1^2 + h_2\sigma_2^2 + r_{12}\left(h_1 + h_2\right)\sigma_1\sigma_2}{\sigma_1^2 + \sigma_2^2 + 2r_{12}\sigma_1\sigma_2} \tag{5.3}$$

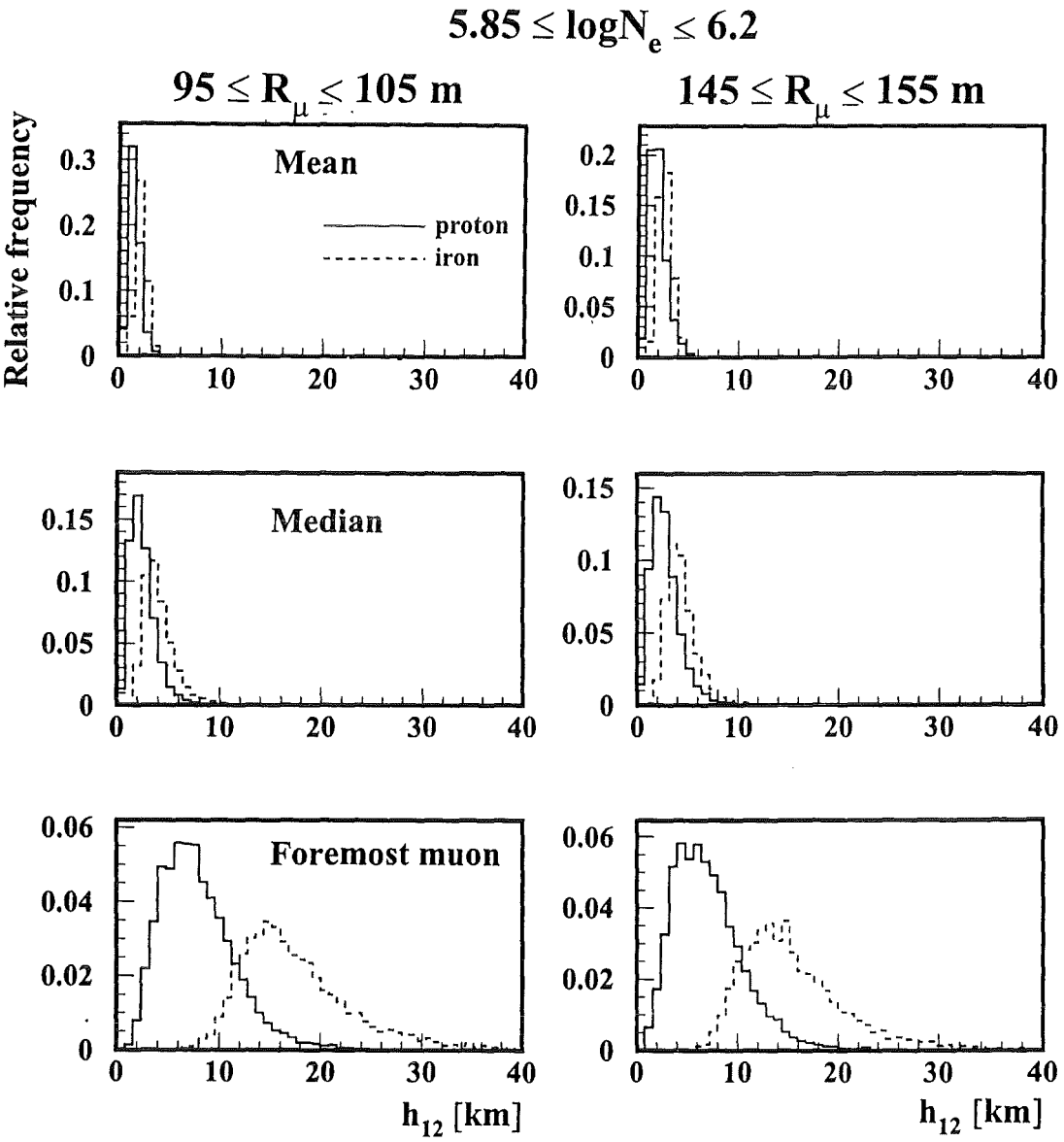

Fig. 17: Single distributions of the correlation quantity h_{12} (R_μ = 100 m) and h_{12} (R_μ = 150 m) for proton and iron induced showers

Actually this transformation relates $\Delta\tau_1$, or $\Delta\tau_{mean}$ and Θ_1, or Θ_{mean} to the geometrically reconstructed longitudinal development of the muon component, mapped by the $h_{1/2}$ distributions.

Due to the strong correlation between h_1 and h_2 indicated by the value of r_{12}, the information provided by h_{12} is practically the same as by h_1 or h_2 seperately.

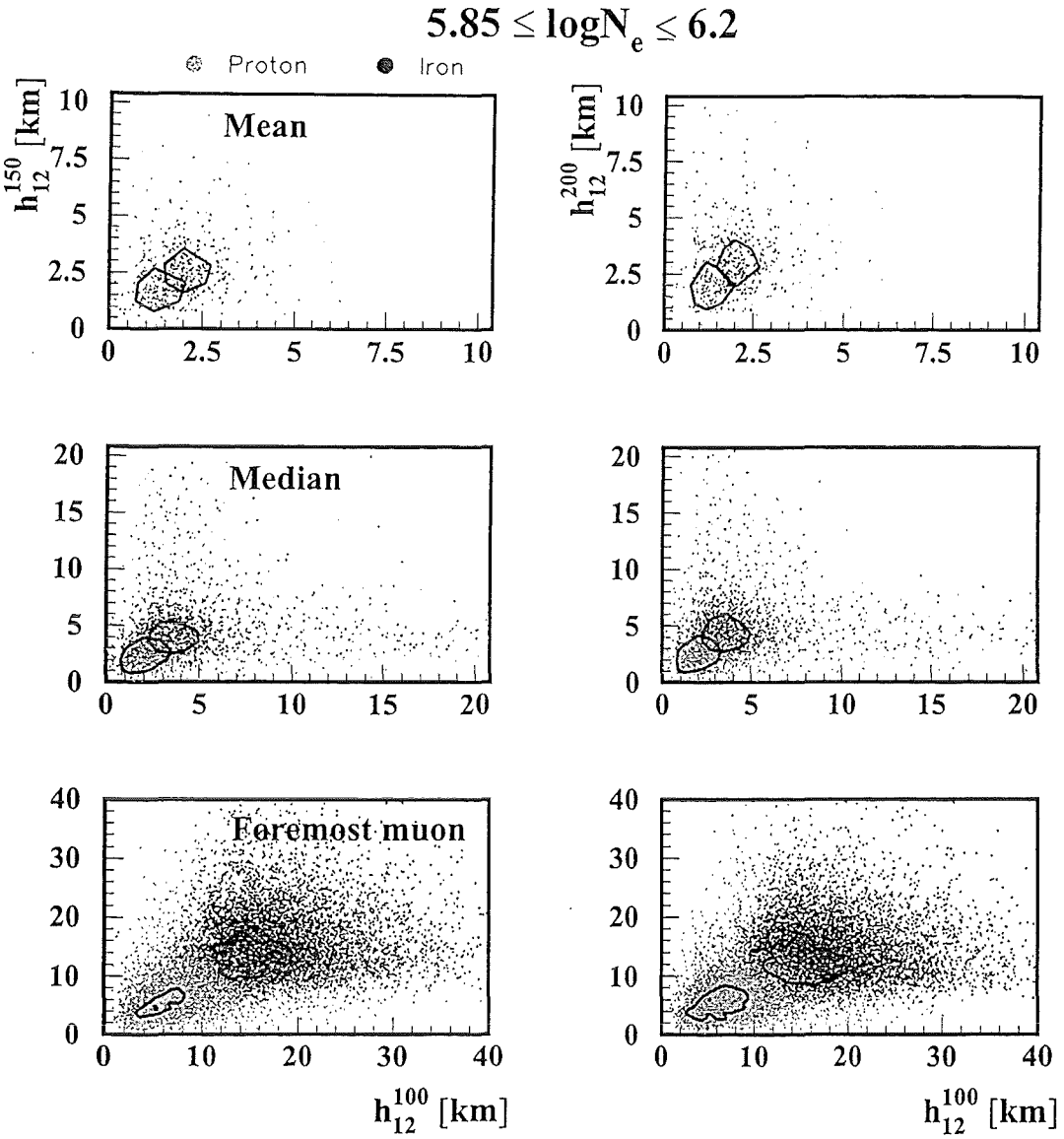

Fig. 18: Correlated distributions from two coincident timing-tracking observations at different values of R_μ

We use the correlation quantity for exploring the radial correlation of observations at *different* locations R_μ, Fig. 18 displays the distribution h_{12} (R_μ = 100 m) vs h_{12} (R_μ = 150 m) for two different primaries.

6. Application of nonparametric statistical analyses techniques

Multivariate analyses techniques facilitate the study of correlations between physical variables, the grouping of events by families and the comparison of experimental data with theoretical models. We use these techniques to explore the significance of the observed features for a discrimination of different EAS primaries, estimating the overlap of the multidimensional distributions and the misclassification by applying Bayesian decision rules /12, 20/. Extending previous applications to the analysis of muon arrival time distributions /8/ we scrutinize the above displayed features of arrival time and angle-of-incidence distributions, and in particular of their correlations, in view of a discrimination of the type of the EAS primaries.

6.1 The Bayesian approach

The analysis is focused to a statistical decision to associate a particular observed event v to a definite event class, say in our cases to proton or Fe-induced EAS. For that purpose we have to compare the a-posteriori probabilities

$$P\,(\text{proton}\,/\,v)\lessgtr P\,(\text{Fe}\,/\,v) \rightarrow \text{decision}\,\begin{cases}\text{Fe}\\ \text{proton}\end{cases} \tag{6.1}$$

with a quantification of the chance of a misclassification.

However, from the multivariate histograms (of the considered observables), resulting from the Monte-Carlo simulations, we do infer conditional probability density distributions *(likelihood functions)*

$$P\,(v\,/\,p) \text{ and } P\,(v\,/\,Fe)$$

of the observed events of a specified class. For an estimate of the *a-posteriori* probability the Bayes theorem is invoked, formulated with the notation of our example of discrimination Fe and proton primaries by

$$P(Fe\,/\,v) = \frac{p_{Fe}}{p_v} P(v\,/\,Fe) \tag{6.2}$$

$$P(prot\,/\,v) = \frac{p_{prot}}{p_v} P(v\,/\,prot) \tag{6.3}$$

Here p_{Fe} / p_v and p_{prot} / p_v are the initial assumptions about the probabilities (normalization: p_v) to observe an event of a specific class (*a-priori probabilities* by guesses which may be iterated in processing the analysis).

There are several procedures to prepare the likelihood functions from Monte-Carlo simulations (including neural network techniques). We use the most popular Parzen window technique /22/ which substitutes each element of the training sample by bell-shaped functions and constructs the probability density by a superposition of many „kernels".

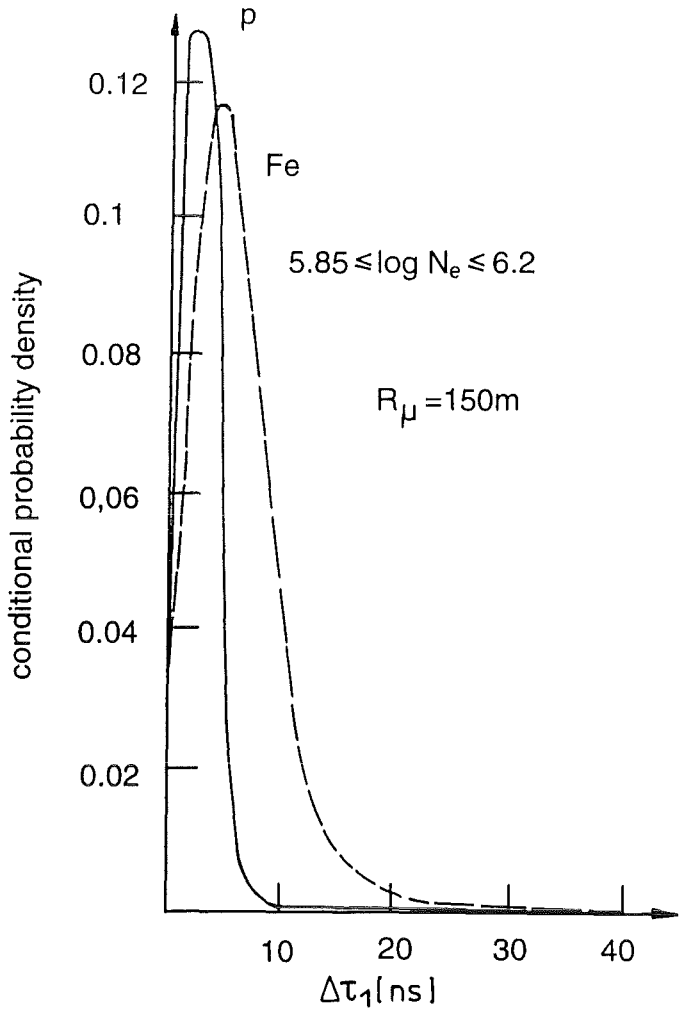

Fig. 19: Probabilitiy density distributions for the arrival time of the first muon for proton and Fe EAS primaries, shown for the case of R_μ = 150 m and log N_e = 5.85 - 6.2.

Fig. 19 displays examples of probabilities density distributions for the arrival time of the first EAS muon ($\Delta\tau_1$) derived from the training samples.

The chance to misclassify a particular observed event v_α due to the overlap of the likelihood functions is given by

$$r\,(v_\alpha) = \text{Min}\,\{\,P\,(\text{proton} / v_\alpha),\, P\,(\text{Fe} / v_\alpha) \tag{6.4}$$

and the Bayes error, indicating the chance to nisclassify the events of the observation space

$$R = \int_v r(v)P(v)dv \tag{6.5}$$

For an estimate of the Bayes error we use the method of the „one-leave-out-for-a-time" test /23/ which removes one element of the sample and trains the sample without it. The element is subsequently classified and returned into the sample. Thus, using the definition

$$\varepsilon(v) = \begin{cases} 0 & \text{if classified correctly} \\ 1 & \text{otherwise} \end{cases} \tag{6.6}$$

the estimate is

$$R^e = \frac{1}{M}\sum_e^M \varepsilon(v_e) \tag{6.7}$$

This estimate could be done each class: M = proton, Fe, ... seperately

$$R_m^e = \frac{1}{M_m}\sum_e^{M_m} \varepsilon\left(v_e^m\right) \tag{6.8}$$

6.2 Classification results

The following graph (Fig. 20) displays results of the analysis of the arrival time $\Delta\tau_1$ of the foremost muon, for two primaries (p, Fe) in two N_e-ranges. The classification and misclassification of a particular event depends on the extent to which the probability density distribution overlaps with the distributions of the other classes. Therefore, in principle, needle-like distributions, even closely positioned would lead to better

classification rates than broad distributions, through visibly clearly separated in the maxima, but considerably overlapping in the tails. In fact, due to this effects, the theoretical distributions, ignoring any influence of the finite time - and angular resolution, favour small R_μ for a better classification. In order to account for the more realistic situation, the dependence of the classification - and misclassification rates on the observation distance R_μ, shown in Fig. 20 is based on the case of the KASCADE detector taking into account the detector qualities (sect. 3), indicating distances of $R_\mu \geq$ 100 m as experimentally favoured detector locations. Of course, the optimal location is a matter of the specific detector qualities and of the density distribution of the muon component.

Since for broader distributions the detector resolution seems to be of minor influence, the further extension of the analysis to angle-of-incidence distributions, time-angle-correlations and to three different primaries (Fig. 21 a-c) returns to the distributions "seen " with the hypothetical timing-tracking setup (with infinite resolution), but restricted with $R_\mu \geq 100$ m. The results illustrate the main tendencies:

- the observation of the time-angle correlation does not improve the result derived for the arrival time and angle-of-incidence distribution separately
- the chance of misclassification and Bayes error decrease with the shower size and the distance R_μ, but they increase with the complexity of the mass composition.

Looking for various promising correlations (Fig. 22 - 24), we consider the correlation with the shower age and 'radial' correlations, i.e. observations correlating the distributions of different radial distances R_μ from the shower center.

Fig. 25 compares for a typical case the classification and misclassification probabilities in various observation modes and emphasizes the importance of observations correlating arrival time (and analogously angle-of-incidence) distributions of different radial distances, additionally classified by the shower age.

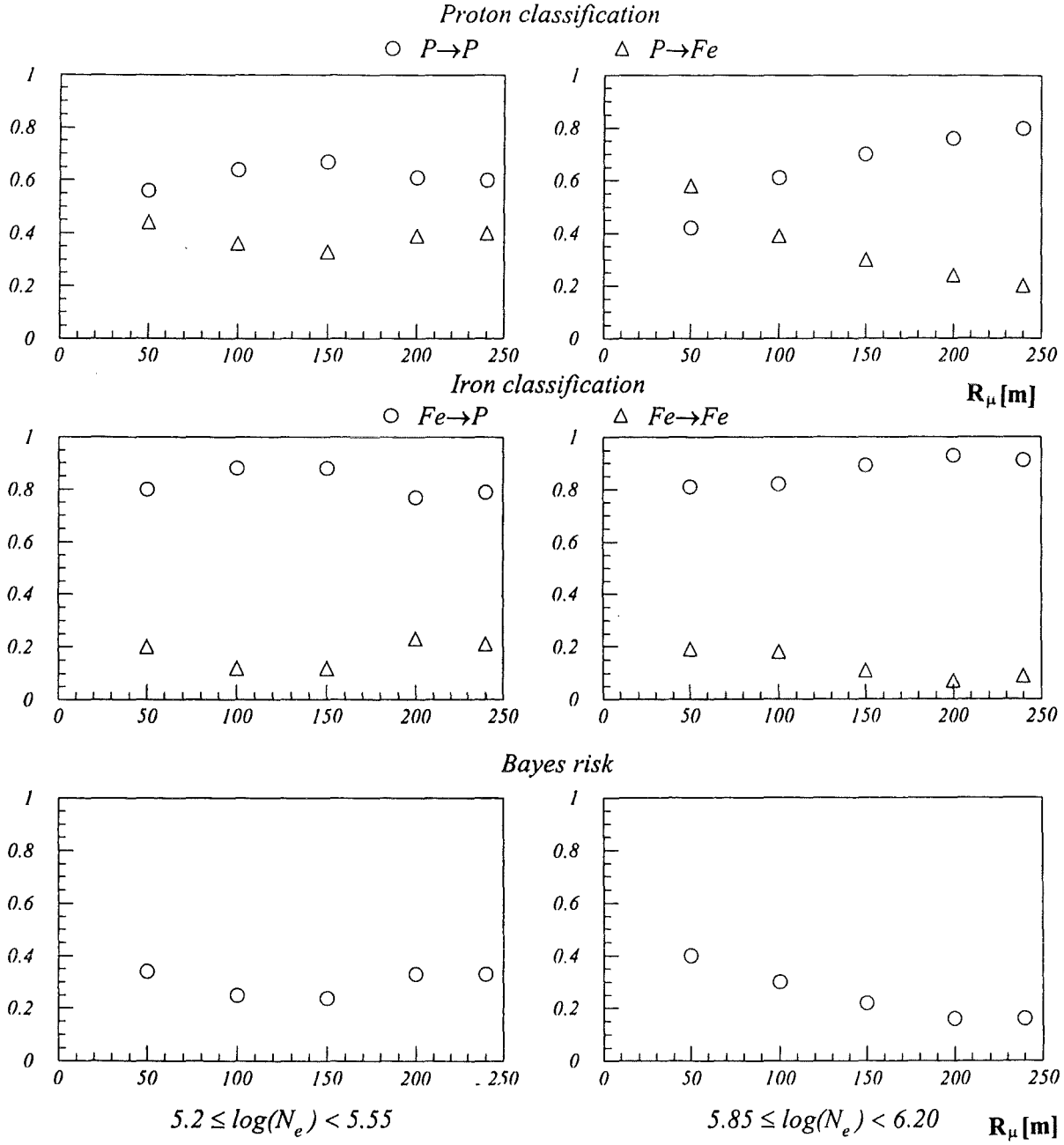

Fig. 20: The dependence of the classification probabilities on the observation distance R_μ, deduced from the arrival time distributions of the foremost muon, for two different primaries and N_e ranges.

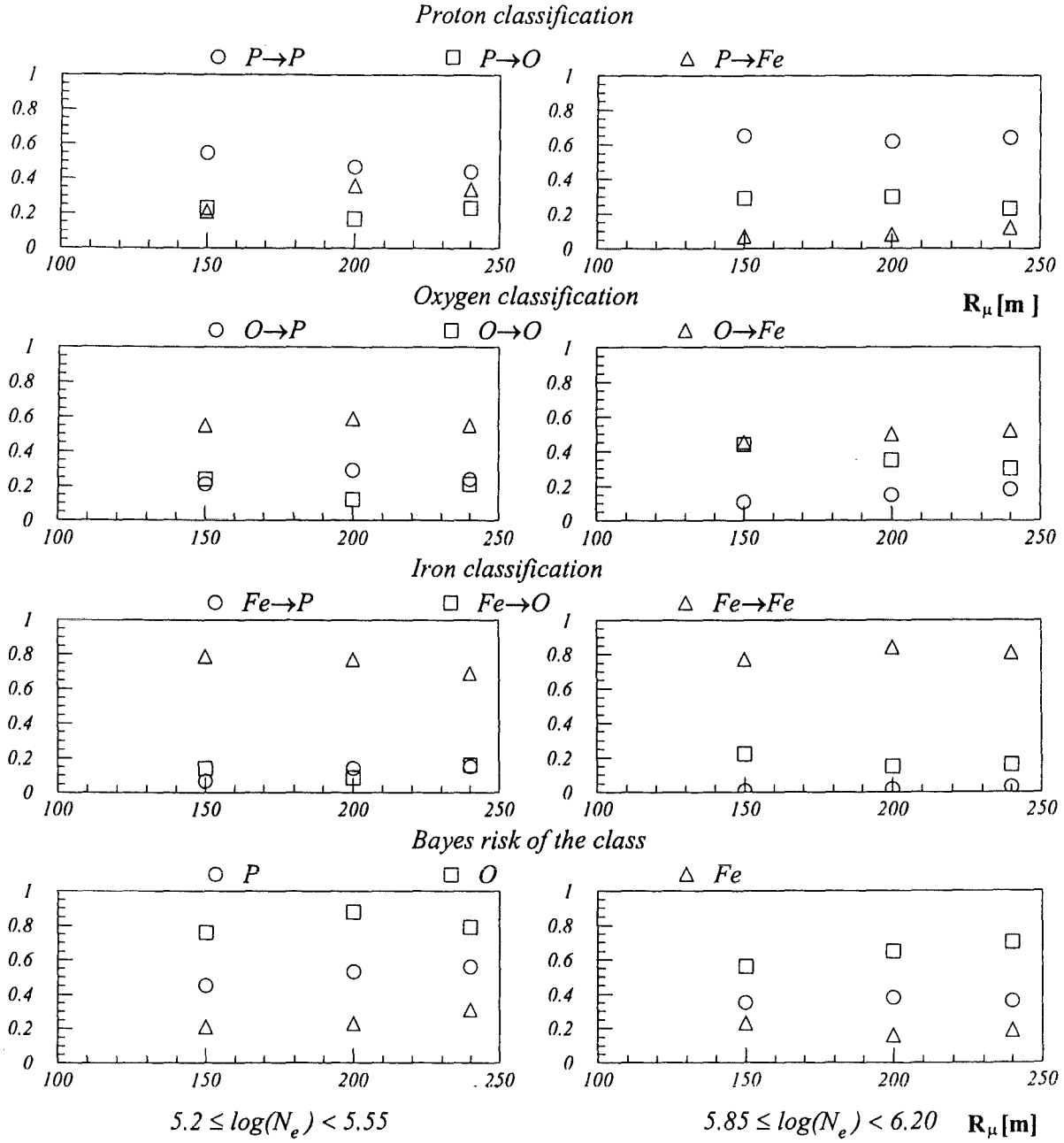

Fig. 21a: The true classification probabilities for proton, O and Fe primaries derived from the arrival time distributions of the foremost muon (observed at distancies $R_\mu \geq 100$ m) for two different N_e ranges.

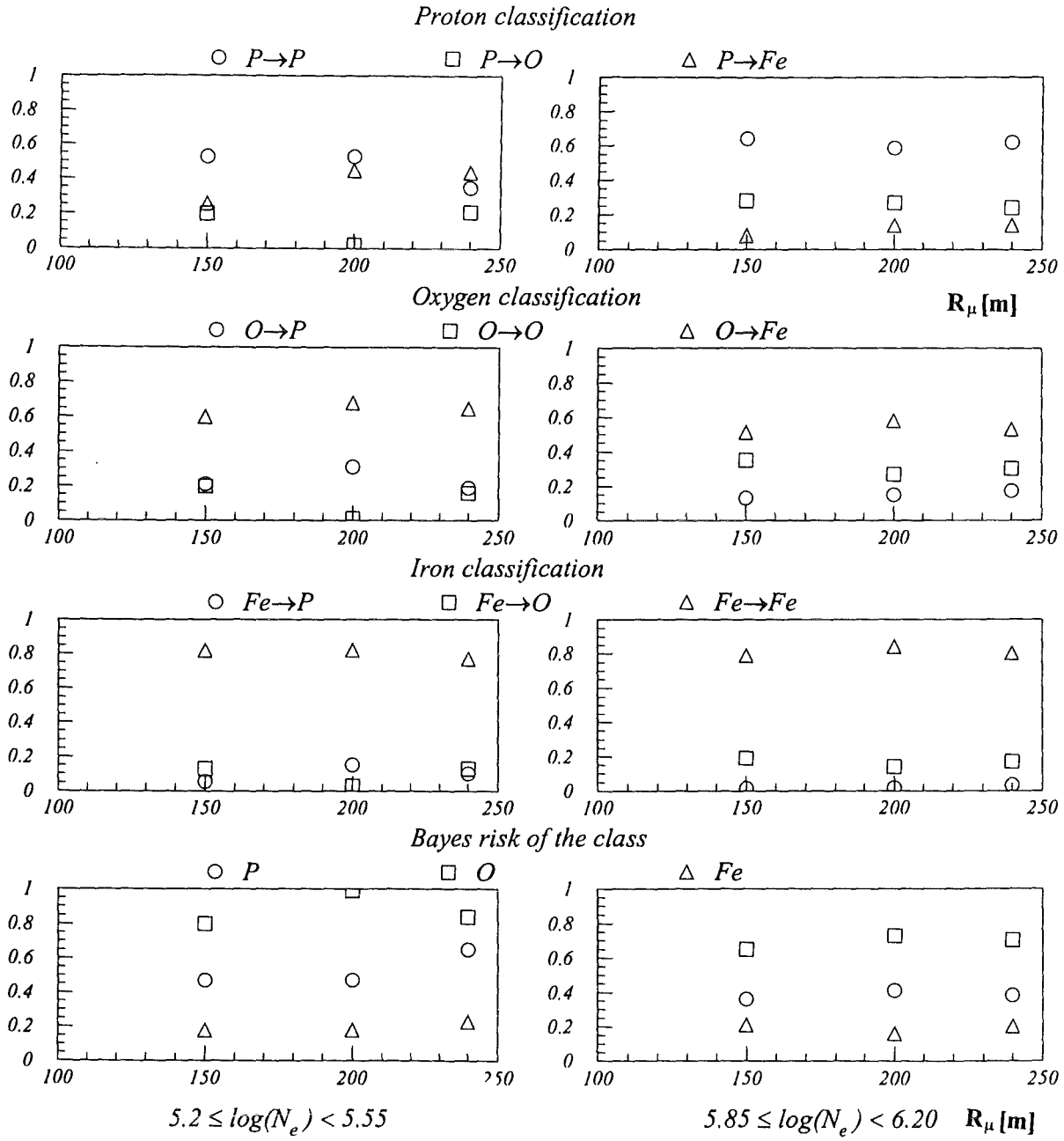

Fig. 21b: The true classification probabilities for proton, O and Fe primaries derived from the angle-of-incidence correlation of the foremost muon (observed at larger distancies R_μ) for two different N_e ranges.

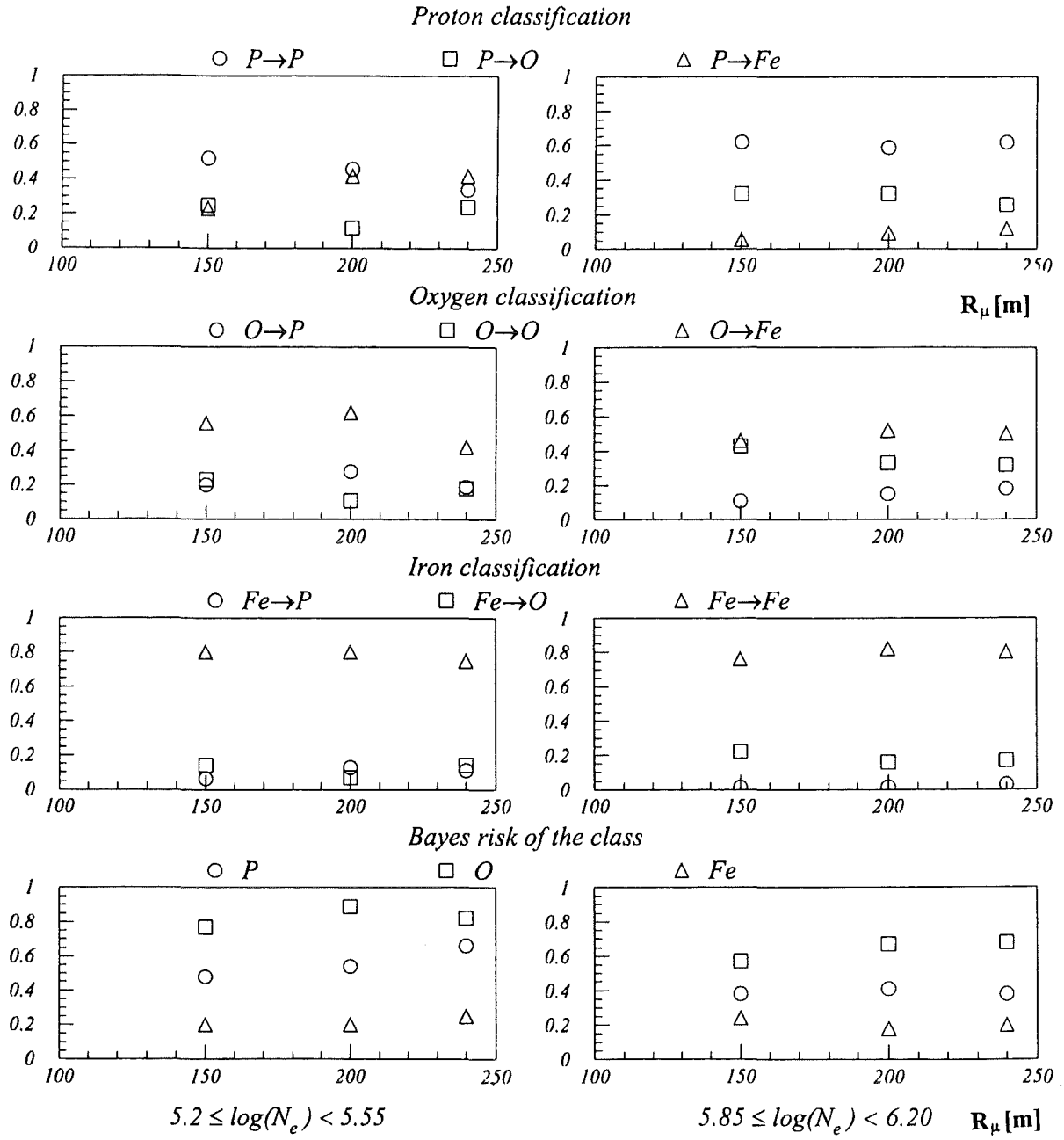

Fig. 21c: The true classification probabilities for proton, O and Fe primaries derived from the arrival time - angle correlation of the foremost muon (observed at larger distancies R_μ) for two different N_e ranges.

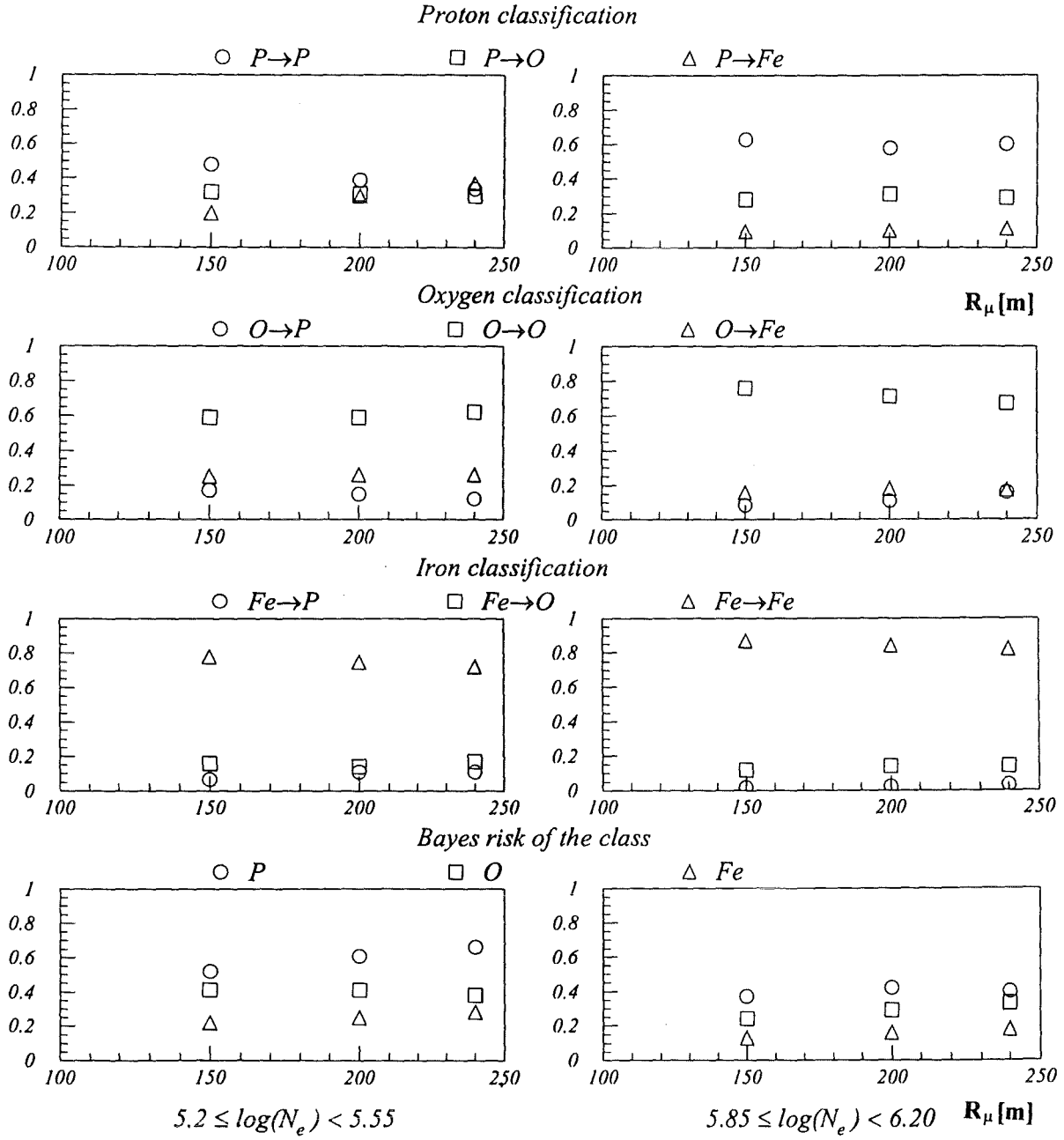

Fig. 22: The true classification probabilities for proton, O and Fe primaries derived from the arrival time - shower age correlation of the foremost muon for two different N_e ranges.

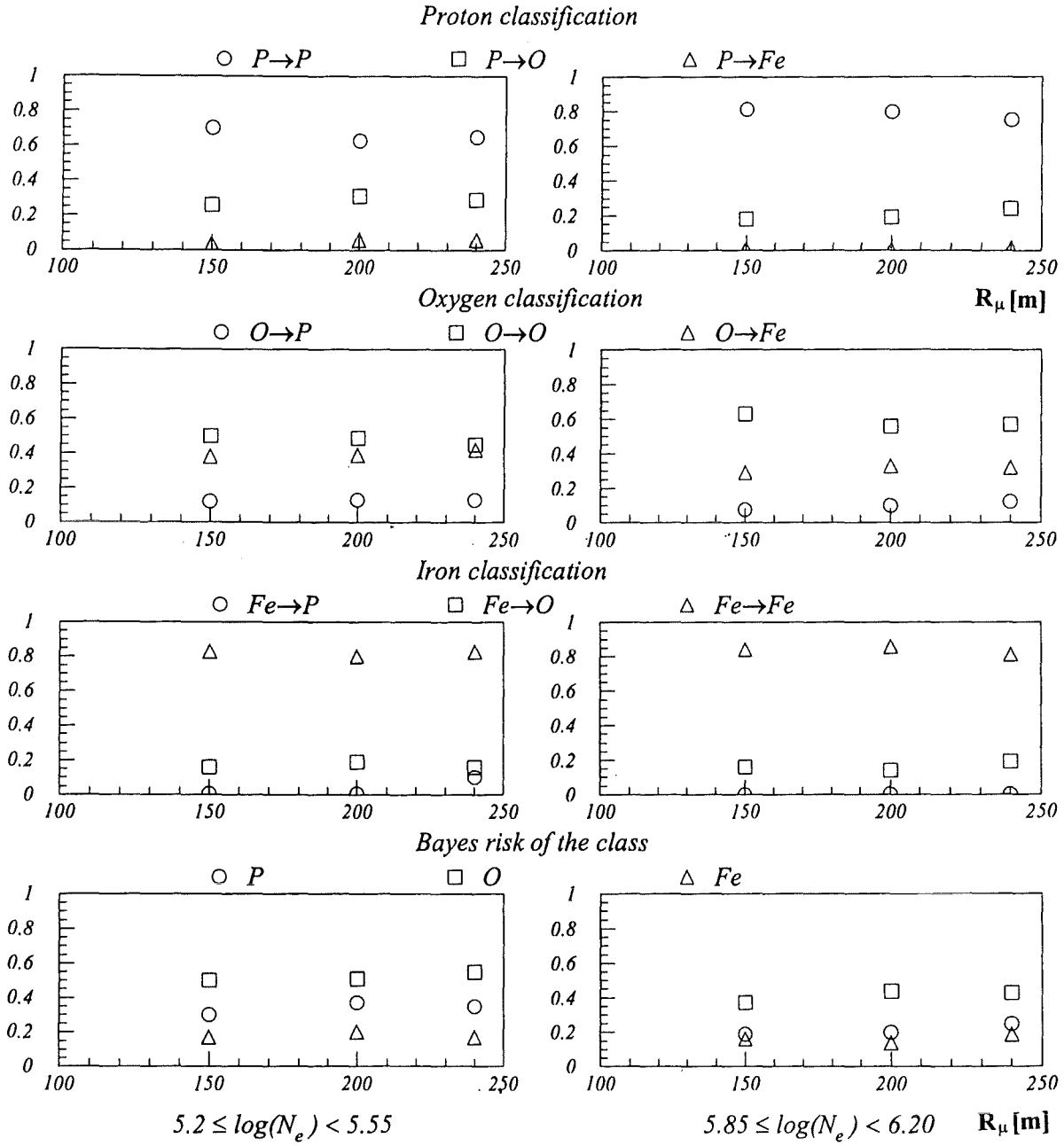

Fig. 23: The true classification probabilities for proton, O and Fe primaries derived from the arrival time - correlation of the foremost muon, observed at two different radial distances (50 m, R_μ) for two different N_e ranges.

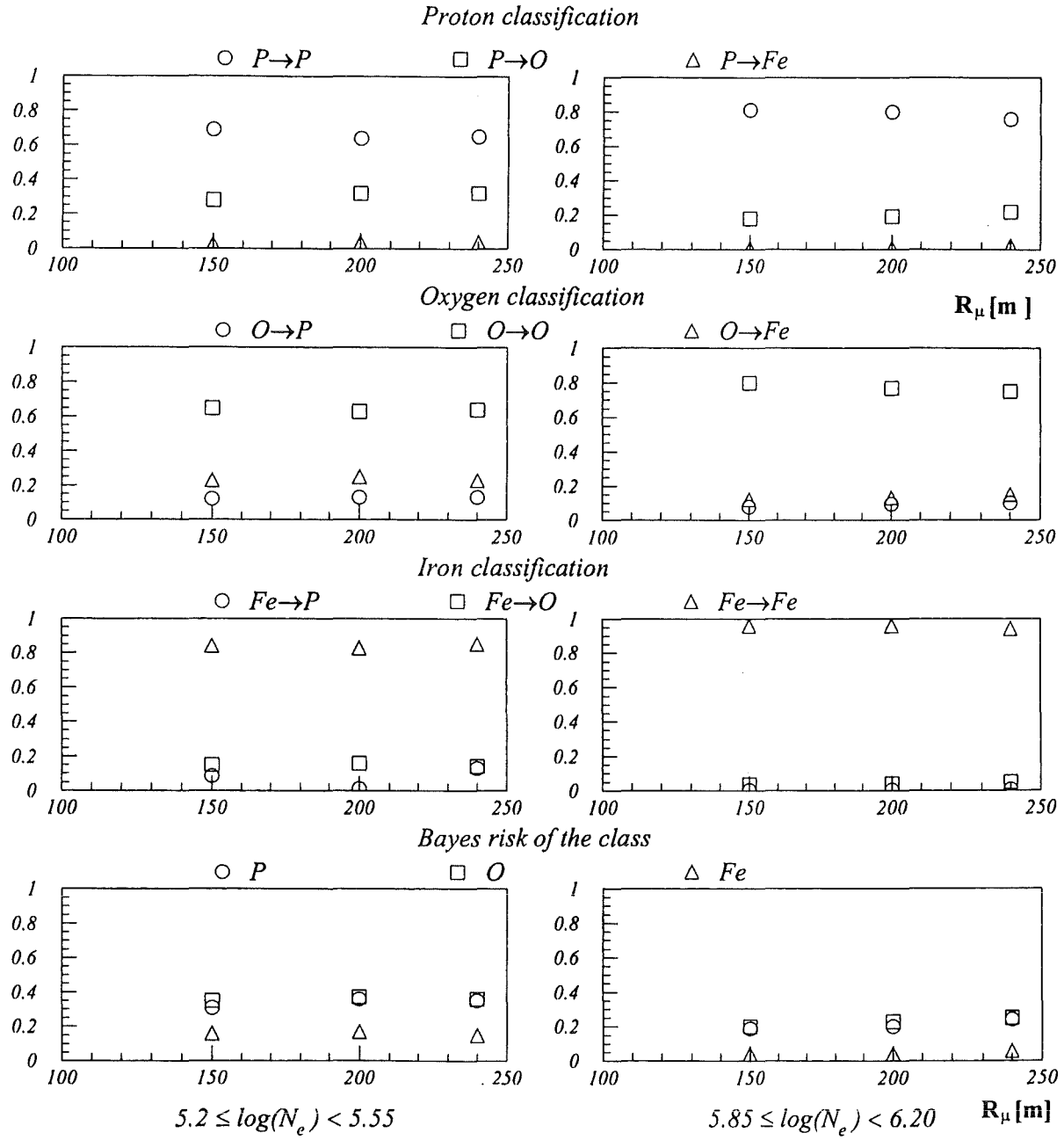

Fig. 24: The true classification probabilities for proton, O and Fe primaries derived from the shower age - arrival time - correlation of the foremost muons, observed at two different radial distances (50 m, R_μ) for two different N_e ranges.

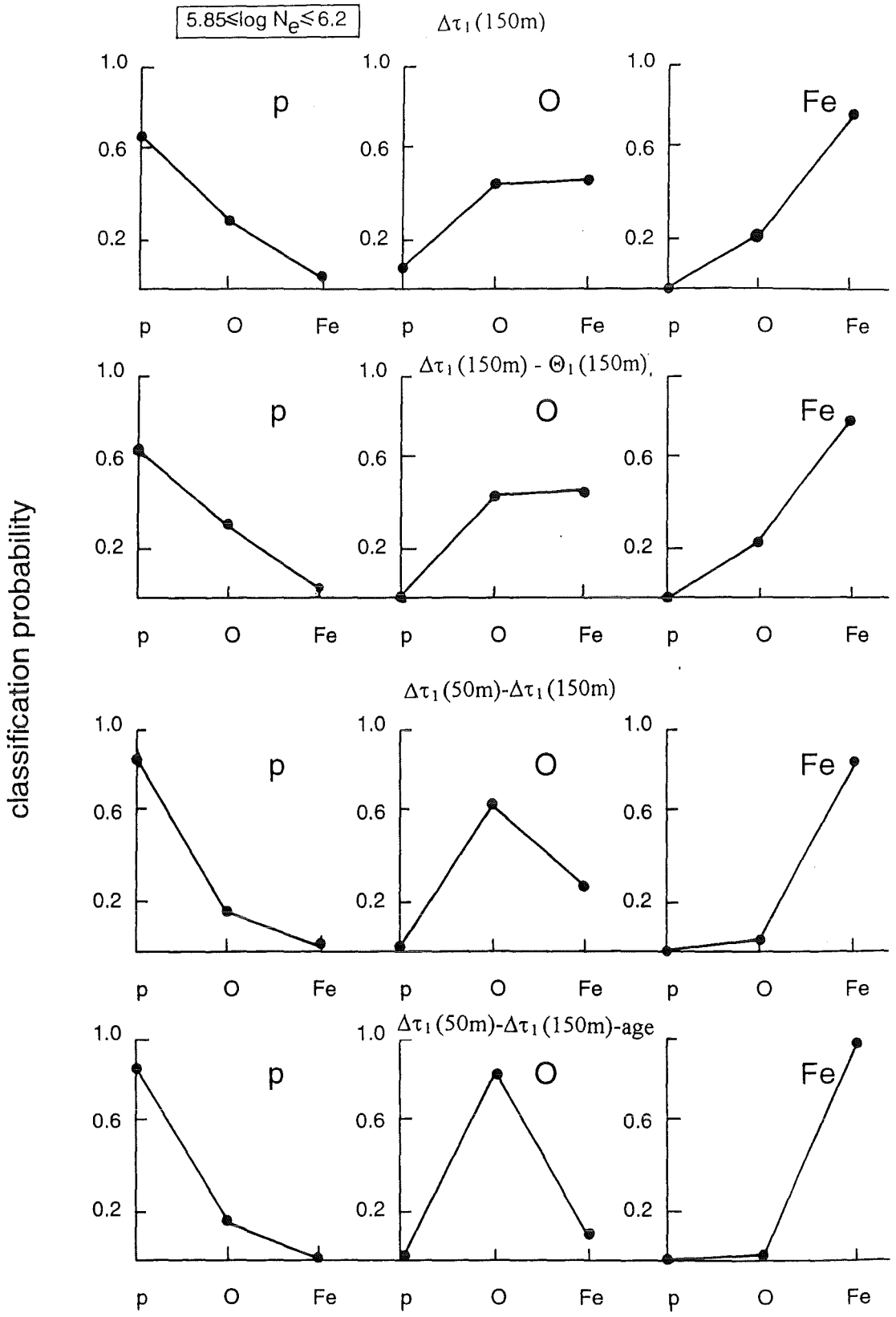

Fig. 25: Comparison of the classification and misclassification in different observation modes.

6.3 Reconstruction of the mass composition

Specified to the case of the three EAS primaries: p, O, Fe, we sketch a simple reconstruction procedure of the mass composition of a control sample with

$$N = n_p + n_O + n_{Fe} \tag{6.9}$$

events, using the classification ($P_{i\to i}$) and misclassification probabilities ($P_{j\to i}$) probabilities, derived from the likelihood functions (see Figs. 19 - 23). The correct numbers of events of a specific class are altered by

$$n'_p = P_{p\to p}\, n_p + P_{O\to p}\, n_O + P_{Fe\to p}\, n_{Fe} \tag{6.10}$$

$$n'_O = P_{p\to O}\, n_p + P_{O\to O}\, n_O + P_{Fe\to O}\, n_{Fe}$$

$$n'_{Fe} = P_{p\to Fe}\, n_p + P_{O\to Fe}\, n_O + P_{Fe\to Fe}\, n_{Fe}$$

which are interpreted as mean values of binomial distributions for the probability to find the particular class (i) among N realisations. Slightly generalising the notation we write

$$n'_i = \sum_{j=1}^{3} n_j \cdot P_{ji} \tag{6.11}$$

with the variance

$$\sigma^2_{n_i} = \sum_{j=1}^{3} n_j P_{ji}\left(1 - P_{ji}\right) \tag{6.12}$$

and

$$\sum_i^3 n'_i = \sum_j^3 n_j = N \tag{6.13}$$

In the case of an experiment, which results in an estimate of n'_p, n'_O, n'_{Fe} ... the above system of linear equations can be inverted /25/ in order to determine the true values n_p, n_O, n_{Fe} ..., provided that reliable estimate of classification and misclassification probabilities P_{ij} are available from the simulation results.

We consider the reconstruction of a 7:1:3 - p:O:Fe control sample of events induced by EAS in the N_e range: $5.85 \leq \log N_e \leq 6.20$ and express the results in terms of composition coefficients $C_i = n_i / N$.

Table 3: Results of the reconstruction procedure.

Mode	p	O	Fe
$\Delta\tau_1$ (150 m)	4.68	3.31	3.23
$\Delta\tau_1$ (150 m) - Θ_1 (150 m)	4.49	3.33	3.12
$\Delta\tau_1^{50} - \Delta\tau_1^{150}$	5.74	2.37	2.88
$\Delta\tau_1^{50} - \Delta\tau_1^{150}$-age	5.75	2.18	3.07

Table 3 presents the reconstructed mass composition from results of various observation modes and displays again the role of the correlations. The errors of this values are dominated by the Bayes risk of the classification probabilities (displayed in Figs. 21-24), while the uncertainty due to the binomial distribution of the n_i values is practically negligible with sufficient large samples (N).

7. Summary and conclusions

Studies of arrival time and angle-of-incidence distributions of muons from extensive air showers have attracted considerable interest since they are considered to be a source of information on the longitudinal EAS development and on the mass composition of cosmic rays. This information potential has recently led to some interesting proposals /5, 7, 8/ (in context with specific experimental installations), how dedicated experiments should be designed and analysed, finally with the suggestion of setting up an array of "muon-eyes" /24/, potentially establishing observation capabilities analogous to the Flye's Eye.

The present studies pursue these aspects on the basis of realistic Monte-Carlo simulations (CORSIKA) of proton, oxygen and iron nuclei induced showers in the shower size range of $\log N_e = 3.8 - 6.2$. First, the features of arrival time distributions are recalled and detailed with reference to a real detector installation (KASCADE) in order to get some insight in the role of the detector performance. In order to explore the features of arrival time and angle-of-incidence distributions of EAS muons ($E_\mu \geq 1$ GeV) in a coherent way,

we refer to hypothetical timing-tracking detectors of 10 x 10 m^2 area and consider the dependence of the distributions and their correlations on the radial distance from the shower core. Special attention is focused to simultaneous observations at different radial distances ("radial correlations"), which exhibit features improving the mass discrimination of the EAS primary. The identification of the primary mass has been attempted by a discriminant analysis, based on advanced nonparametric statistical analyses techniques and on a reconstruction procedure of the a-priori-assumed mass composition. In general, the main results can be characterised:

- Arrival time distributions and angle-of-incidence distributions show similar trends, improving the mass discrimination with increasing shower size N_e and observation distance from the shower core.

  As far as only the theoretical results of the simulations are considered (ignoring limitations by the detector qualities) the discrimination features are tentatively more pronounced by the distributions of the foremost arriving EAS muons rather than by the mean or median values of the distributions.

- There is a strong correlation of the muon arrival time distribution with the corresponding angle-of-incidence distribution, so that one type of measurements can fairly well replaced by the other (or added with improving the statistical accuracy). This feature has been reported /5/ as "Time-Tracking-Complementarity".

  However, due to the strong correlation, a combination of both type measurements does hardly improve the mass discrimination, and the application of timing or tracking or both combined is a matter of the experimental realisation and mutual checks of systematic errors.

- In contrast "radial correlations", i.e. correlated observations of the arrival time (angle-of-incidence) distributions at different distances from the shower center exhibit improvements in the mass discrimination, quantified by decreasing misclassification probabilities of the multivariate distribution analysis. A correlation with the shower age shows further distinct improvements.

Of course, the efficiency of radial correlations is increasing with the number of correlated variables and of setup detectors, located at different distances from the shower

core. Thus, finally an experimental array measuring the temporal and directional characteristics of the arriving muon component along the lateral distribution in a radial sector of the shower disc would be of great interest.

The present results evolved from a continuous discussion of the merits of arrival time and angle-of-incidence measurements in context of the KASCADE approach. We acknowledge in particular, valuable discussions with Michelangelo Ambrosio, Anatoly Erlykin, Miriam Föller, George Khristiansen, Jürgen Oehlschläger and Jürgen Wentz. We are grateful to Dieter Heck and Johannes Knapp for conmunicating us some details of the CORSIKA simulations. Special thanks to Sabine Burkhardt for her patience in preparing the many iterations of the manuscript. Two of us (I.M.B. and B.V.) thank Forschungszentrum Karlsruhe for the hospitility during their research periods as visiting scientists, when most of the calculations have been done.

References

1. H. Rebel, In "Astrophysics and Cosmology", p.121, eds. B. Sinha and R.K. Moitra, Narosa Publish. House, New Delhi, India (1995)
   I.M. Brâncus and H. Rebel, Proc. Tours Symposium on Nuclear Physics II, Tours 30.08. - 02.09.1994, France, p.78, eds. H. Utsunomiya, M. Ohta, J. Galin and G. Münzenberg
2. H. Rebel and A. Haungs, XV Cracow Summer School of Cosmology - The Cosmic Ray Mass Composition, Lodz, Poland, 15-19 July, 1996
   H. Rebel, Internal Report, Forschungszentrum Karlsruhe (1995), unpublished
3. J. Linsley, L. Scarsi and B. Rossi, Phys. Rev. **L6** (1961) 485
   J. Linsley and L. Scarsi, Phys. Rev. **128** (1962) 2384
4. Yu. Fomin and B.G. Khristiansen, Sov. Journal Nucl. Phys. **14** (1971) 360
   J.R. Patterson and A.M. Hillas, Journal Phys. G: Nucl. Phys. **9** (1983) 327
5. T.V. Danilova , D. Dumora, A.D. Erlykin and J. Procureur, Journal Phys. G: Nucl. Phys. **20** (1994) 961 - Physics of Atomic Nuclei (Yaderna Fizika) **59** (1996) 109
   D. Dumora, "Complémentarité Trace-Temps des Muons dans les Grandes Gerbes de l'Air", Thèse L'Université Bordeaux I, (Oct.1994)
6. T.J.L. McComb and K.E. Turner, Journal Phys. Soc. Japan **51** (1982) 3087
   J. Linsley, 22nd Int. Cosmic Ray Conf. (Dublin) 1991, Conf. Abstr. 2 (1991) 873 - Nuovo Cim. **15C** (1992) 321
7. G. Agnetta et al.,Nuovo Cimento **13** (1990) 391 - Nucl. Instr. Meth. **A337** (1994) 521
   M. Ambrosio et al., Nucl. Instr. Meth. **A344** (1994) 350
   M. Ambrosio, C. Aramo, L. Colesanti, A.D. Erlykin, S.K. Machavasiani, Journal Phys. G: Nucl. Part. Phys. (submitted)

8. H. Rebel, G. Völker, M. Föller and A.A. Chilingarian, Journal Phys. G: Nucl. Part. Phys. **21** (1995) 451

9. P. Doll et al., KfK Report 4686 (1990), Kernforschungszentrum Karlsruhe - Nucl. Phys. B (Proc.Suppl.) **A14** (1990) 336

10. H. Rebel - KASCADE Collaboration, Proc. VII Internat. Symposium on Very-High-Energy Cosmic Ray Interactions, Ann Arbor, Michigan, June 1992, (AIP Conf. Proc. **276**) ed. L.Jones, p. 575

11. G. Schatz, Interdiscipl. Sci. Rev. **18** (1993) 306

12. A.A. Chilingarian, Comp. Phys. Comm. **54** (1989) 381
A.A. Chilingarian and G.Z. Zazian, Nuovo Cim. **14** (1991) 381

13. J.N. Capdevielle et al., KfK Report 4998 (1992), Kernforschungszentrum Karlsruhe
J. Knapp and D. Heck, CORSIKA User's Manual, KfK Report 5196B (1993), Kernforschungszentrum Karlsruhe, Internal Report, Forschungszentrum Karlsruhe (1995), unpublished

14. H.J. Simonis and H. Rebel, Internal Report, Forschungszentrum Karlsruhe (1996), unpublished

15. A. Haungs, J. Kempa, H.J. Mathes, H. Rebel and J. Wentz, Nucl. Instr. Meth. in Physics Research **A372** (1996) 515

16. C.P. Woidneck and E. Boehm, J. Phys. A Math. Gen. **8** (1975) 997

17. K.V. Bury, "Statistical Models in Applied Science", J. Wiley & Sons, N.Y., London, Sydney, Toronto (1975), p. 299

18. P. Doll et al., Nucl. Instr. Meth. in Physics Research **A367** (1995) 120

19. P.R. Bevington, "Data Reduction and Error Analysis for Physical Sciences", Mc Graw-Hill Book Comp., NY (1969)

20. P. Desesquelles, Ann. Phys. Fr. **20** (1995) 1

21. K. Bernlöhr, Habilitation Thesis, Faculty of Physics and Astronomy, University Heidelberg (1995)

22. E. Parzen, Ann. Math. Stat. **33** (1962) 1065

23. S.M. Snappin and J.D. Knoke, Technometrics **26** (1984) 371

24. D. Dumora, A.D. Erlykin and J. Procureur, J. Phys. G: Nucl. Part. Phys. **22** (1996) 273

25 A. Chilingarian and G.Z. Zazian, Pattern. Recognition Letters **11** (1990) 781

Appendix: Supplementary displays of features of the analysis results

Fig. A 1: Variation of shower sizes associated to a definite energy of the EAS primary.

Fig. A 2 a-d: Contributions of different primary energies to a defined N_e-bin.

Fig. A 3 a-b: The dependence of the mean value $\overline{\Delta\tau}_{mean}$ and of the standard deviation σ of the *means* of the single arrival time distribution from the radial distance R_μ from the shower center. The detector efficiency and resolution corresponding to the KASCADE central detector.

Fig. A 4 a-b: The dependence of the mean value $\overline{\Delta\tau}_{median}$ and of the *medians* of the single arrival time distribution from the radial distance R_μ from the shower center. The detector efficiency and resolution corresponding to the KASCADE central detector.

Fig. A 5 a-b: Comparison of the mean values $\overline{\Delta\tau}_{mean}$ and $\overline{\Delta\tau}_{median}$ and their standard deviations of the single arrival time distributions, calculated for an (ideal) detector setup of the area 10 x 10 m^2 (chapt. 4).

Fig. A 6 a-b: Comparison of the mean values $\overline{\Theta}_{mean}$ and $\overline{\Theta}_{median}$ and their standard deviations fo the single angle-of-incidence distributions, calculatd for an (ideal) detector setup of the area 10 x 10 m^2.

Fig. A 7 a: Mean and standard deviation of the arrival time and angle-of-incidence distributions of the foremost muon ($5.20 \leq \log N_e \leq 5.85$).

Fig. A 7 b: Mean and standard deviation of the single *mean* arrival time and angle-of-incidence distributions ($5.20 \leq \log N_e \leq 5.85$).

Fig. A 7 c: Mean and standard deviation of the single *median* arrival time and angle-of-incidence distributions ($5.20 \leq \log N_e \leq 5.85$).

Fig. A 7 d: Mean and standard deviation of the single *median* arrival time and angle-of-incidence distributions ($5.85 \leq \log N_e \leq 6.20$).

Fig. A 8 a-b: Energy threshold effects on the arrival time distributions of EAS muons.

Fig. A 9 : Values of the correlation coefficient of correlated arrival time distributions $\left(R_\mu^1 = 50\ \text{m},\ R_\mu^2 = R_\mu\right)$ and of the arrival time-angle-of-incidence distributions at the same place for the foremost muons.

Fig. A 10 a-c: Values of the correlation coefficient for correlated distribution, observed with the timing-tracking detectors at different distances R_μ from the shower core a) first detector at R_μ = 50 m b) first detector at R_μ = 100 m c) triple correlation with the first two detectors at $R_\mu^1 = 50\ \text{m},\ R_\mu^2 = 100\ \text{m}$.

Fig. A 11 a-c: Distributions of the quantities h_1 and h_2, derived from the arrival time and angle-of-incidence distributions for proton and iron induced EAS.

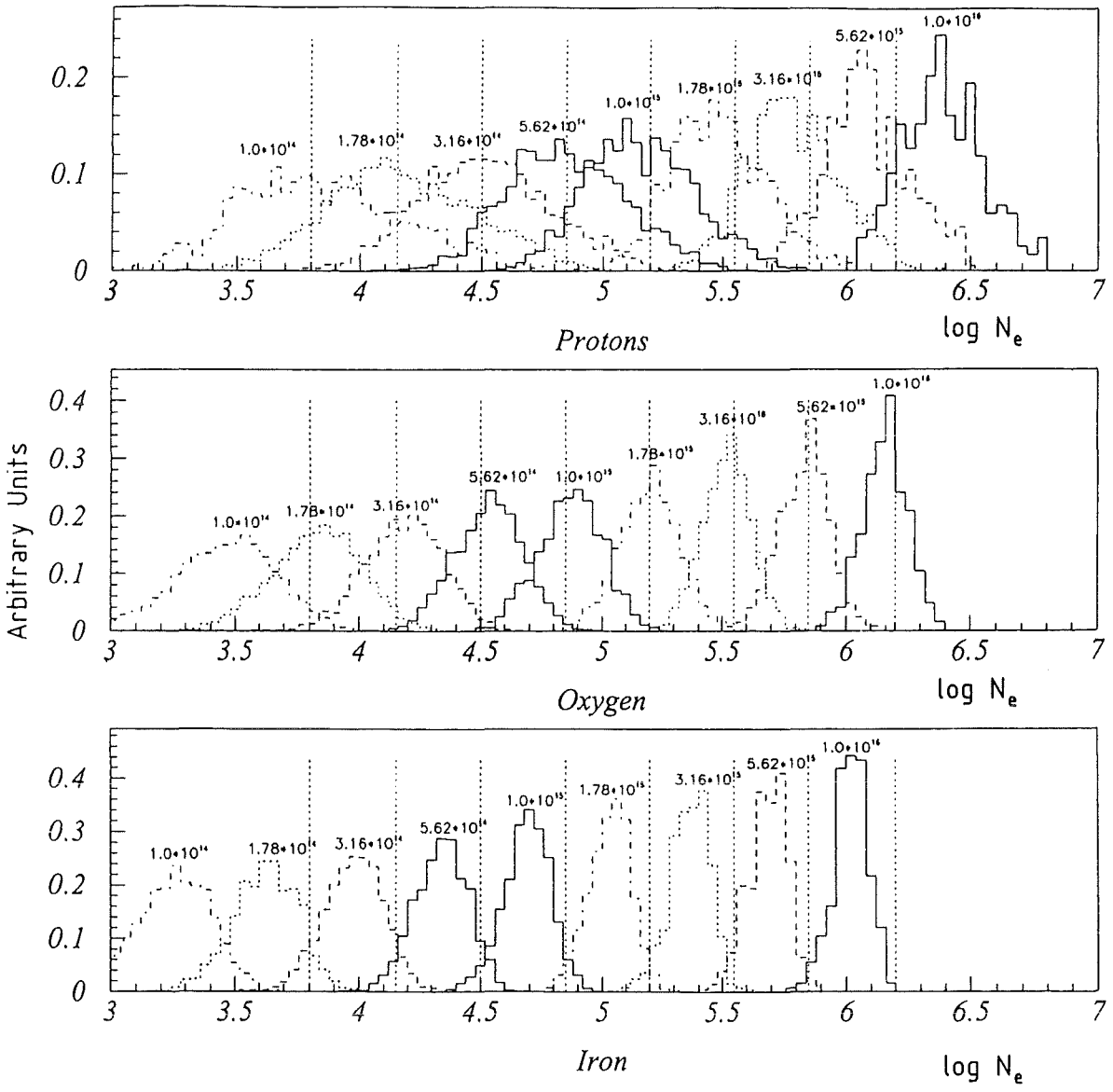
Arbitrary Units
Protons
Oxygen
Iron
log N_e
$1.0 \cdot 10^{14}$
$1.78 \cdot 10^{14}$
$3.16 \cdot 10^{14}$
$5.62 \cdot 10^{14}$
$1.0 \cdot 10^{15}$
$1.78 \cdot 10^{15}$
$3.16 \cdot 10^{15}$
$5.62 \cdot 10^{15}$
$1.0 \cdot 10^{16}$

Fig. A 1

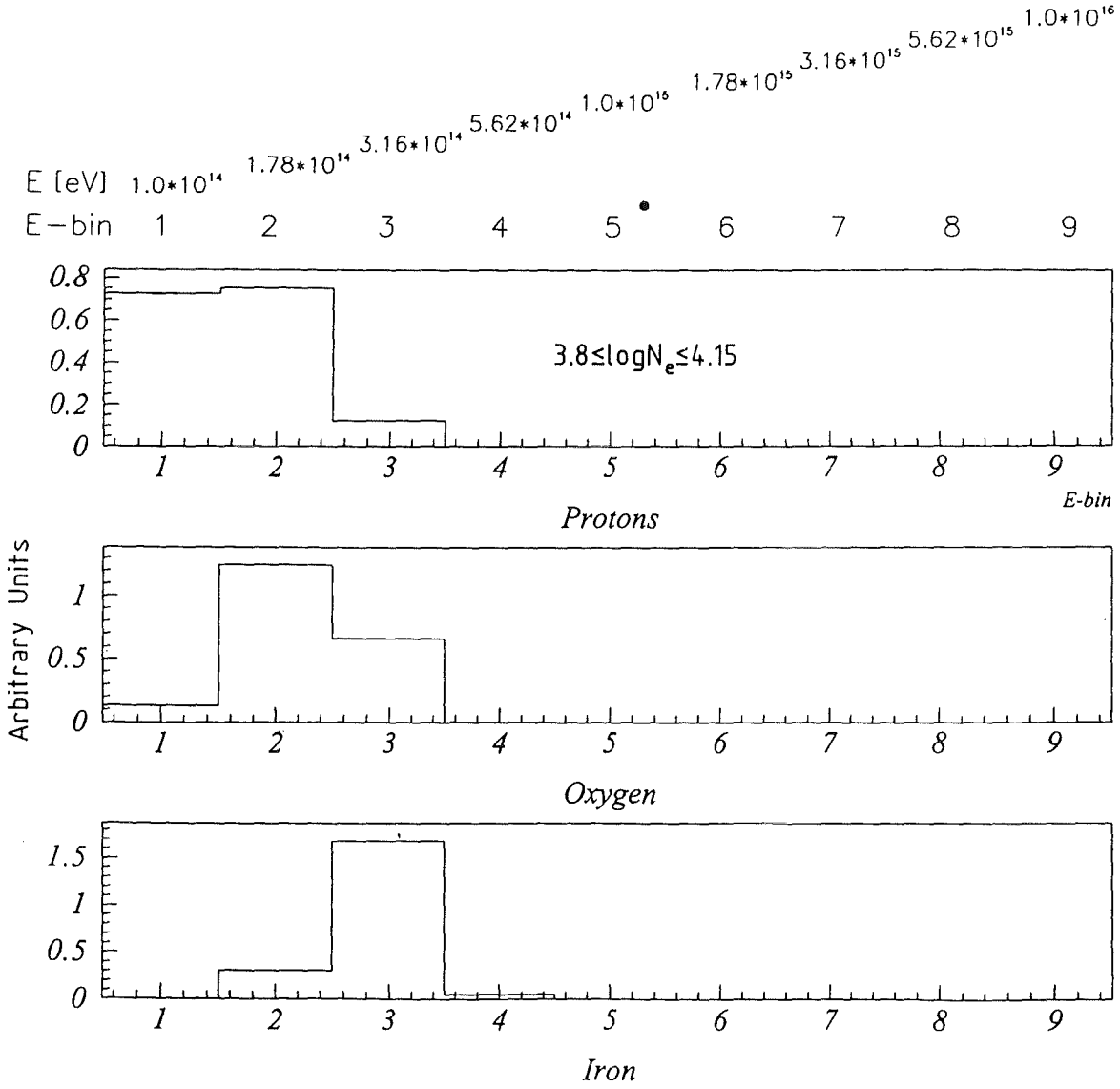
E [eV] 1.0*10^14 1.78*10^14 3.16*10^14 5.62*10^14 1.0*10^15 1.78*10^15 3.16*10^15 5.62*10^15 1.0*10^16
E-bin 1 2 3 4 5 6 7 8 9
3.8≤logN_e≤4.15
E-bin
Protons
Arbitrary Units
Oxygen
Iron

Fig. A 2 a

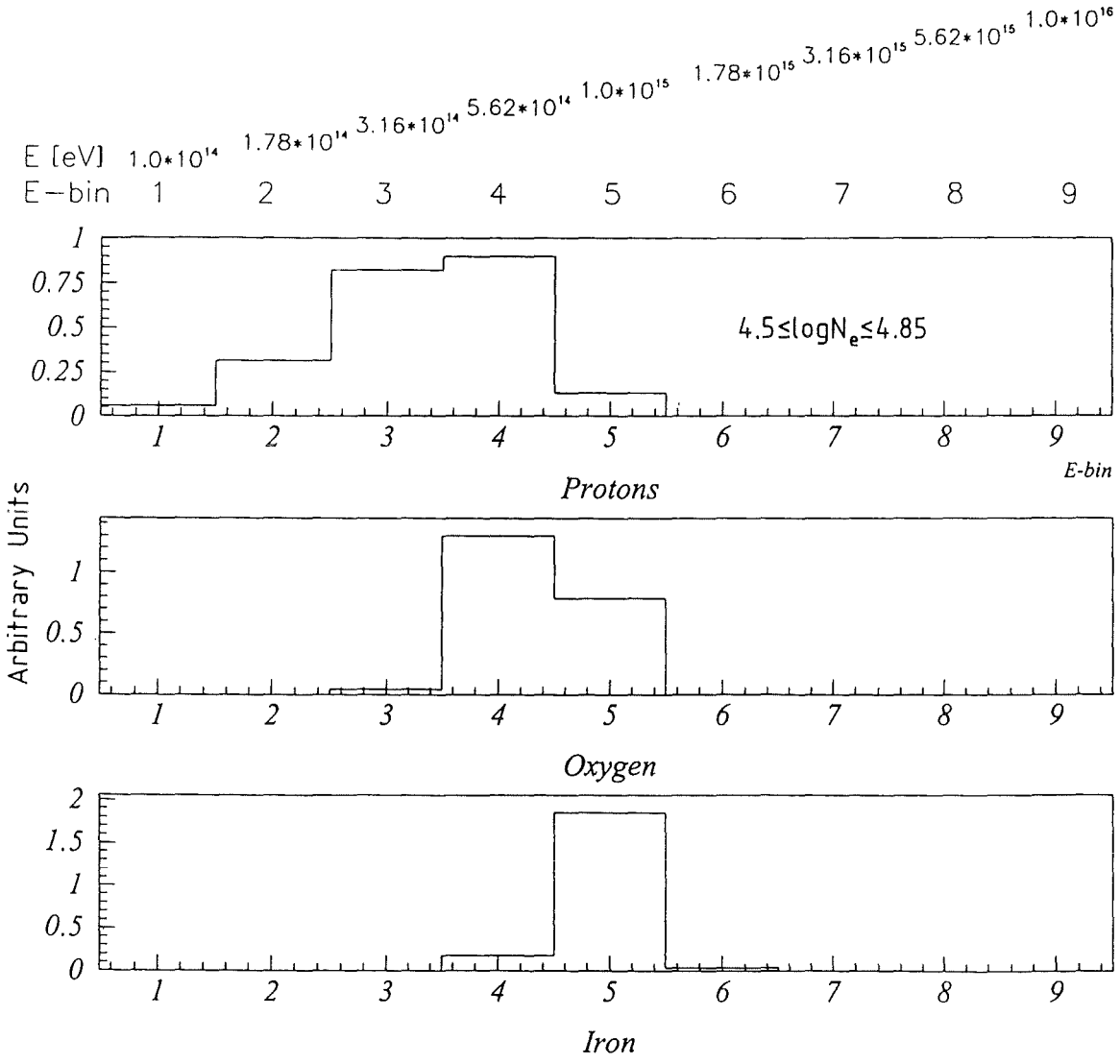
E [eV] 1.0*10^14 1.78*10^14 3.16*10^14 5.62*10^14 1.0*10^15 1.78*10^15 3.16*10^15 5.62*10^15 1.0*10^16
E-bin 1 2 3 4 5 6 7 8 9
4.5≤logN_e≤4.85
E-bin
Protons
Arbitrary Units
Oxygen
Iron

Fig. A 2 b

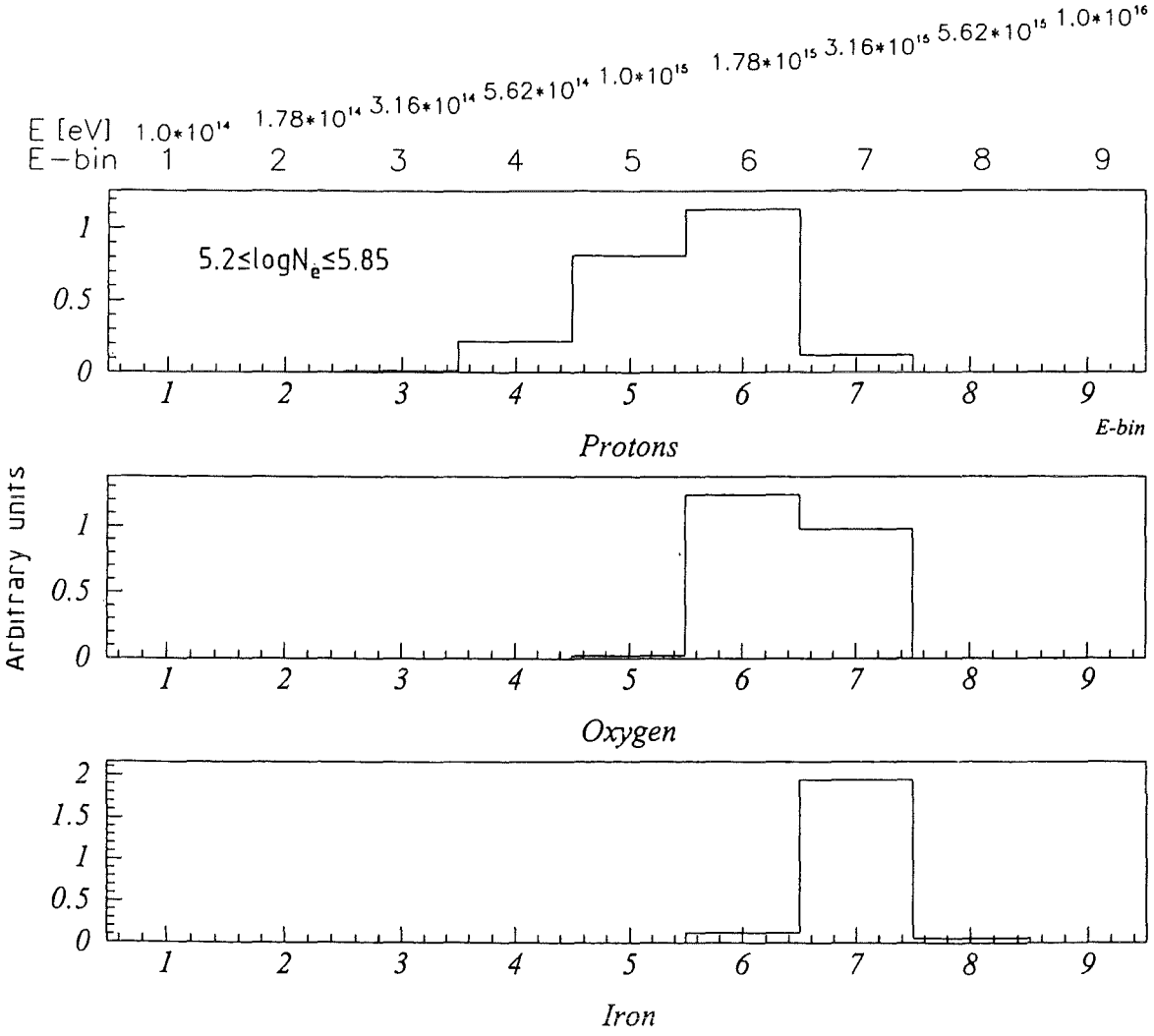
E [eV] 1.0*10^14 1.78*10^14 3.16*10^14 5.62*10^14 1.0*10^15 1.78*10^15 3.16*10^15 5.62*10^15 1.0*10^16
E-bin 1 2 3 4 5 6 7 8 9
5.2≤logN_e≤5.85
Protons
E-bin
Arbitrary units
Oxygen
Iron

Fig. A 2 c

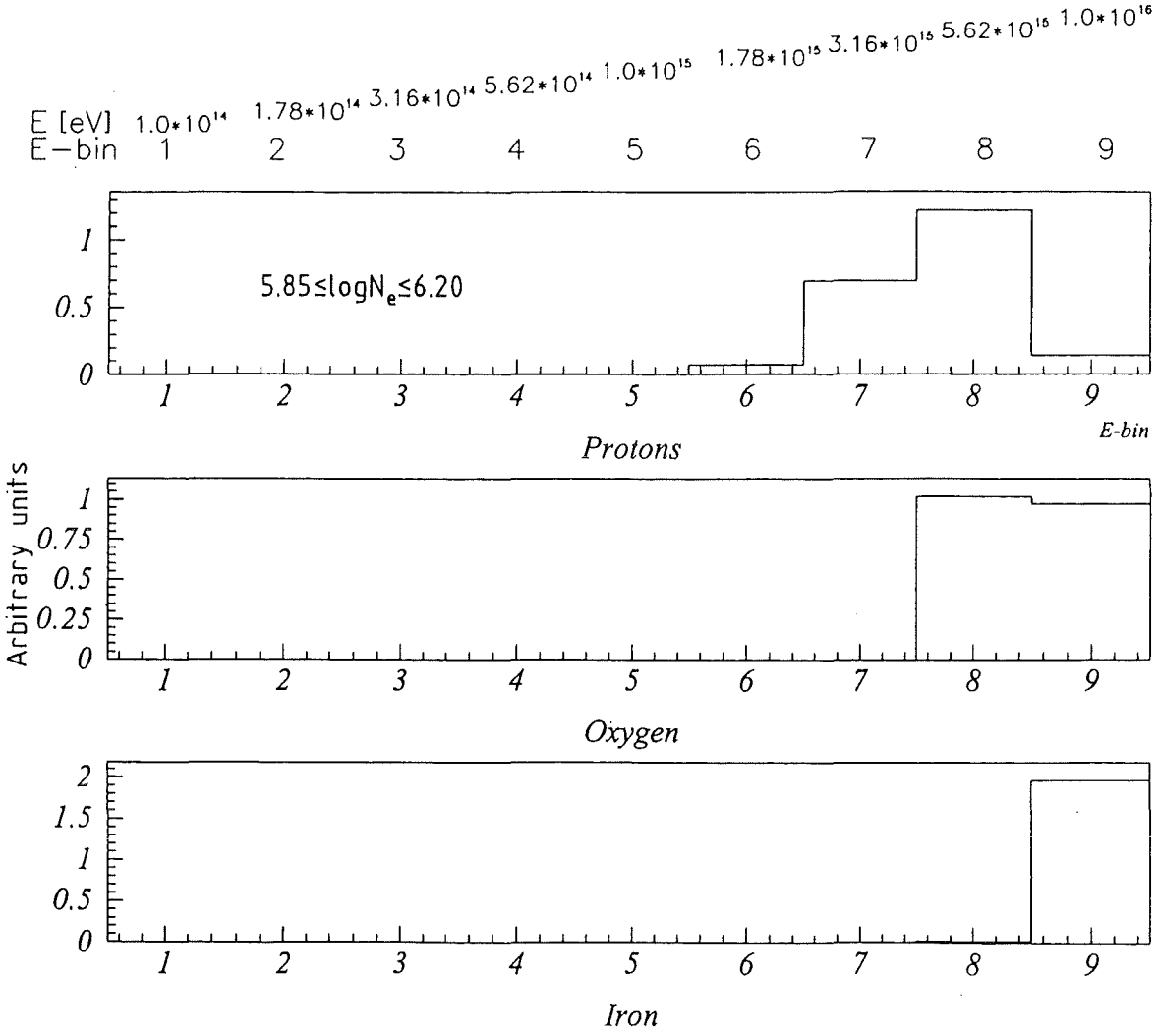
E [eV] 1.0*10^14 1.78*10^14 3.16*10^14 5.62*10^14 1.0*10^15 1.78*10^15 3.16*10^15 5.62*10^15 1.0*10^16
E−bin 1 2 3 4 5 6 7 8 9
5.85≤logN_e≤6.20
Protons
E-bin
Arbitrary units
Oxygen
Iron

Fig. A 2 d

$4.5 \leq \log(N_e) \leq 4.85$

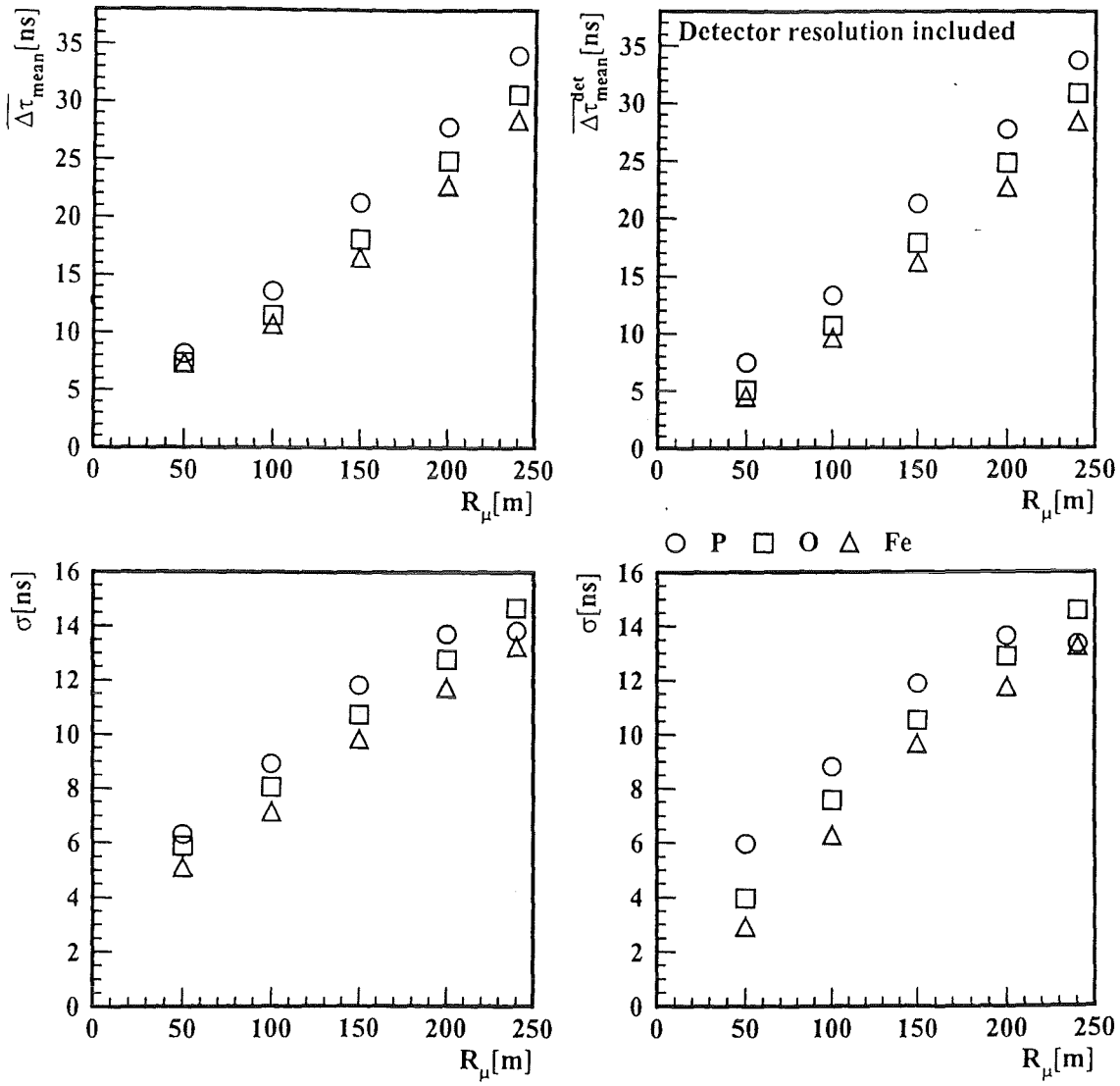

Fig. A 3 a

$5.85 \leq \log(N_e) \leq 6.2$

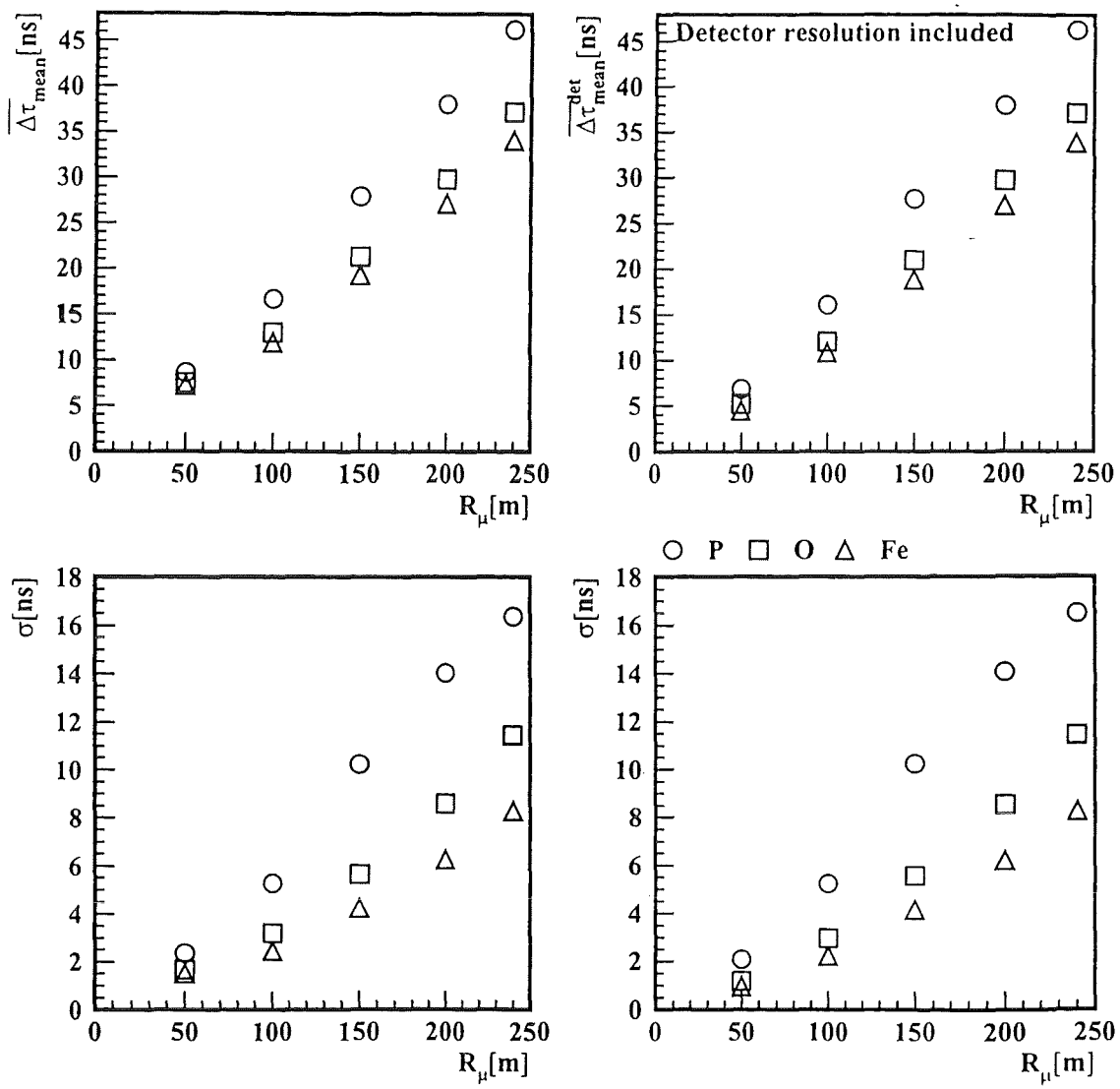

Fig. A 3 b

$4.5 \leq \log(N_e) \leq 4.85$

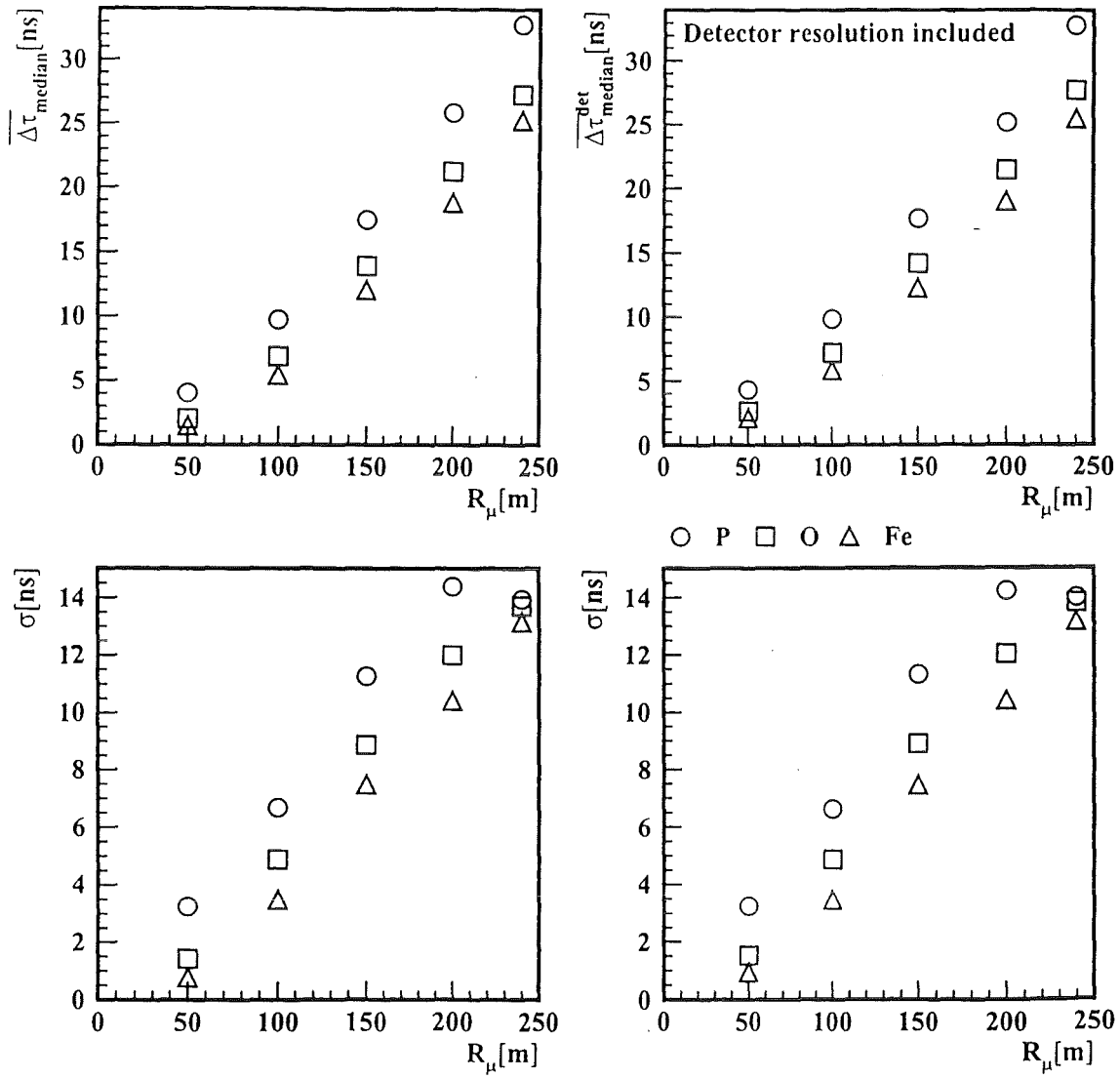

Fig. A 4 a

$$5.85 \leq \log(N_e) \leq 6.2$$

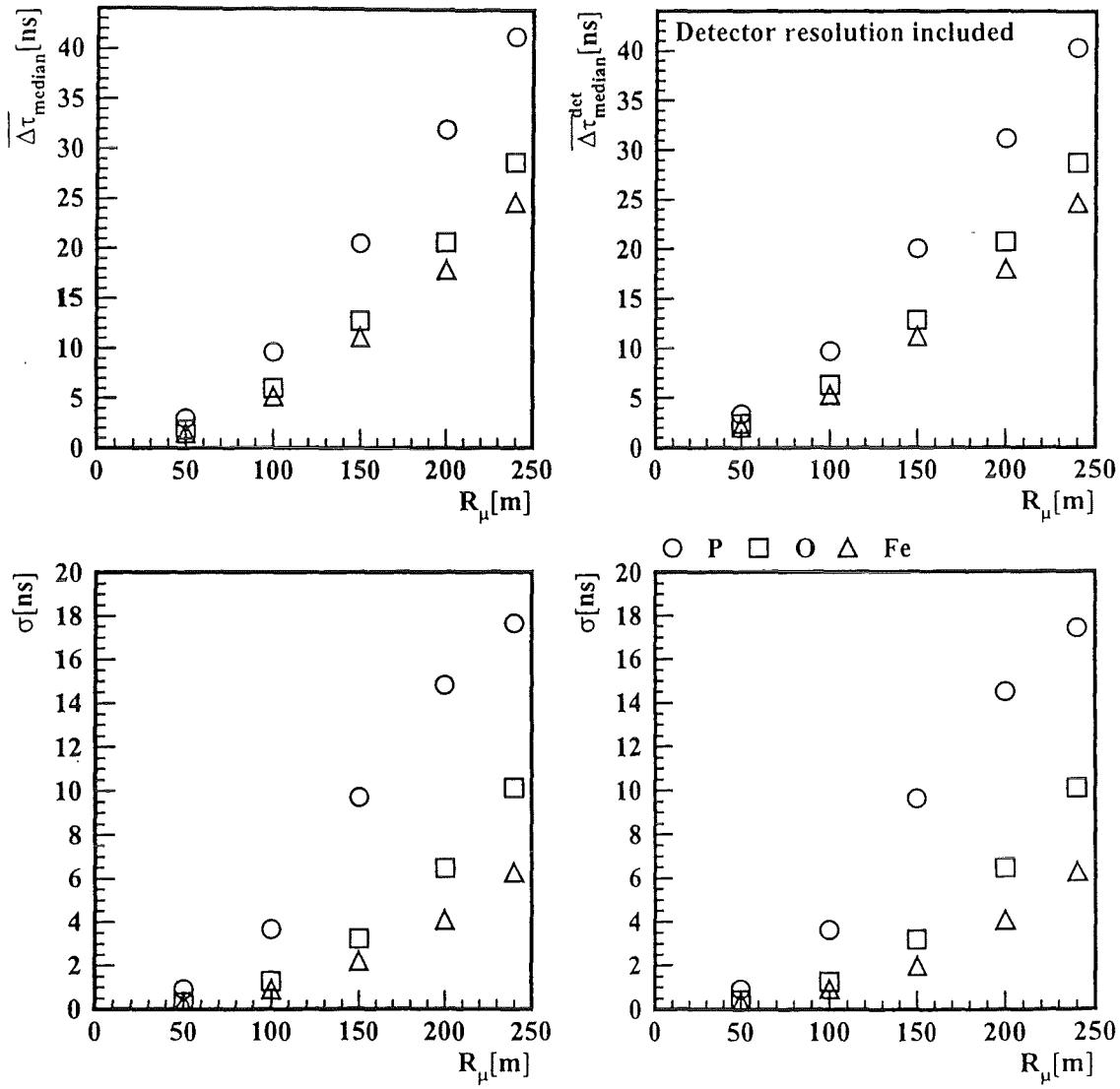

Fig. A 4 b

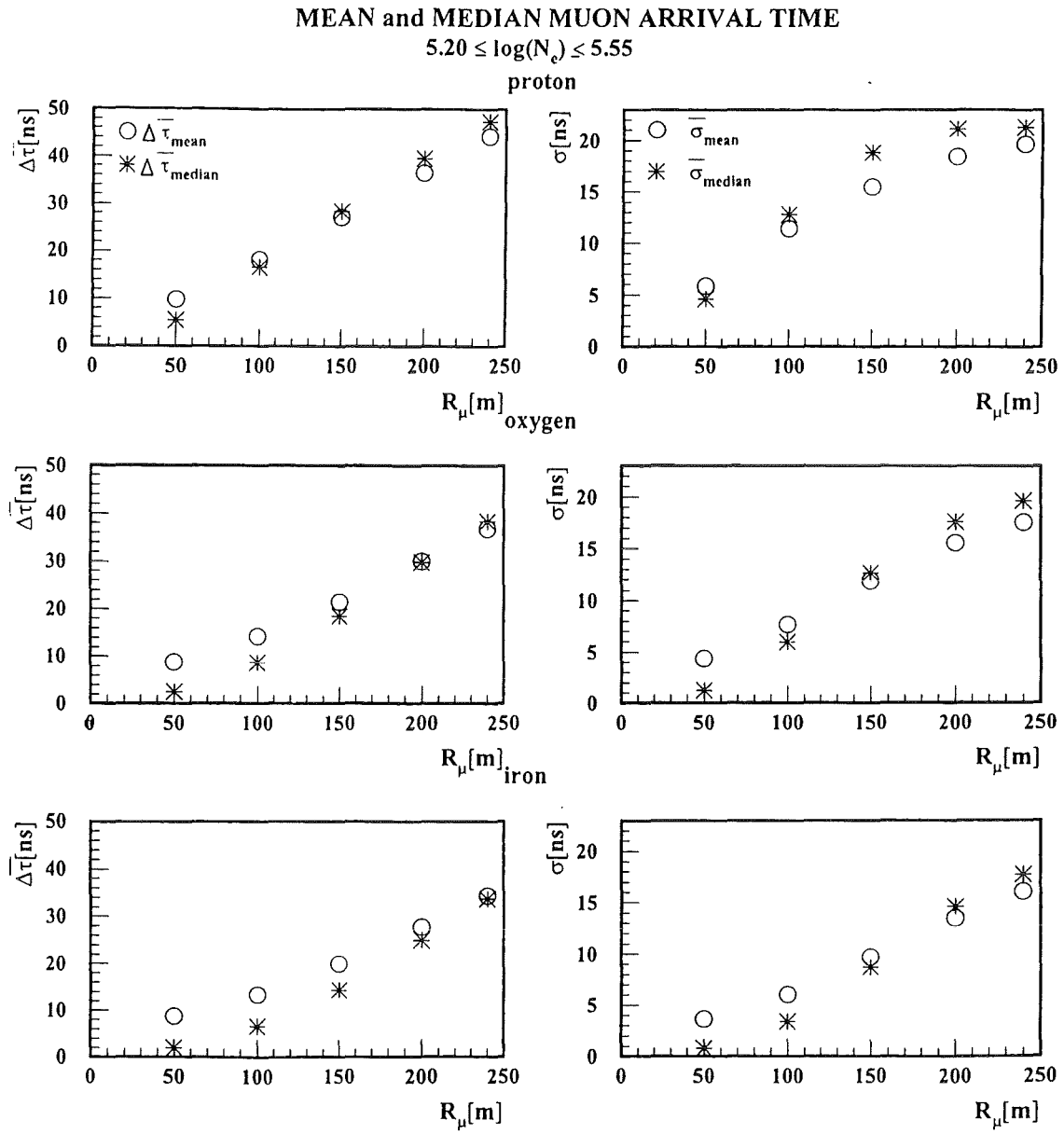
MEAN and MEDIAN MUON ARRIVAL TIME
5.20 ≤ log(N_e) ≤ 5.55
proton
Δτ̄[ns]
σ̄[ns]
Δτ̄_mean
Δτ̄_median
σ̄_mean
σ̄_median
R_μ[m]
oxygen
iron

Fig. A 5 a

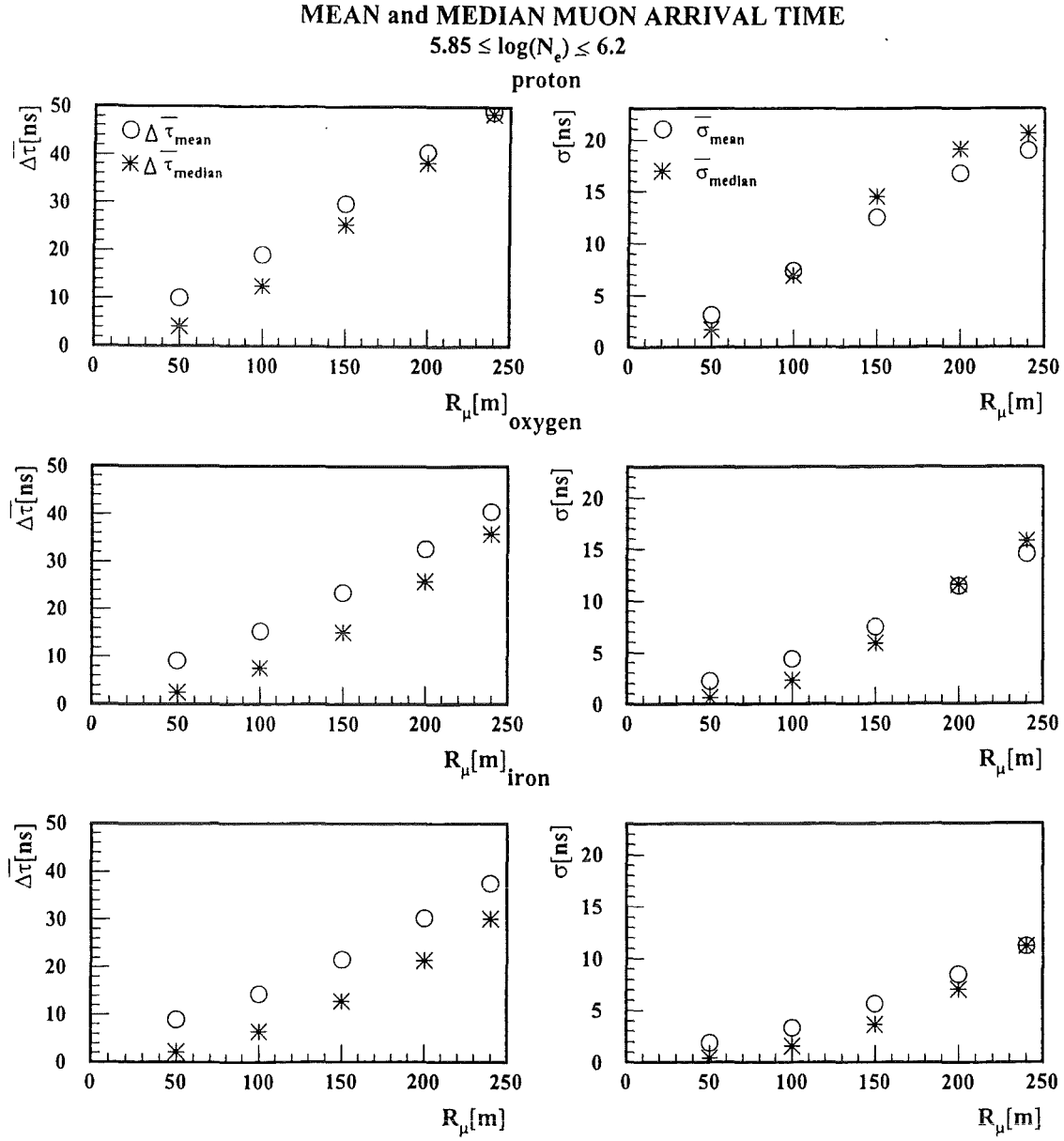
MEAN and MEDIAN MUON ARRIVAL TIME
5.85 ≤ log(N_e) ≤ 6.2
proton
Δτ̄[ns]
σ[ns]
Δτ̄_mean
Δτ̄_median
σ̄_mean
σ̄_median
R_μ[m]
oxygen
iron

Fig. A 5 b

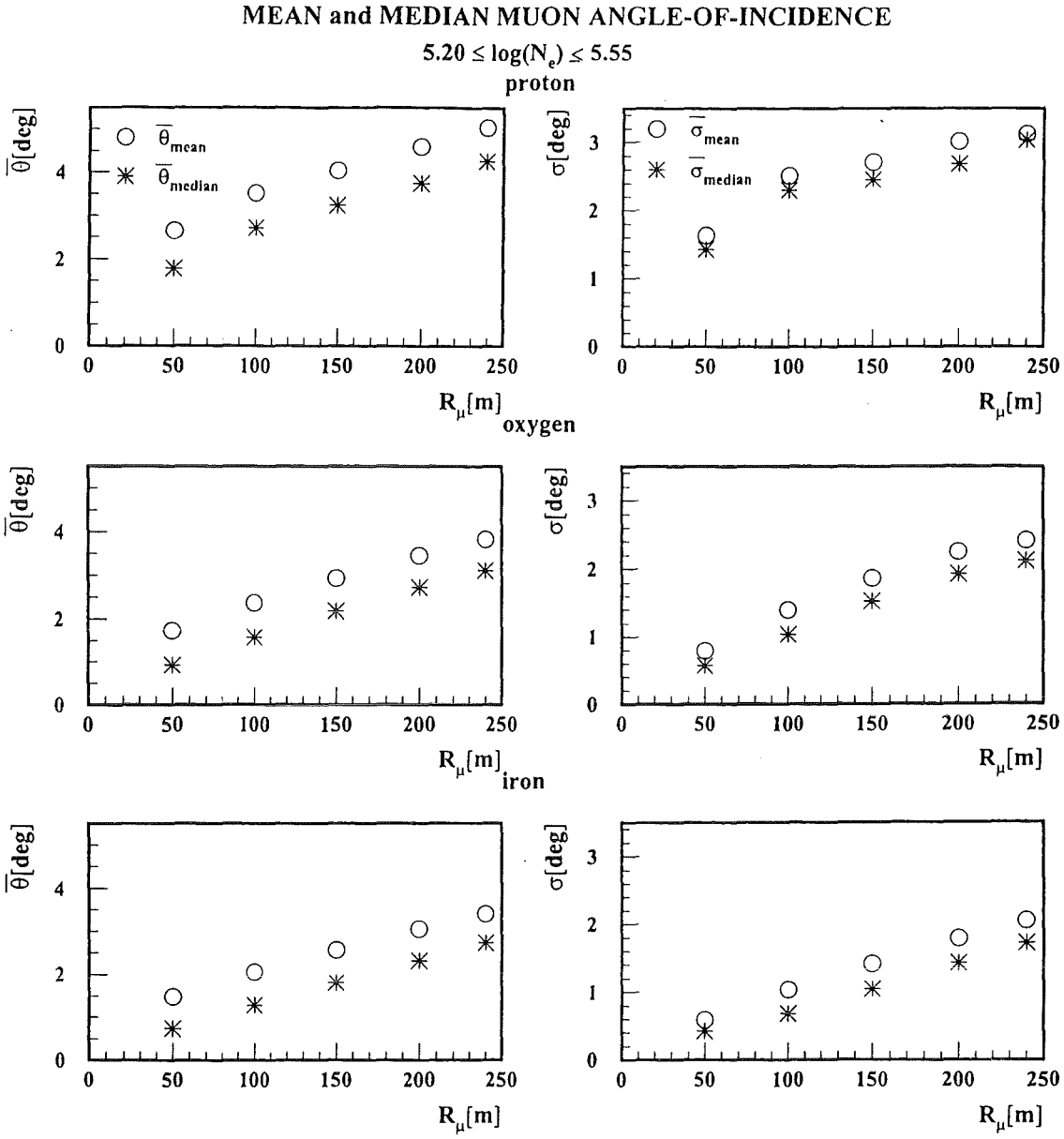
MEAN and MEDIAN MUON ANGLE-OF-INCIDENCE
5.20 ≤ log(N_e) ≤ 5.55
proton
oxygen
iron
θ̄[deg]
σ̄[deg]
θ̄_mean
θ̄_median
σ̄_mean
σ̄_median
R_μ[m]
0
50
100
150
200
250
1
2
3
4

Fig. A 6 a

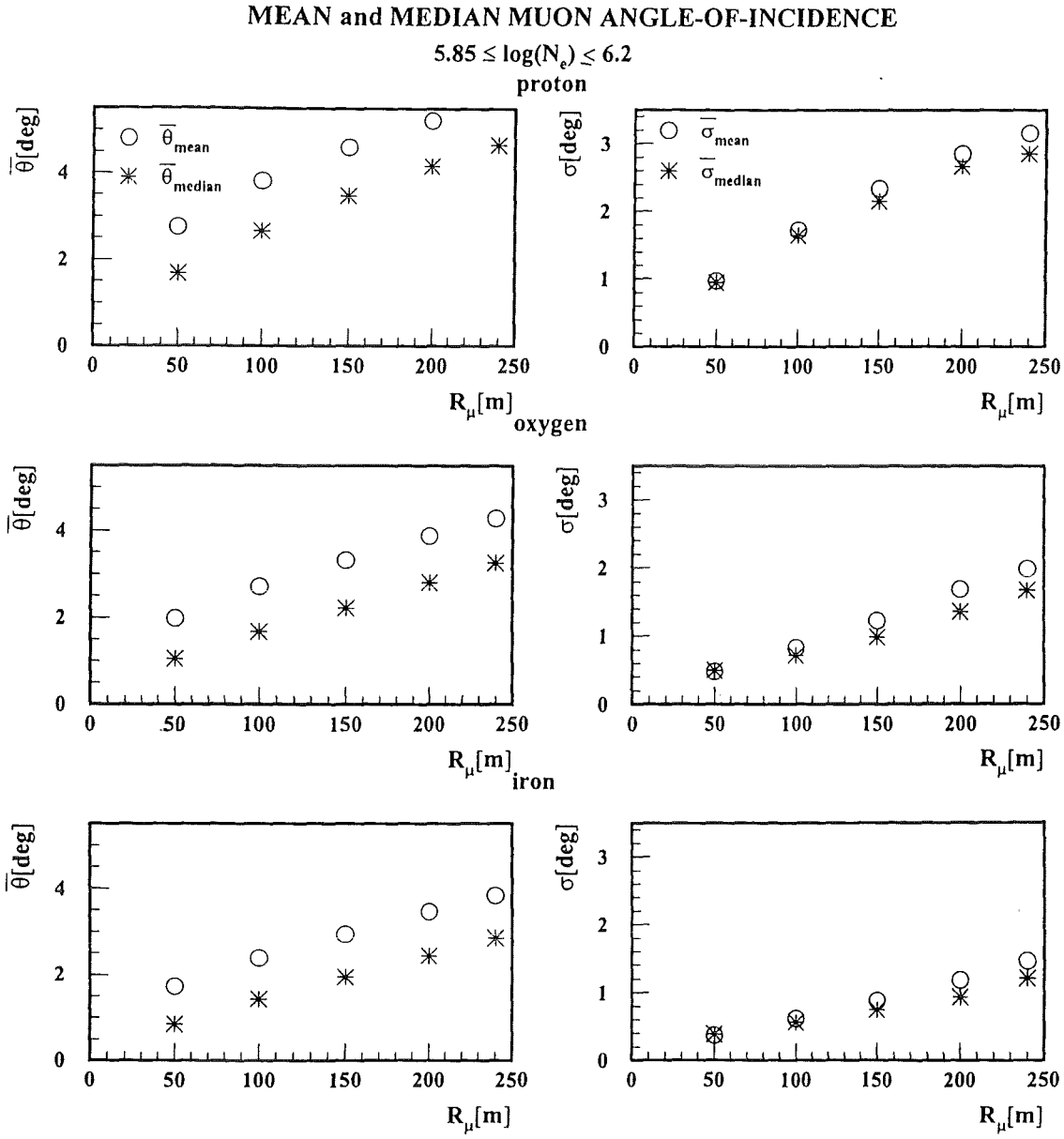
MEAN and MEDIAN MUON ANGLE-OF-INCIDENCE
5.85 ≤ log(N_e) ≤ 6.2
proton
oxygen
iron
θ̄[deg]
σ̄[deg]
θ̄_mean
θ̄_median
σ̄_mean
σ̄_median
R_μ[m]
0
50
100
150
200
250
1
2
3
4

Fig. A 6 b

ANALYSIS OF ARRIVAL TIME AND ANGLE-OF-INCIDENCE

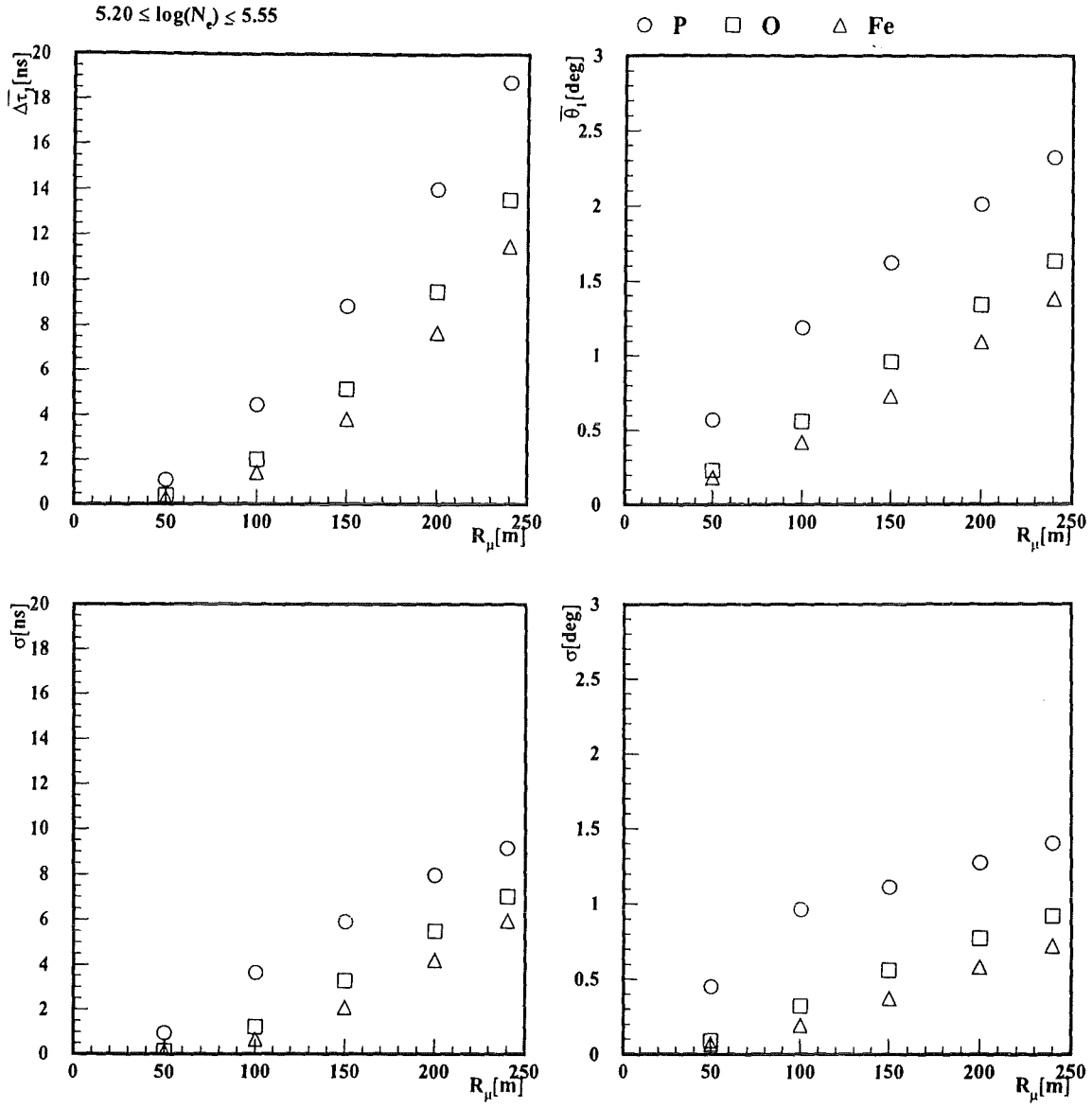

Fig. A 7 a

ANALYSIS OF ARRIVAL TIME AND ANGLE-OF-INCIDENCE

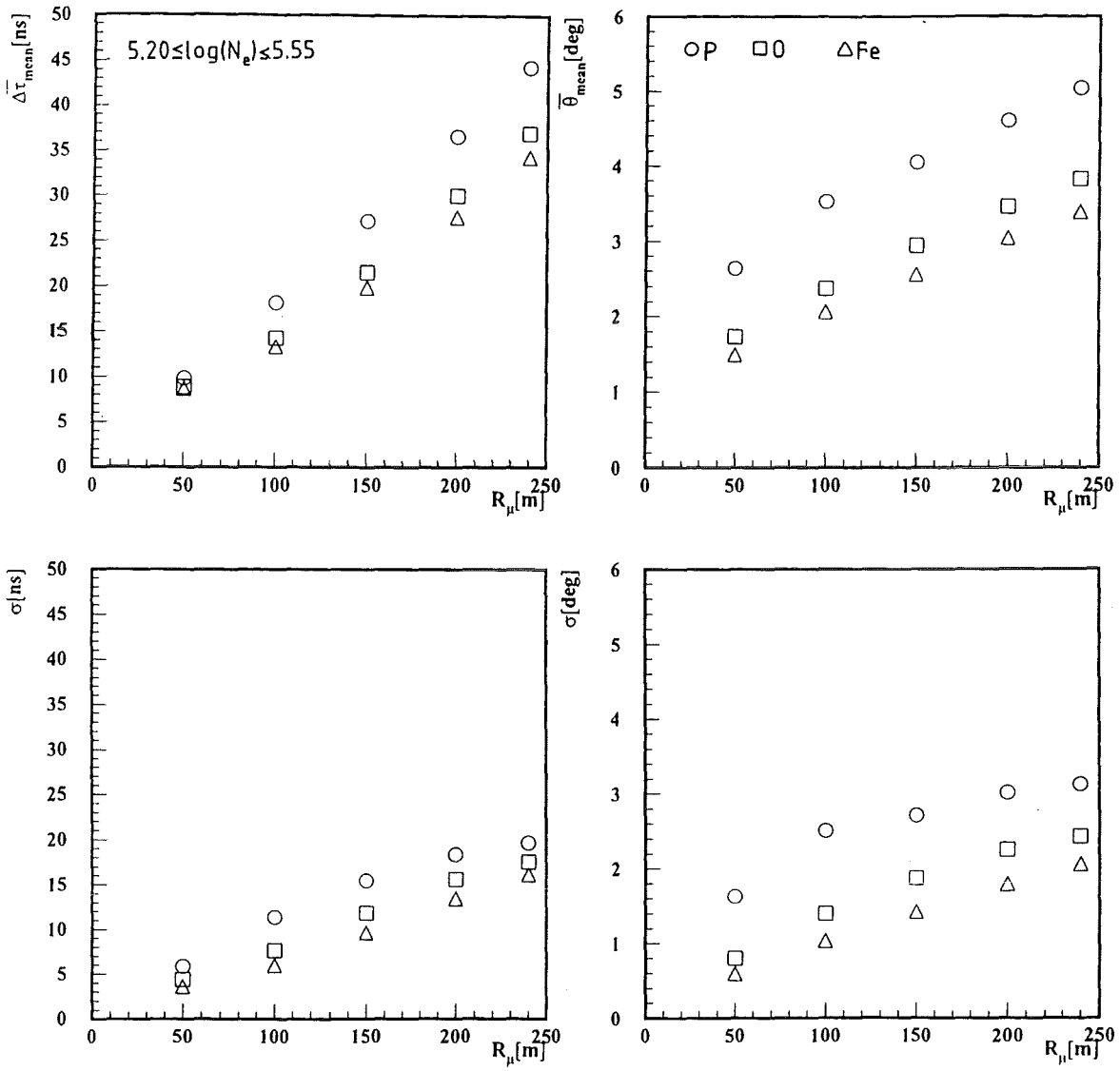

Fig. A 7 b

ANALYSIS OF ARRIVAL TIME AND ANGLE-OF-INCIDENCE

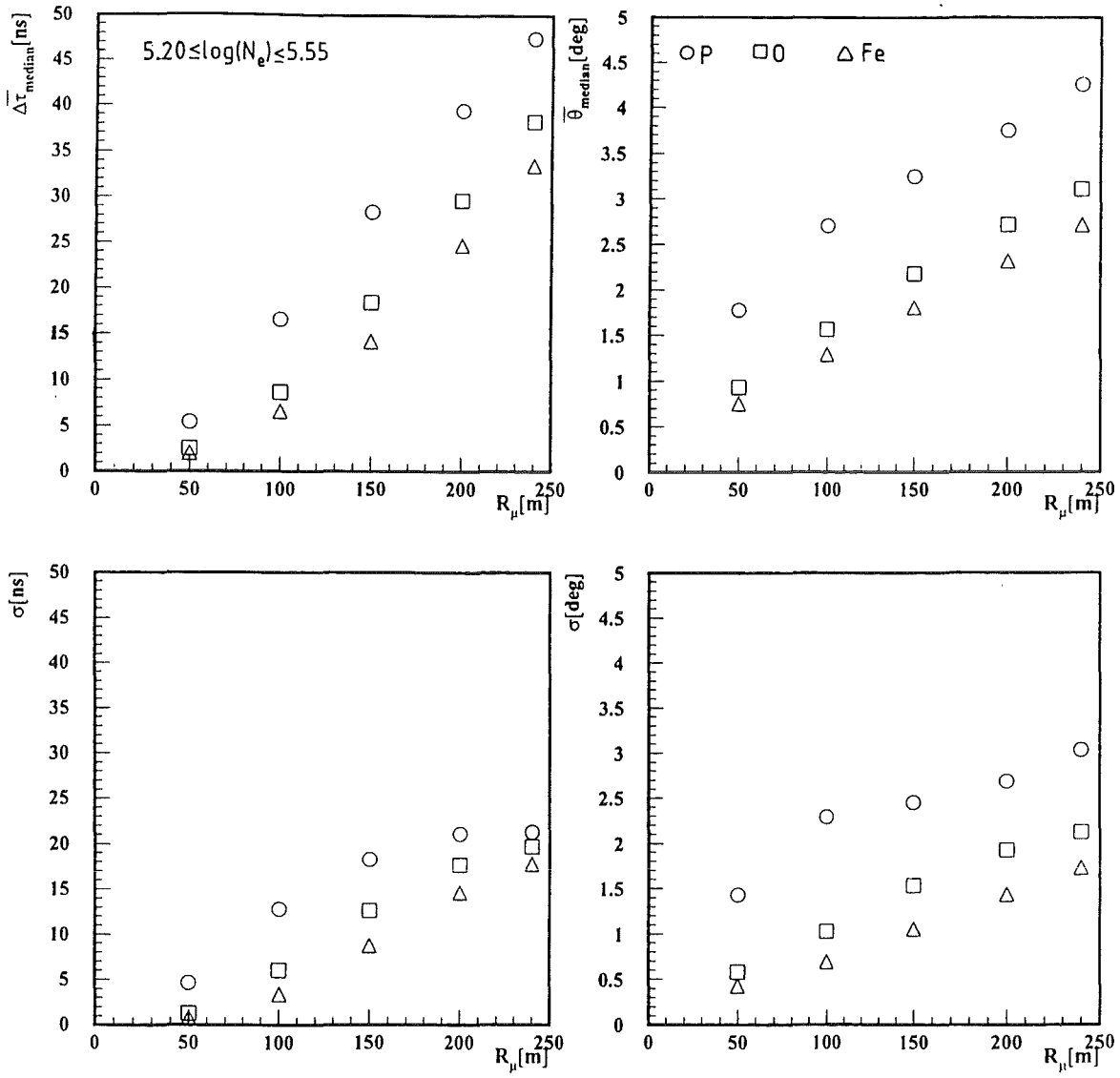

Fig. A 7 c

ANALYSIS OF ARRIVAL TIME AND ANGLE-OF-INCIDENCE

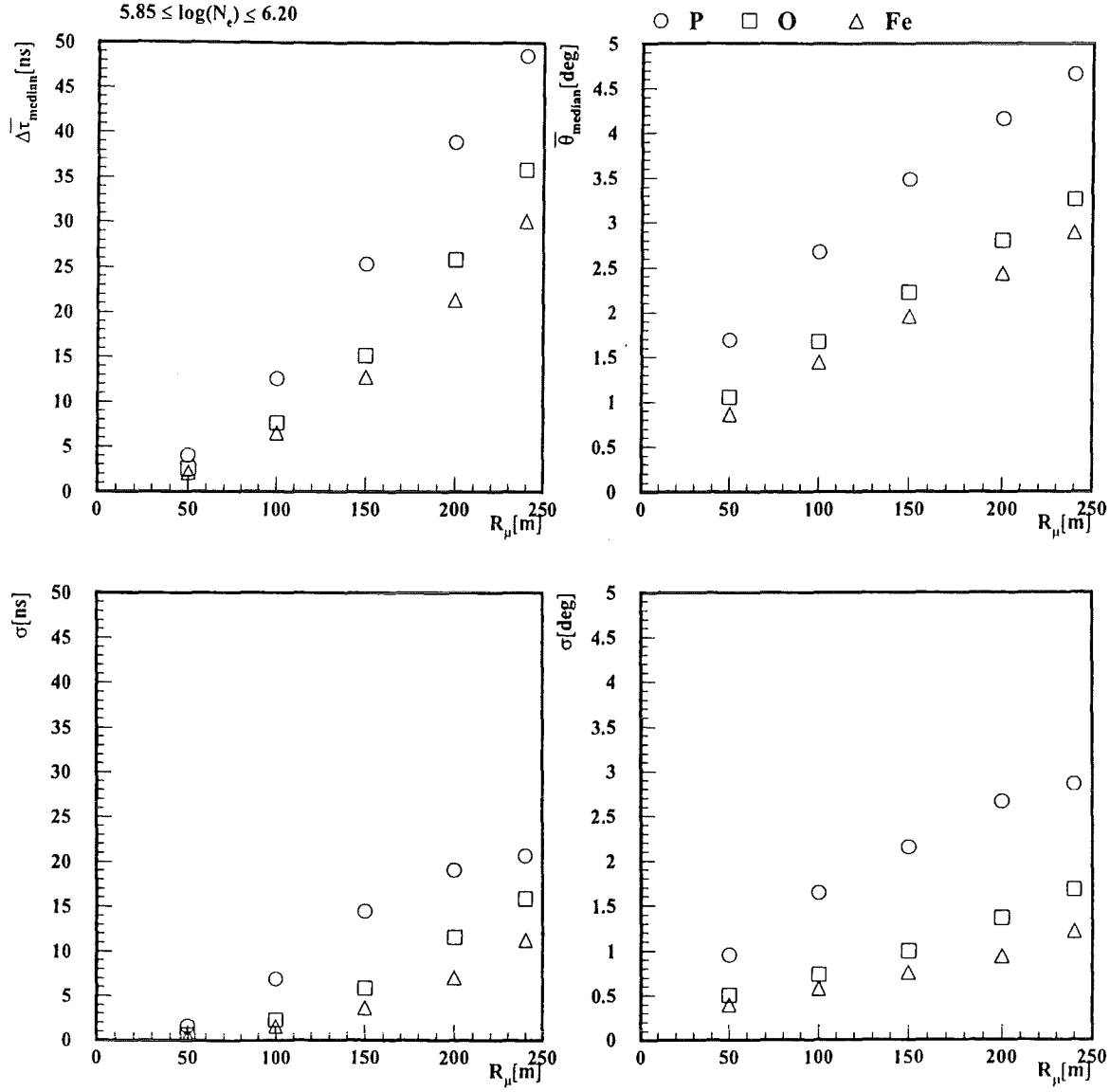

Fig. A 7 d

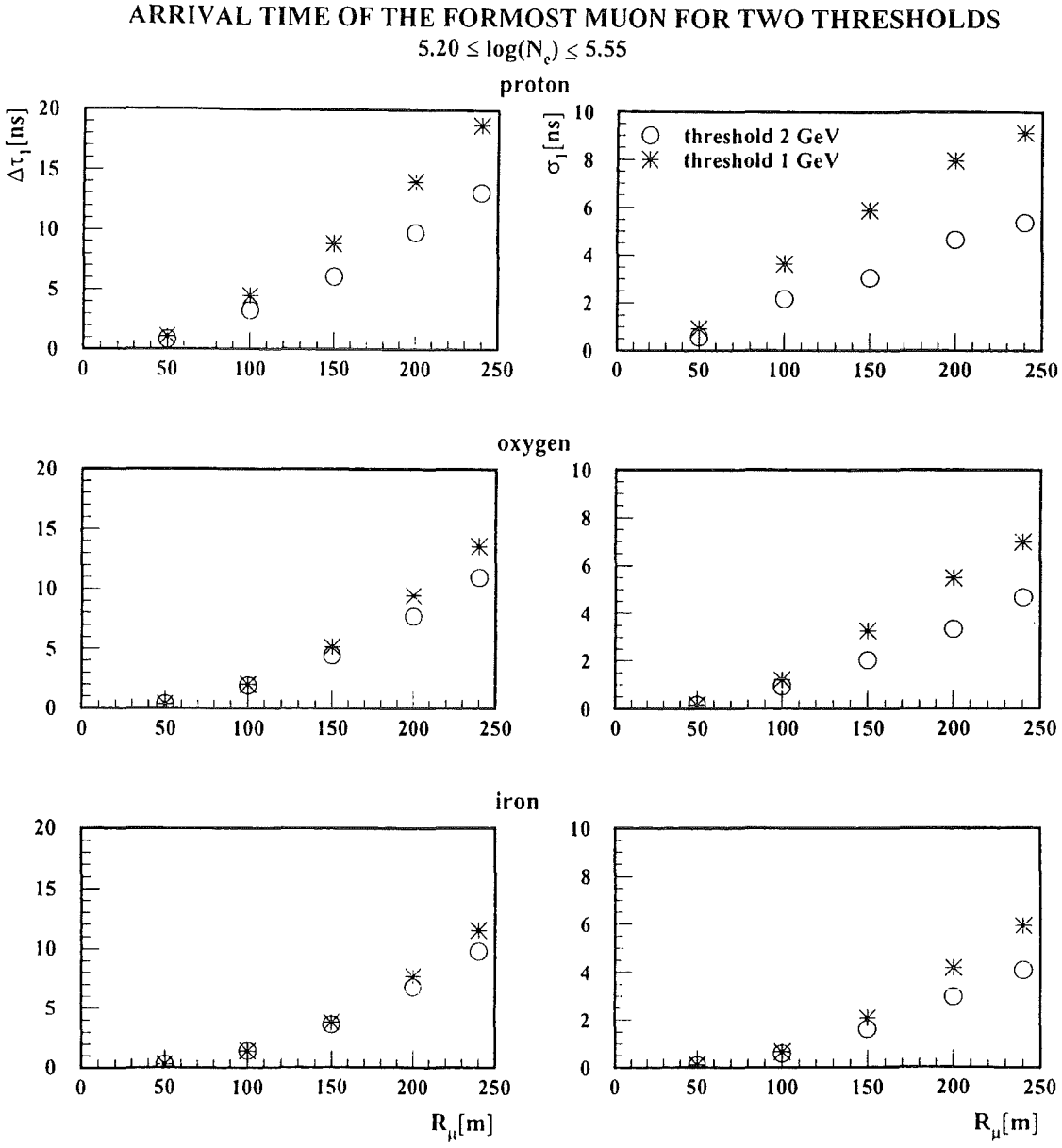
ARRIVAL TIME OF THE FORMOST MUON FOR TWO THRESHOLDS
5.20 ≤ log(N_e) ≤ 5.55
proton
oxygen
iron
Δτ_1[ns]
σ_1[ns]
threshold 2 GeV
threshold 1 GeV
R_μ[m]
R_μ[m]

Fig. A 8 a

ANGLE OF INCIDENCE OF THE FOREMOST MUON FOR TWO THRESHOLDS

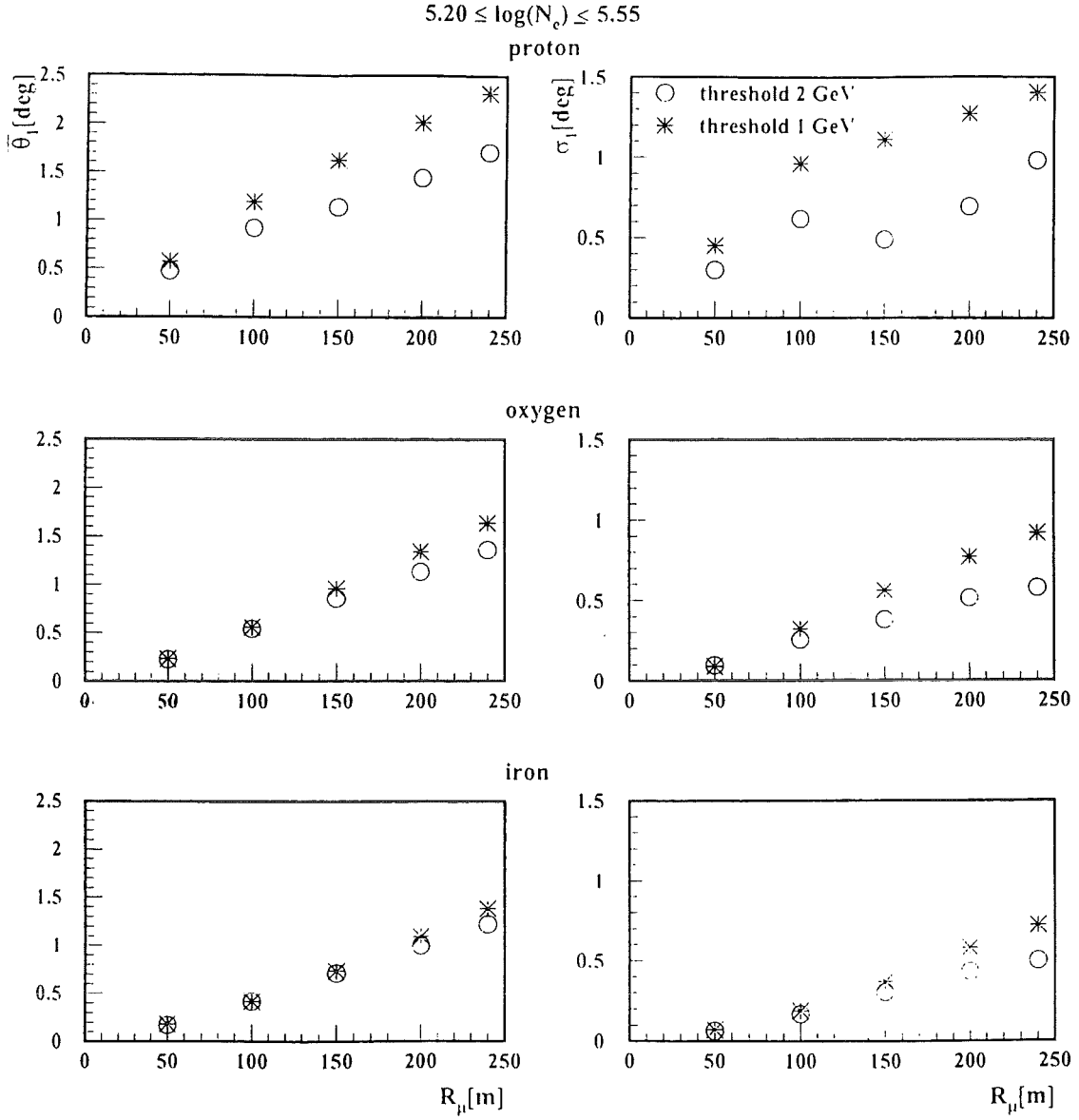

Fig. A 8 b

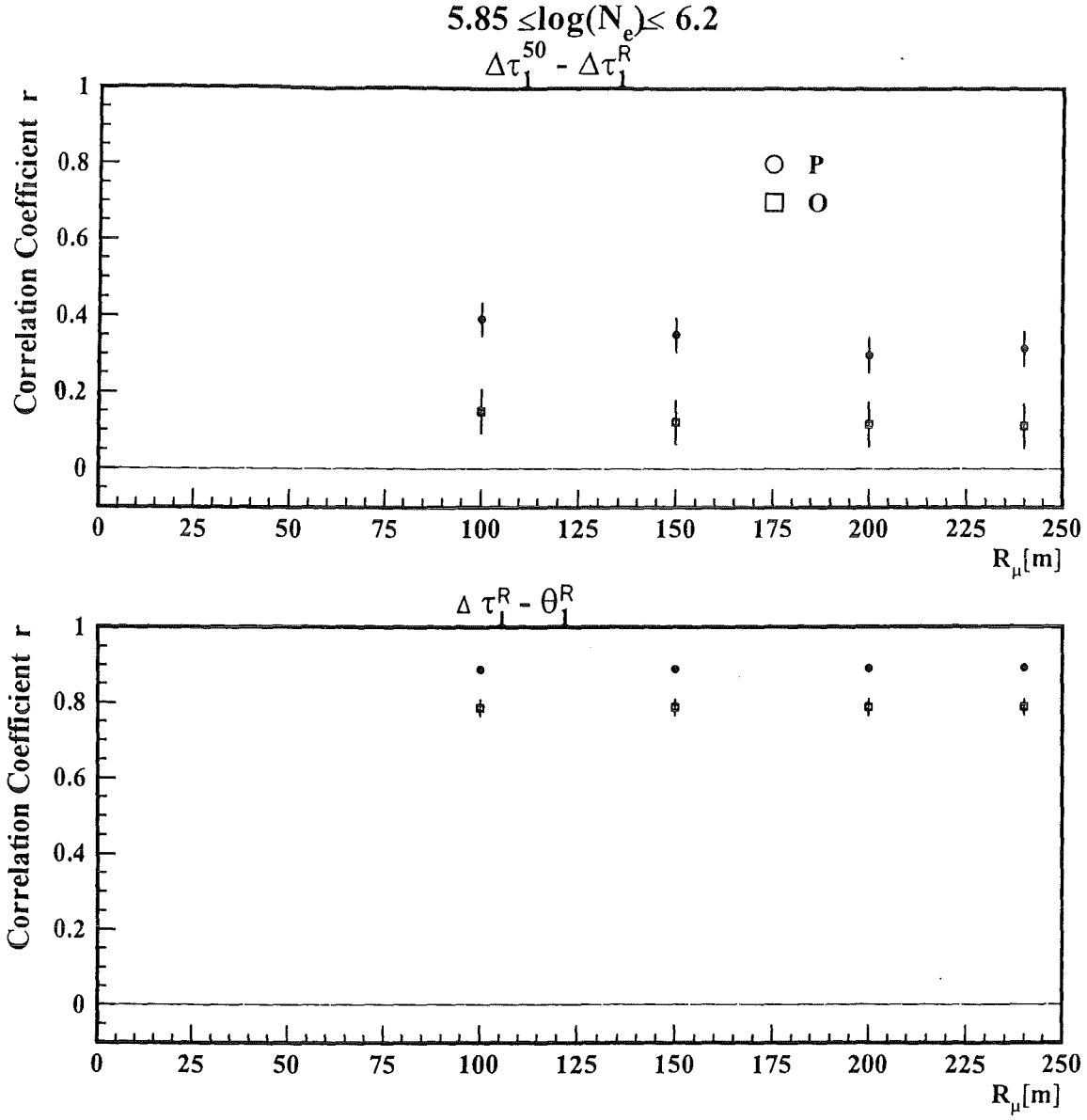
5.85 ≤log(N_e)≤ 6.2
Δτ_1^50 - Δτ_1^R
Correlation Coefficient r
P
O
R_μ[m]
Δ τ_1^R - θ_1^R
Correlation Coefficient r
R_μ[m]

Fig. A 9

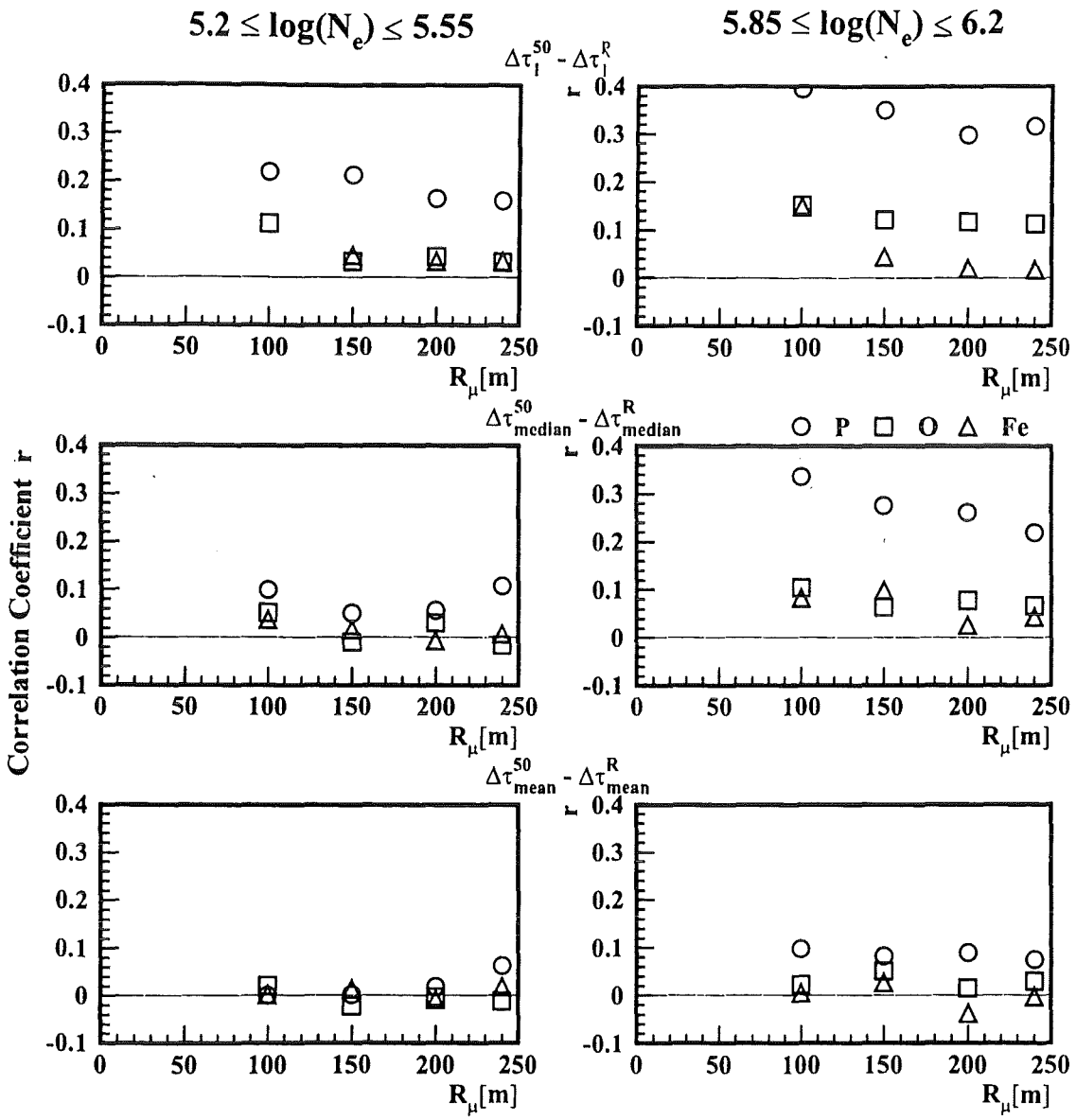
5.2 ≤ log(N_e) ≤ 5.55
5.85 ≤ log(N_e) ≤ 6.2
Δτ_I^50 - Δτ_I^R
Δτ_median^50 - Δτ_median^R
Δτ_mean^50 - Δτ_mean^R
Correlation Coefficient r
P O Fe
R_μ[m]

Fig. A 10 a

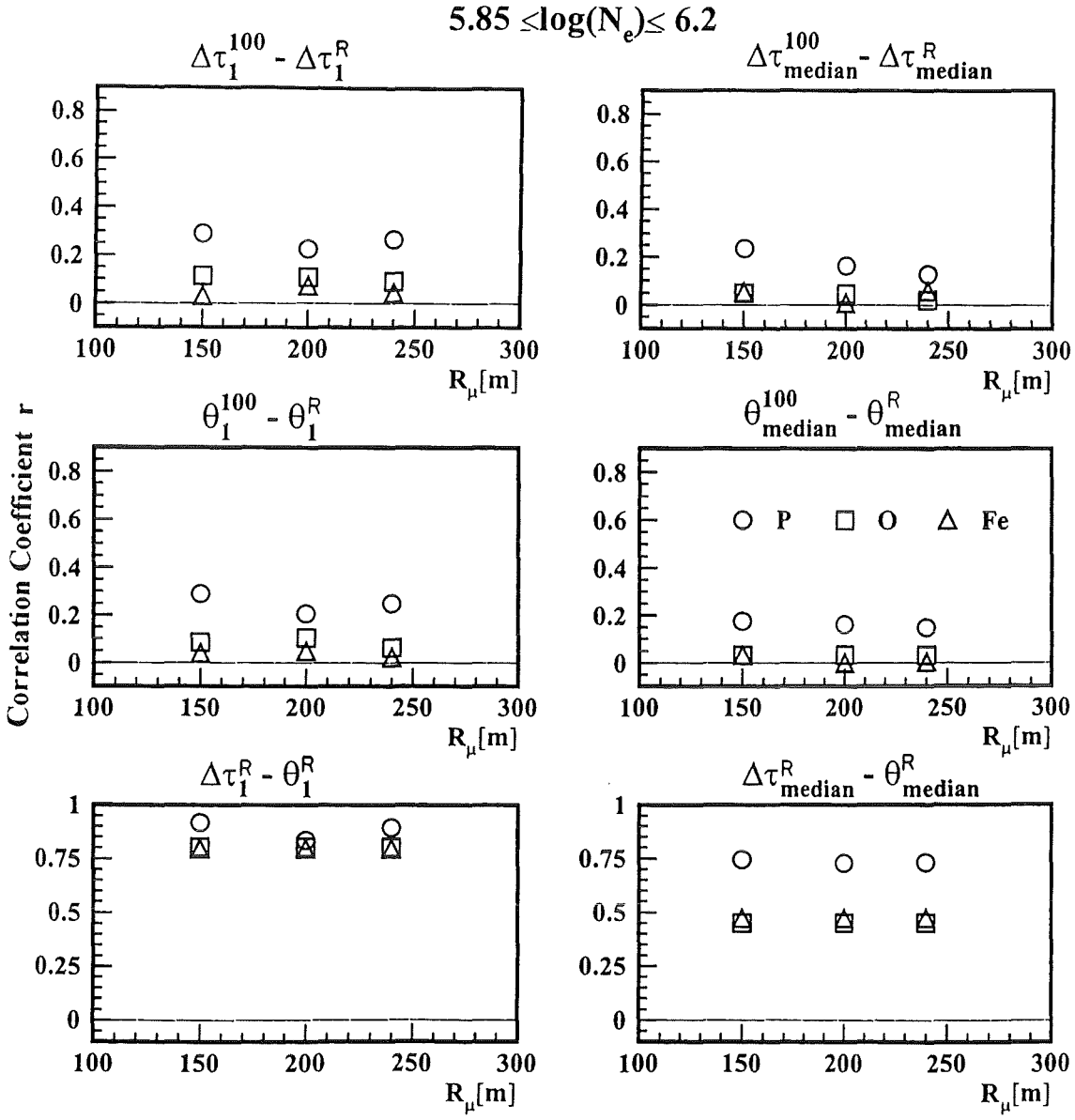
5.85 ≤log(N_e)≤ 6.2
Δτ_1^100 - Δτ_1^R
Δτ_median^100 - Δτ_median^R
θ_1^100 - θ_1^R
θ_median^100 - θ_median^R
Δτ_1^R - θ_1^R
Δτ_median^R - θ_median^R
Correlation Coefficient r
R_μ[m]
P
O
Fe

Fig. A 10 b

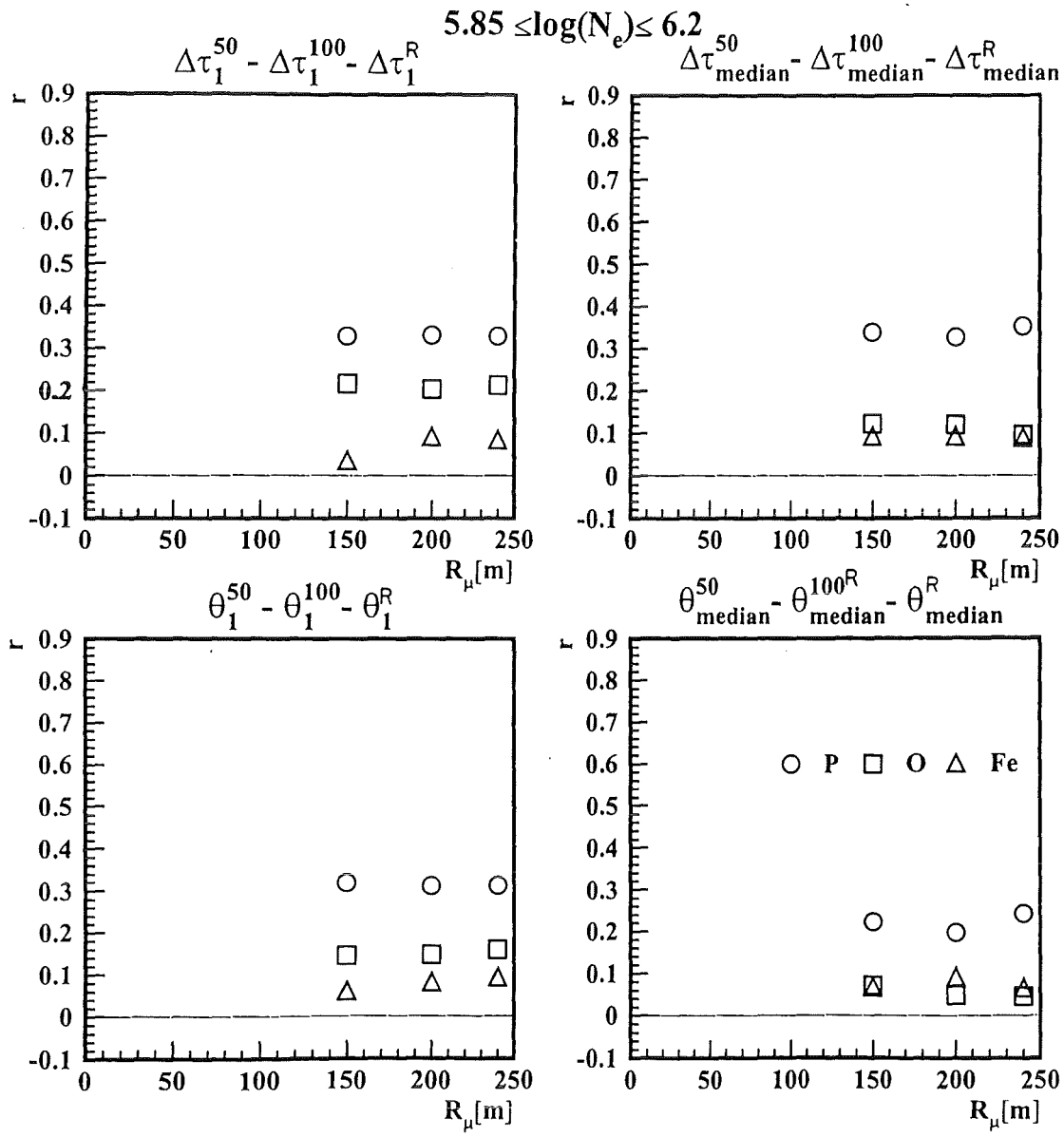
5.85 ≤log(N_e)≤ 6.2
Δτ_1^50 - Δτ_1^100 - Δτ_1^R
Δτ_median^50 - Δτ_median^100 - Δτ_median^R
θ_1^50 - θ_1^100 - θ_1^R
θ_median^50 - θ_median^100R - θ_median^R
r
R_μ[m]
P
O
Fe

Fig. A 10 c

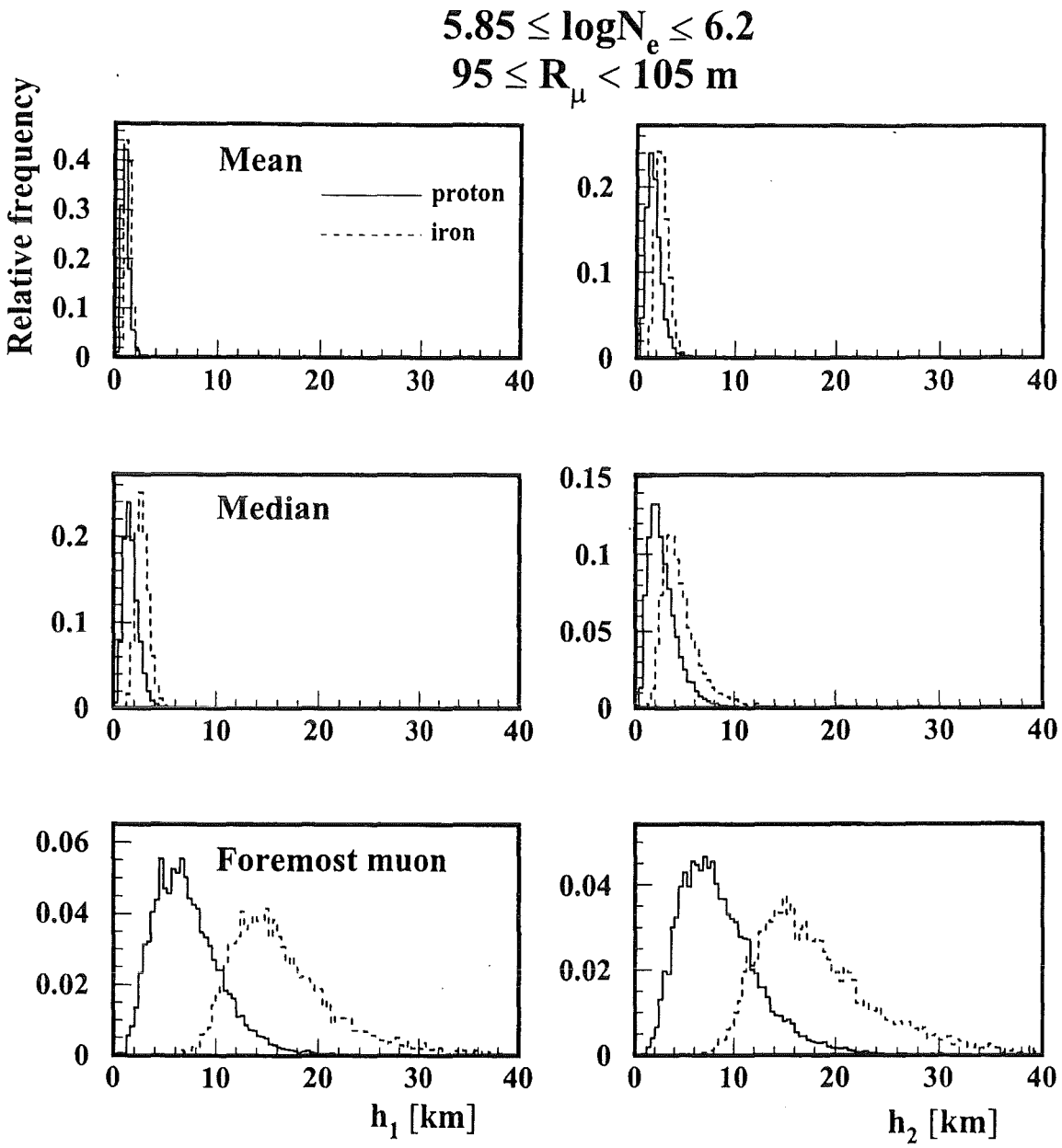
$5.85 \leq \log N_e \leq 6.2$
$95 \leq R_\mu < 105$ m
Relative frequency
Mean
proton
iron
Median
Foremost muon
h_1 [km]
h_2 [km]

Fig. A 11 a

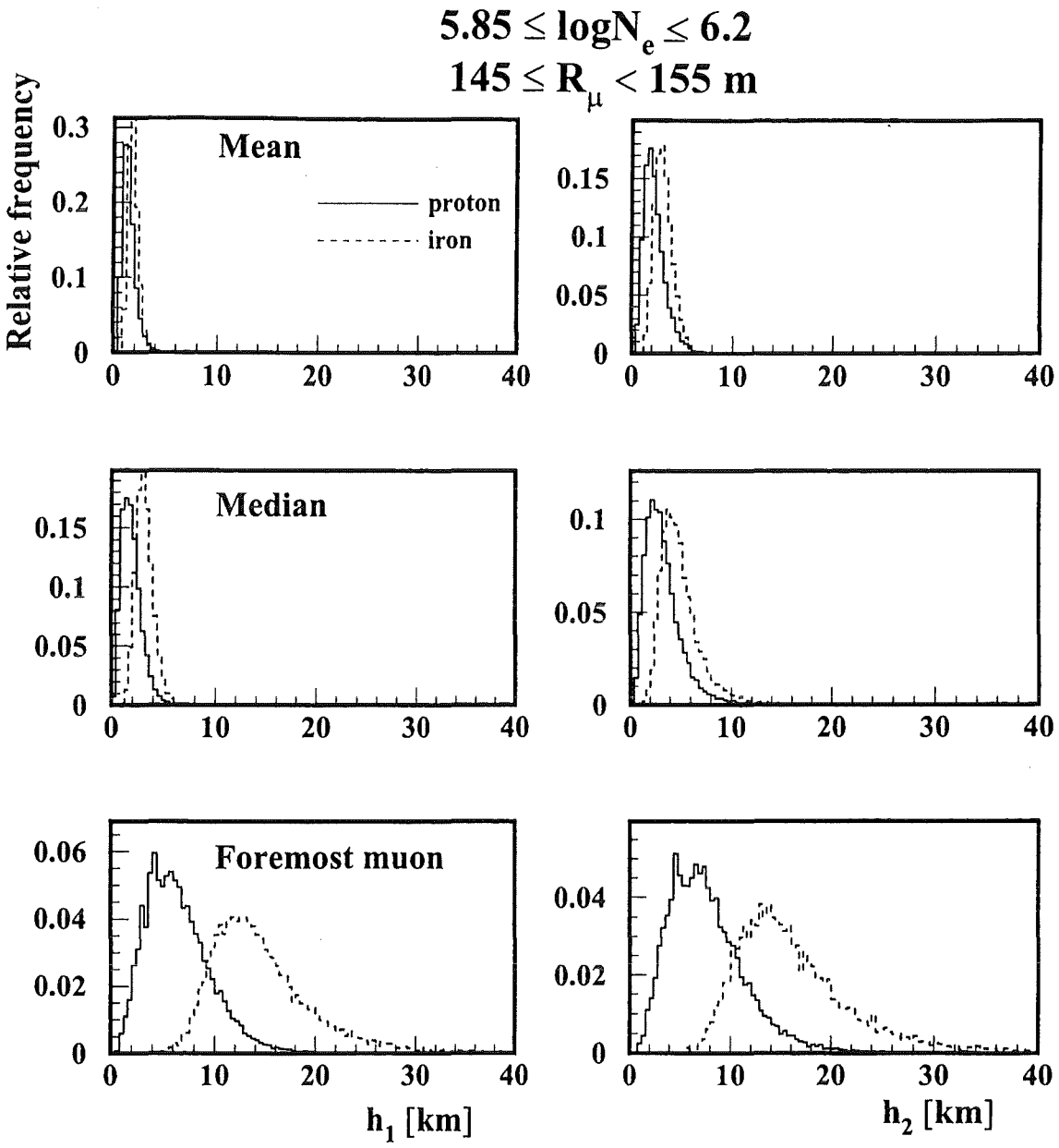
5.85 ≤ logN_e ≤ 6.2
145 ≤ R_μ < 155 m
Relative frequency
Mean
proton
iron
Median
Foremost muon
h_1 [km]
h_2 [km]

Fig. A 11 b

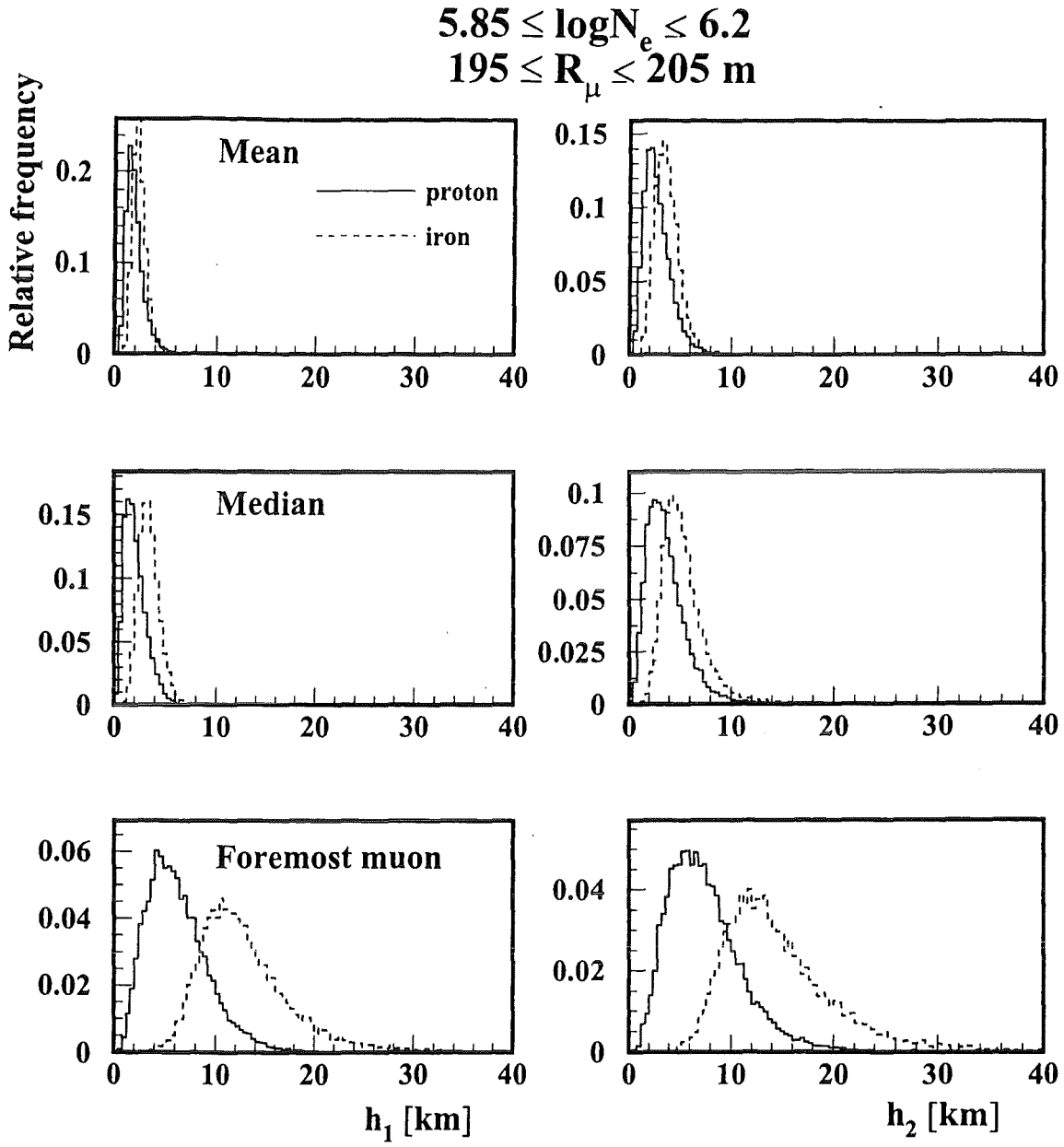
5.85 ≤ logN$_e$ ≤ 6.2
195 ≤ R$_\mu$ ≤ 205 m
Relative frequency
Mean
proton
iron
Median
Foremost muon
h$_1$ [km]
h$_2$ [km]

Fig. A 11 c